UNIVERSITY OF SOUTHAMPTON

Aerodynamics and Aeroacoustics of Flap Side-Edges

by

David Angland

Thesis for the degree of Doctor of Philosophy

in the
Faculty of Engineering, Science and Mathematics
School of Engineering Sciences

February 2008

UNIVERSITY OF SOUTHAMPTON

ABSTRACT

FACULTY OF ENGINEERING, SCIENCE AND MATHEMATICS
SCHOOL OF ENGINEERING SCIENCES

Doctor of Philosophy

Aerodynamics and Aeroacoustics of Flap Side-Edges

by David Angland

An experimental and computational investigation was carried out to determine the aerodynamics and aeroacoustics of a flap side-edge. A porous side-edge treatment was applied to the flap side-edge in an attempt to reduce airframe noise. Measurements taken as part of the experimental study were forces, on-surface pressures, particle image velocimetry, hotwire anemometry and on-surface microphones. Oil flow was performed to visualise the on-surface flow. A detached eddy simulation was performed on a geometry that consisted of a main element and a half span flap to understand the flowfield. From the experimental and computational investigation four sources of vorticity in the flowfield were identified, i.e. the main element cove, the main element trailing-edge, separation on the flap suction surface, and the flap side-edge vortical system. These sources of vorticity interacted to produce a significantly unsteady flowfield above the solid flap surface. Three potential acoustic sources on the flap were identified. The first two sources were the turbulent shear layers that rolled up to form the flap side-edge vortex, reattaching firstly on the side-edge and secondly on the suction surface of the flap. A mid-frequency broadband hump was measured by an on-surface microphone at the point of reattachment of the turbulent shear layer on the flap side-edge. The third source was a low frequency instability in the off-surface vortex due to non-linear vortical interactions upstream of the flap. This instability was measured by a hotwire in the downstream vortex and by an on-surface microphone in the main element flap cove. The application of a porous flap side-edge had two favourable effects. Firstly, it reduced the magnitude of vorticity in the turbulent shear layer and the vortex. This reduced the magnitude of the hydrodynamic instabilities induced by the flap side-edge vortex. Secondly, it displaced the vortex further away from the flap surface due to the finite mass flux allowed through the porous material. This reduced the magnitude of the disturbances that interacted with the solid flap surface by moving them further away. The effect of applying a porous flap side-edge was most noticeable in reducing the mid frequency broadband hump in the on-surface microphone measurements.

Contents

List of Figures

List of Tables

Acknowledgements

An áit a bhfuil do chroí
is ann a thabharfas do chosa thú.

My thanks to Prof. Xin Zhang for his supervision over the course of this PhD and for the times of encouragement and motivation when they were needed most. I am also indebted to him for the opportunity afforded to me to do my PhD here in Southampton.

A special thanks to all the wind tunnel and technical staff for their invaluable help throughout the course of this work.

I would like to thank all the friends I have met during my time in Southampton especially those I've shared an office with. A special mention is due to Scott, Koen, Kon, Raj, Sammie, Andy, Ed, Matthew, Martijn, Stevie and Enrico. You have all made my time here so enjoyable and we've had a lot of good times. The *craic* has been excellent! *Go raibh mile maith agaibh go léir. Ar scáth a chéile a mhaireas na daoine!*

I would especially like to thank all those with whom I have climbed with over the last few years. Thanks for sharing a rope and for all the great memories.

A special thanks to Ghaithaa for all her help, love and support.

Finally I would like to thank my parents and brother for all their unconditional love and support for me throughout my life. *Go bail ó Dhia oraibh.*

Nomenclature

a	Speed of sound, m/s
A_w	Cross sectional area of hotwire, m^2
b_F	Span of flap, m
C_2	Inertial resistance constant
C_D	Drag coefficient
C_{DES}	Constant in DES model
C_L	Lift coefficient
C_M	Pitching moment coefficient
C_p	Pressure coefficient
c	Reference chord, m
$\overline{c}$	Mean aerodynamic chord, m
c_F	Flap chord, m
c_p	Specific heat at constant pressure, J/g.K
d	Length scale in SA model, m
$\tilde{d}$	Modified length scale in DES model, m
E	Total energy, J/kg
$E(f)$	Power Spectral Density, dB/Hz
e	Internal specific energy, J/kg
f	Frequency, Hz
$H(f)$	Heavyside unit function
I	Acoustic Intensity, W/m^2
k	Turbulence kinetic energy, m^2/s^2
l_0	Correlation length of acoustic source, m
P_{ij}	Compressive stress tensor, N/m^2
Pr	Prandtl number
Pr_t	Turbulent Prandtl number
p	Pressure, N/m^2
Q	Convective heat transfer, W
q_i	Heat flux vector, W/m^2
R	Riemann invariant, m/s
Re	Reynolds number
r	Farfield distance, m

r_0	Vortex diameter, m
S	Planform area, m^2
S_{ij}	Strain rate tensor, 1/s
St_F	Strouhal number based on flap chord
T	Temperature, K
T_{ij}	Lighthill stress tensor, N/m^2
t	Time, s
t_F	Thickness of flap, m
u^+	Non-dimensional velocity
u_n	Velocity normal to boundary, m/s
u, v, w	Components of velocity in x, y and z directions respectively, m/s
V	Velocity magnitude, m/s
V_0	Non linear region in acoustic analogy
V_1	Linear region in acoustic analogy
x_F	Distance along flap chord, m
x, y, z	Cartesian coordinates, x positive downstream, y positive up, z positive to port
y^+	Non-dimensional wall distance

Greek Symbols

α	Main element angle of attack, degrees
$\Delta x, \Delta y, \Delta z$	Cell dimensions in x, y and z directions, m
δ_F	Flap deflection angle, degrees
$\delta(f)$	Dirac delta function
δ_{ij}	Kronecker delta function
Δt	Physical timestep size, s
δ^*	Boundary layer displacement thickness, m
ϵ	Turbulence dissipation rate, m^2/s^3
γ	Ratio of specific heats
μ	Molecular viscosity, Ns/m^2
μ_t	Turbulent viscosity, Ns/m^2
ν	Kinematic viscosity, m^2/s
ν_t	Eddy viscosity, m^2/s
$\tilde{\nu}$	Modified eddy viscosity in SA model, m^2/s
θ	Angle, rad
τ_{ij}	Shear stress tensor, N/m^2
ρ	Density, kg/m^3
Ω	Non-dimensional vorticity based on flap chord

ω	Vorticity, 1/s
ω^*	Dimensionless angular frequency

Subscripts

i	Conditions in interior domain
w	Conditions at wall
∞	Conditions at freestream

Superscripts

$\prime$	Perturbation

Acronyms

AIAA	American Institute of Aeronautics and Astronautics
CAA	Computational Aeroacoustics
CFD	Computational Fluid Dynamics
CFL	Courant Number
CMT	Continuous Moldline Technology
CTA	Constant Temperature Anemometry
DES	Detached Eddy Simulation
DNS	Direct Numerical Simulation
FWH	Ffowcs-Williams Hawkings
LADA	Large Aperture Directional Array
LES	Large Eddy Simulation
MICS	Microphones
PIV	Particle Image Velocimetry
PMA	Phased Microphone Array
PPI	Pores Per Inch
PSD	Power Spectral Density
RANS	Reynolds-Averaged Navier-Stokes
SA	Spalart Allmaras
SADA	Small Aperture Directional Array
SPL	Sound Pressure Level
SST	Shear Stress Transport
URANS	Unsteady Reynolds-Averaged Navier-Stokes
ZOC	Zero, Operate and Calibrate

Chapter 1

Introduction

1.1 Introduction to Topic

With civil aviation noise regulations becoming more stringent, noise reduction is becoming an increasingly important consideration for civil aircraft manufacturers. The noise generated by an aircraft comes mainly from two sources, i.e. engine and airframe. The airframe noise is generated as a result of the airframe moving through the air. The main contributors to the airframe noise are landing gear and high-lift devices. Noise of modern aircraft in their approach configuration can be dominated by the airframe noise since the engines are normally operated at a reduced power setting [1]. Therefore, the airframe noise has become an important consideration for noise certification and its environmental impact.

In an effort to reduce airframe noise, researchers have focused on landing gear and high-lift devices, since these are the main airframe noise generating components of an aircraft. A strong vortex that exists at the outboard flap side-edge has been identified as a strong source of airframe noise [2]. In the vicinity of the flap side-edge, there is an unsteady, turbulent flowfield that produces hydrodynamic perturbations. The sharp edges at the flap side-edge lead to acoustic scattering of these hydrodynamic perturbations. Therefore, unsteadiness in the flap side-edge region is efficiently converted to noise and is radiated to the farfield. By modifying the flowfield around the flap side-edge, the magnitude of these disturbances can be reduced or displaced further away from the solid surface. By changing the geometry of the sharp edges, the efficiency of the scattering of these sources can also be reduced.

1.2 Aims of Thesis

This research was focused on understanding noise generation mechanisms associated with the flowfield around a flap-side edge and their reduction. Previous investigations identified a noise reduction of up to 4 dB in the farfield, within a limited band of frequencies, by replacing part of a flap side-edge with an open cell porous material [3]. The physics responsible for this were not discussed. The present work employed a variety of experimental and numerical techniques to understand the physics responsible for noise production at the flap side-edge and the mechanism by which a porous material applied to the flap side-edge reduced the noise.

As part of the experimental investigation, measurements taken included forces, on-surface pressures, particle image velocimetry, hotwire anemometry and on-surface microphones. Oil flow was also used for on-surface flow visualisation. Experiments were performed on a hardwall case and three different porous flap side-edge treatments. As part of the numerical study, a detached-eddy simulation was performed with a hardwall and a porous side-edge. The nearfield unsteadiness determined in the simulation was used as an input to a Ffowcs-Williams Hawkings solver to obtain the farfield acoustics.

1.3 Structure of Thesis

This thesis is divided into four main sections. Firstly, a review of the relevant literature and a discussion of the previous work performed in this field is presented in Chapter 2. This includes noise generation mechanisms at the flap side-edge proposed by various authors as well as possible noise reduction strategies.

Secondly, the experimental results are detailed and discussed in Chapters 3 to 6. Chapter 3 describes the experimental techniques used as well as the design of the wind tunnel model. Chapter 4 presents the experimental results for the hardwall case. Chapter 5 contains the results for the experiments performed with three different porous side-edges. Chapter 6 presents the results for a split flap configuration and the effect of applying a porous side-edge to this configuration.

In the third section, the numerical results are presented and discussed in Chapters 7 to 8. Chapter 7 describes the computational methodology including grid generation issues and boundary conditions. Chapter 8 presents the results of a detached eddy simulation of the flowfield around a flap side-edge.

Finally, both the experimental and computational conclusions are presented in Chapter 9.

Chapter 2

Literature Review

2.1 Introduction

A survey of the literature pertaining to flap side-edge aerodynamics and aeroacoustics and related topics was conducted. The findings of this survey are presented herein. The relevant literature is discussed under a number of headings. Section 2.2 discusses those studies that involved airframe noise studies and in particular those that identified the flap side-edge as a major noise source, to put into context this current work. Section 2.3 gives a review of studies concerning computational aeroacoustics and in particular the use of acoustic analogies to obtain farfield acoustics from a detailed simulation of the nearfield fluid. Section 2.4 discusses references that deal with the aerodynamics of a flap side-edge and the flow phenomena present. Section 2.5 contains references concerned with aeroacoustic studies of the flap side-edge including noise generation mechanisms and measured spectra and directivities. Section 2.6 details the noise generation mechanisms at the flap side-edge that has been proposed in the literature to date. Section 2.7 presents studies that proposed noise reduction methods for the flap side-edge by active and passive means.

2.2 Flap Component Airframe Noise Studies

In the 1970's numerous experimental studies were performed that showed there was strong airframe noise associated with the side-edge of deployed trailing-edge wing flaps [4, 5, 6]. The pressure differential between the upper and lower surfaces produced an oscillating vortical system, which resulted in a strong tonal noise [7]. In general, any vortical pattern in a flow generates sound as soon as its inertia is modified because the corresponding change in the pressure gradients also induces density fluctuations that propagate as sound. At moderately subsonic Mach numbers this essentially occurs as

convected vortical patterns interact with solid surfaces [8]. According to interference patterns observed in flyover noise measurements of an aircraft with high lift devices deployed, flap noise dominates in the forward arc at high frequencies [9].

Fink [10] detailed a method used to calculate airframe noise. The method calculated the noise radiated from each individual portion of the aircraft independent of other noise sources. Each noise component was described by an appropriate aeroacoustic mechanism, velocity dependence, directivity and spectrum. The trailing-edge flap spectra was taken from studies on a Vickers VC-10 aircraft [11] at three different flap deflection angles. The three different measured spectra for the three flap deflection angles, had all approximately the same shape. Fink assumed that the trailing-edge flap Sound Pressure Level (SPL) varied with the square of the sine of the flap deflection angle. This caused all three spectra at different flap deflection angles to collapse. The SPL was also assumed to vary directly with flap area, inversely with far-field distance squared and directly with airspeed to the sixth power. Frequency was scaled as a Strouhal number relative to flap chord. According to Fink, the directivity of the trailing-edge flap noise appeared to be that of a lift dipole normal to the flight direction.

Chow *et al.* [3] provided a summary of the work done on a European reduction of airframe noise project. The work included baseline noise source studies and methods to reduce the strength of these noise sources. It also included an experimental database and noise prediction modelling. Full scale flight tests were performed with an Airbus A340 aircraft. The results demonstrated that landing gear noise dominated over the high-lift devices noise and also that noise from slats dominated over noise from flaps. The noise generated by the flaps varied with velocity to the eighth power while for combined high-lift devices the velocity law was $V_{\infty}^{5.5}$. This differs from the value suggested by Fink [10].

An analysis of a series of aeroacoustic experiments performed on an $1/11^{\text{th}}$ scale Airbus A320 model in an open anechoic wind tunnel was presented by Davy and Moens [12]. The study was aimed at characterising the airframe noise sources. The main noise sources were localised using a two-dimensional cross-shaped array of microphones. Correlations were performed on both the nearfield and farfield microphone data to determine the spectral content of the sources. They determined that flap sources were a lower contributor to the overall airframe noise of the model than slat sources. The experimental study identified the main flap noise source located at the flap side-edge. At low frequencies, slat noise dominated over flap side-edge noise. In the middle frequency range the flap side-edge was dominant. The authors concluded that at high frequency and particularly upstream, the outboard flap side-edge noise was a significant contributor to the overall airframe noise.

These references were of interest for background to flap side-edge aeroacoustics and indicated there was an important noise source located at the flap side-edge.

2.3 Computational Aeroacoustics

2.3.1 Issues and Methods

Computational Aeroacoustics (CAA) is concerned with accurate numerical prediction of aerodynamically generated noise as well as its propagation. Aeroacoustic problems like aerodynamic problems are governed by the Navier-Stokes equations. However, aeroacoustic problems are distinctly different in their nature, characteristics and objectives. Tam [13] presents some of the computational issues that are unique to aeroacoustics which demonstrates their difference to commonly encountered Computational Fluid Dynamics (CFD) problems. Aeroacoustic problems are time dependent. In most aircraft noise problems the frequencies are high, which means the wavelengths are small. Tam suggests that typically a minimum of six to eight mesh point per wavelength is required for direct numerical simulation. Due to the large spectral bandwidth of aeroacoustic problems, an enormous amount of mesh points are needed in the computational domain. The root-mean-square velocity fluctuation associated with the radiated sound are many orders of magnitude less than the mean flow and usually smaller than the error. Because of this, Roe [14] fears that the acoustic solutions may be hopelessly corrupted by computational noise. This issue is related to the disparity between the magnitudes of acoustic waves and the mean flow.

Due to the problem of distinct and well-separated length scales, the spatial resolution for a Direct Numerical Simulation (DNS) simulation is important. The computational time step is dictated by the size of the finest mesh to keep the Courant number (CFL) less than its critical value for a stable finite difference scheme. For very small spatial resolution this leads to excessive CPU time. For aerodynamic problems the primary interest is in determining the loads and moments acting on the body being modelled. Therefore, the solution only needs to be accurate around the body of interest. In aeroacoustic problems the directivity and spectrum of the radiated sound in the farfield are the quantities of interest. Since the distance from the noise source to the boundary is relatively large it is imperative that the numerical scheme must be free of numerical dispersion, dissipation and anisotropy. According to Tam, very few time-marching schemes can meet this demanding requirement.

Radiation and outflow boundary conditions are needed to allow the acoustic and flow disturbances to leave the computational domain with minimal reflection. Radiation boundary conditions are needed along boundaries with inflow to allow the acoustic

waves to propagate out of the computational domain. The Euler equations support three types of small-amplitude disturbances, i.e. acoustic, vorticity and entropy waves. Along boundaries of outflow, a set of outflow boundary conditions are required to facilitate the exit of acoustic, vorticity and entropy disturbances [13]. Wall boundary conditions are also important for aeroacoustic computations. Since the spatial derivatives are normally high-order, the order of the resulting finite difference equations are higher than the original partial differential equations. Therefore the number of boundary conditions needed for a unique solution are greater. As well as extraneous boundary conditions the use of high-order equations implies the generation of spurious numerical solutions near wall boundaries [13].

2.3.2 Acoustic Analogies

Instead of incurring the significant computational cost of resolving the acoustic waves as they propagate to the farfield, an acoustic analogy approach can be invoked. The acoustic analogy extracts the necessary information out of an unsteady CFD calculation and then performs an integration and computes time dependent density or pressure fluctuations in the farfield, as well as the related frequency spectra. The basis of the acoustic analogy is to identify an outer region (V_0) where the acoustic waves are assumed to propagate linearly. The acoustic region surrounds a non-acoustic region (V_1) where the governing linear equation does not apply and the flowfield has to be either simulated by numerical methods or measured in detail experimentally. Morfey [15] describes two distinct approaches for matching the acoustic field (V_0) to the "non-acoustic" region (V_1). The first is where the non-linear region (V_1) is replaced by an extension of the linear region (V_0), with equivalent sources added to represent the flow. The second is where the numerical solution in the nonlinear region (V_1) is matched directly to a linear acoustic solution in (V_0) by applying appropriate matching conditions across the interface.

The Lighthill acoustic analogy [16] allows the noise generation and propagation to be divided into the computation of fluctuations in the near-field and a separate computation of the generation and propagation of noise. The compressible Navier-Stokes equations can be written to describe the propagation of sound in a uniform medium at rest due to externally applied fluctuating stress as,

$$\frac{\partial^2 \rho'}{\partial t^2} - a_\infty^2 \frac{\partial^2 \rho'}{\partial x_i^2} = \frac{\partial^2 T_{ij}}{\partial x_i \partial x_j} \ . \tag{2.1}$$

The left-hand side is the linear wave equation and the right-hand side is a source term to the medium outside the region of the fluctuating flow. This term results from the nonlinear convection and viscous terms in the momentum equation. This source term is assumed known from the solution of the nearfield fluctuating flow. The Lighthill stress

tensor T_{ij}, known as the quadrupole term, is given as follows,

$$T_{ij} = \rho\, u_i u_j + P_{\,ij} - a_{\,0}^{\,2}\, \rho'\, \delta_{ij}\ . \tag{2.2}$$

The compressive stress tensor $P_{\,ij}$ written in terms of velocity gradients is as follows,

$$P_{\,ij} = p'\, \delta_{ij} + \mu \Bigg\{ - \frac{\partial u_i}{\partial x_j} - \frac{\partial u_j}{\partial x_i} + \frac{2}{3} \left(\frac{\partial u_k}{\partial x_k} \right) \delta_{ij} \Bigg\}\ . \tag{2.3}$$

When the flow is assumed to be effectively incompressible ($M^2 \ll 1$) [17] and viscous dissipation is neglected at high Reynolds numbers, then the Lighthill stress tensor is approximated as $T_{ij} \approx \rho\, u_i u_j$. Curle [18] showed that sound, in the presence of stationary boundaries, was generated not only by the distribution of acoustic quadrupoles given by the right hand side of Equation 2.1 but supplemented by a surface distribution of acoustic dipoles. In the presence of stationary boundaries an additional surface term appears,

$$\frac{\partial^2 \rho'}{\partial t^2} - a_{\,\infty}^{\,2}\, \frac{\partial^2 \rho'}{\partial x_i^2} = \frac{\partial^2 T_{ij}}{\partial x_i \partial x_j}\ - \frac{\partial}{\partial x_i} \left[\left(P_{ij} + \rho\, u_i u_j \right) \delta(f)\, \frac{\partial f}{\partial x_j} \right]\ . \tag{2.4}$$

The unsteady flow in the vicinity of an edge is an important source of aerodynamic sound [19]. Ffowcs-Williams and Hawkings (FWH) allowed a moving permeable surface boundaries within (V_1) to be replaced by equivalent sources. The FWH equation [20] is an extension of Lighthill-Curle theory of aerodynamic sound to include arbitrary convective motion. This, like the previous acoustic analogy, is an integral technique that can predict the farfield signal based solely on nearfield input. The time histories of all the flow variables are needed but no spatial derivatives are explicitly required [21]. The solution of the FWH equation requires a surface and a volume integral. Ffowcs-Williams and Hawkings volume displacement term for moving surfaces, which is a monopole distribution on the surface, appears as an additional term. The differential form of the FWH equation is as follows,

$$\begin{aligned} \left(\frac{\partial^2}{\partial t^2} - a_{\,0}^{\,2}\, \frac{\partial^2}{\partial x_i^2} \right) \left(H(f) \rho' \right) &= \frac{\partial^2}{\partial x_i \partial x_j} \left(T_{ij} H(f) \right) \\ - \frac{\partial}{\partial x_i} \left(\left(P_{ij} + \rho\, u_i u_j \right) \delta(f)\, \frac{\partial f}{\partial x_j} \right) &+ \frac{\partial}{\partial t} \left(\rho_0\, u_i\, \delta(f)\, \frac{\partial f}{\partial x_i} \right)\ . \end{aligned} \tag{2.5}$$

The Heavyside unit function is defined as unity when $f > 0$ and zero when $f < 0$, where the function $f = 0$ defines the surface outside which the solution is required. Equation 2.5 is usually solved using a Green function technique. The solution is often well approximated by the surface integral alone and the volume term can be ignored [22]. Acoustic analogies calculate the density or pressure fluctuations in the farfield and related frequency spectrum. Acoustic analogies are computationally less expensive than resolving the acoustic waves all the way out to the farfield and therefore are desirable from that respect.

2.4 Flap Side-Edge Aerodynamics

This section outlines various aerodynamic investigations into flap side-edges. Firstly, the experimental studies are reviewed and relevant results discussed. Secondly, the results of computational fluid dynamics studies are discussed. Thirdly, computational issues pertinent to the current investigation are reviewed and discussed.

2.4.1 Experimental Studies

Spaid and Lynch [23] performed experiments to illustrate some of the crucial flow physics associated with high-lift geometries at full scale Reynolds numbers. Data included static pressure distributions, lift and drag measurements, and boundary layer and wake surveys. Spaid and Lynch suggested that the data could be useful for CFD code calibration since CFD struggles to accurately model complex flowfields associated with high-lift configurations such as confluent boundary layers and merging wakes from multi-elements [23]. An important observation was that Reynolds number variations had a large impact on the performance of high-lift configurations. Valarezo *et al.* [24] and Lynch [25] noted that important performance parameters did not scale simply with Reynolds numbers. This made accurate extrapolation of data from low Reynolds numbers experiments to full scale difficult. Spaid and Lynch [23] concluded that it was important to make measurements at Reynolds numbers representative of flight conditions.

The wakes of upstream elements were found to decrease the loading on the trailing-edge flap. The spreading/merging of wakes due to changes in flap gap and deflection angle were crucial to the maximum lift characteristics. Flap gaps and overhangs that promoted merging of the flap boundary layer and main element wake were associated with less than optimum maximum lift but did suppress flap separation. Increasing the flap deflection did not counteract this unfavourable effect. As the flap deflection angle increased, the slat and main element were subjected to a higher adverse pressure gradient. This increased the wake spreading and limited any improvements in maximum lift capability.

The applicability of this experimental study to the present work was limited. This was due to a lack of discussion of the flow features at the flap side-edge. By knowing the flow features, the potential acoustic sources could be hypothesised. Of more value, in terms of insight, were the computational investigations, which are discussed in the next section.

Gursul presented a review of unsteady vortex flows [26]. Kelvin-Helmholtz type instabilities were identified in the shear layers that rolled up to form the vortices. Vortex wandering was defined as large, broadband fluctuations that were due to random dis-

placements of the vortex core. One of the proposed causes for vortex wandering was freestream turbulence [27]. However, Menke and Gursul [28] showed that the vortex core displacements were greater than those caused by freestream turbulence. Gursul [29] determined that a definite correlation existed between the vortex wandering and the presence of Kelvin-Helmholtz instabilities in the separated shear layer that formed the vortex. Non-linear interactions between the small vortices in the shear layer and the primary vortex led to the random displacements of the primary vortex core.

2.4.2 Computational Studies

According to Meredith [30] some of the flowfield physics associated with high-lift flows that pose challenges to CFD are laminar flow regions, attachment line transition, relaminarisation, transonic slat flow, confluent boundary layers, wake interactions, separation, and reattachment. Lynch *et al.* [31] stated that even for two-dimensional flows, state-of-the-art CFD codes were unable to consistently predict increments in performance as a result of changes in Reynolds number and slat/flap positions. Numerous computational solutions have been performed on the flow over a three-dimensional high lift wing with the aim of understanding the prominent flow structures associated with both the inboard and outboard flap side-edges. According to Khorrami *et al.* [32] these efforts were motivated by a lack of understanding of noise producing fluid dynamical processes at the flap side edge.

Khorrami *et al.* [32] performed an extensive computational investigation of a generic high-lift configuration comprising of a wing and a half-span flap at flap deflection angles of 29 and 39 degrees. The steady computational solutions were obtained using the thin-layer form of the Reynolds Averaged Navier-Stokes (RANS) equations and the Spalart-Allmaras turbulence model [33]. The reason cited for using this turbulence model was its robustness, efficiency and ability to handle flows where separation and reattachment occur. The computational results for on-surface pressure measurements were compared with experimental results obtained using the 7×10 Quiet Flow Facility at NASA Langley. The steady computational results showed the presence of a dual vortex system; a strong vortex that formed on the lower portion of the flap side edge and a weaker one that formed near the edge on the flap top surface. The primary vortex rapidly grew in size in the streamwise direction and eventually occupied the entire flap side-edge. However, the weaker vortex only grew moderately. Somewhere near the flap mid-chord Khorrami *et al.* noted that the primary vortex, which was detached from the side-edge, moved to the upper surface and merged with the top vortex to form a single strong vortex. Khorrami *et al.* postulated that the separated shear layer at the bottom flap side edge was a constant source of vorticity that was wrapped around the vortex and "fed it". These shear layers were formed due to boundary-layer separation at both bottom and top sharp corners on the flap side edge. This constant feeding of vorticity

resulted in a stronger vortex with a low-pressure core, which caused the axial velocity in the core to obtain a speed up to twice the freestream speed.

Another important flow feature noted by Khorrami *et al.* [32] was the presence of vortex breakdown for the 39 degrees flap deflection case. This reference was the first time that vortex breakdown had been reported to be numerically computed in a multi-element high-lift configuration. This was observed in the post-merged vortex near the flap trailing edge where the adverse pressure gradient caused a rapid deceleration of the vortex core axial velocity and eventually caused the vortex to breakdown with a region of axial flow reversal. Beyond the breakdown region, the core axial velocity accelerated again and was directed downstream. Khorrami *et al.* did not postulate any reason why this was so. The authors noted that the vortex breakdown in this case was quite dissimilar to the classical bubble-type or spiral-type breakdowns that were observed in an axisymmetric tube in the region of the breakdown point[1]. Rather than the internal recirculating zones, an apparent focal point (or in three-dimensions a saddle point) existed through which all the streamlines converged. This paper was useful in detailing the flow phenomena present around the flap side edge, namely shear layer roll-up, multiple vortex formation, vortex merging and vortex breakdown processes.

A steady RANS computation was carried out on a high-lift configuration with taper and sweep by Khorrami *et al.* [34]. While the earlier study [32] was concerned with a two-element high-lift wing to capture the complex nature of a flap side-edge flow field, this study examined the effects of sweep and taper on a flap side-edge flow field at flap deflection angles of 20 and 30 degrees. The computations were performed using the Spalart-Allmaras one-equation turbulence model [33] with a solid-body rotation modification. The reason proposed for this was that streamwise vortices that displayed solid-body rotation usually exhibited weak turbulent fluctuations and behaved in a "laminar-like" manner. Khorrami *et al.* suggested that this was due to the strong centrifugal force field. The solid-body rotation modification dampened the turbulent viscosity in regions that demonstrated solid-body-rotation and produced better results for vortex dominated flows. This has important implications for the choice of an appropriate turbulence model for the present study.

Khorrami *et al.* [34] noted that according to the acoustic array measurements, the outboard flap side-edge was found to be a more potent noise source than the inboard flap side-edge. The reason postulated was the outboard vortex path remained closer to the side-edge than the inboard path and vortex breakdown first occurred at the outboard edge and at lower flap deflection angles. A conclusion of this study was that vortex breakdown was not unique to those simple generic configurations and in reality occurred at any flap side-edge in a high-lift setting.

[1] See §2.5.3 for a brief discussion of vortex breakdown

Similar to the previous studies discussed, Streett [35] also noted two separation bubbles, with associated streamwise vorticity and roll-up at the upper and lower corners of the flap edge. The reattachment point of the side-edge vortex moved up the side-edge as the flow progressed along the flap chord until it reached the upper corner. The side-edge vortex then travelled over the upper corner interacting and then merging with the upper-surface vortex. This single vortex was fed with vorticity from the cylindrical shear layer that emanated from the lower edge. The mechanism of continually feeding vorticity into the vortex produced a strong jet-like flow in the core of the vortex.

More recently, Cummings *et al.* [36] performed a detached-eddy simulation on a high-lift wing on an unstructured grid. The geometry consisted of a half-span flap and a three-quarter span slat. Grid refinement was applied to the slat, main element leading edge, main element flap cove and flap regions. The largest grid size was 5.2×10^6. Although some unsteadiness was found in the slat region, the flap-tip vortex was found to be steady. The authors recognised a need for improvement in the grid density.

Sensitivities of the computed solutions are categorised by Moitra [37] as those dependent on the grid and those depending on the flow solver. Grid attributes such as surface point distribution, normal spacing near the surface, grid stretching ratio and grid density in the wake regions have large effects on the accuracy of the computed solution for complex high-flows. Moitra stated that turbulence models and transition location were the principal sources of flow solver sensitivities. Subtle differences in turbulence modelling caused differences in the prediction of wake growth, particularly for wakes in adverse pressure gradients which characterise high-lift flowfields. Since the location and extent of separation was strongly influenced by the transition location, it was important to accurately predict the location of the transition from laminar to turbulent flow.

2.4.3 Grid Generation Issues

Moitra [37] presented grid attributes for computing high-lift flowfields. These were obtained by systematically varying grid parameters until an increase in grid density no longer produced appreciable variations in surface pressure and skin-friction coefficients as well as integrated quantities such as lift, drag and pitching moment. Moitra [37] stated that the difficulty in creating such grids was ensuring sufficient grid density in the areas of interesting flow phenomena, while preventing deterioration of grid density and smoothness in other areas. This was further compounded by the disparity in length scales that were associated with the complex physics in a high-lift configuration and even more so in acoustic problems. The three principal areas of interest to Moitra were the resolution of the boundary layer, grid density on the surface of the geometry, and resolution of wakes including regions of merging or separation. Distribution of points

on the surface was controlled by clustering grid points in regions of high curvature and limiting the maximum allowable spacing between two adjacent grid points in regions of low curvature. A grid converged solution was obtained. No change in the computed solution was obtained when the maximum allowable spacing between two adjacent grid points was decreased below a value of 0.3 percent chord, thus establishing an optimal surface grid parameter value. According to Moitra in a previous study conducted by Boeing, the maximum limits on surface spacing were established to be 0.1 and 0.3 percent of the chord at the leading and trailing edges respectively. This data was useful in determining grid clustering in the present study.

Literature pertaining to grid resolution requirements for boundary layers has been reviewed by Moitra [38]. Two important considerations were the initial normal spacing and the stretching ratio. Moitra stated that the initial normal spacing at the surface must be small enough to provide at least three points in the linear sublayer ($y^+ < 5$). This implied an upper bound of approximately a y^+ of 1.5 on the upper surface. Other guidelines [39] stated that when the laminar sublayer was being resolved, then the y^+ at the wall adjacent cell should be $y^+ \approx 1$. However, a higher value of y^+ was acceptable as long as it was well inside the viscous sublayer ($y^+ < 5$). An upper limit on the value of the stretching ratio was established by Spalart [40] based on an analysis of optimal grid distributions with regard to truncation errors. According to this analysis, optimal grid distribution was obtained for geometric stretching ratio not exceeding 1.2.

The resolution of the wake regions was the most crucial requirement for accuracy of CFD predictions of high-lift flows [37]. The usual method was to assume *a priori* the location of the wake in the form of lines in the flowfield and to cluster points in the vicinity. The difficulty was in predicting the location of the wake. Thus this method may result in a waste of grid points at best and corruption of the solution as a result of a lack of resolution at worst. Moitra [37] stated that the origin of wakes was in the boundary layer, submerged in the boundary layer grid, and therefore were well resolved. As it moved downstream it moved away from the airfoil surface. Crucially a lack of grid resolution caused a rapid dissipation of the wake in this case. The wake half-width grows directly proportional to the streamwise distance [30, 31]. Also the velocity gradients in the boundary layer are hundreds and often thousands of times larger than the wake velocity gradients [37]. This led Moitra to conclude that it should be sufficient for grid spacing of several orders of magnitude greater than the boundary layer to resolve wakes.

Special attention was paid to the region behind a highly deflected flap where the flow was characterised by flow separation and massive flow reversal. These phenomena occupy a large spatial extent and cannot be adequately resolved by grid refinement of the near-body alone. The widely varying length scales associated with the flow phenomena in this region caused a solution-adapted grid to approach a uniform grid [38]. This was

seen in the solution adapted grid results presented by Walsh and Zingg [41]. The cell size in this box matched the cell size at the edge of the boundary layer of the flap. The grid convergence study conducted by Moitra [37] established a lower limit on the stretching ratio of 1.1 in this region. The corresponding cell size in the uniformly spaced box was approximately 0.25% of the chord. This analysis of optimum grid parameters conducted by Moitra was important for creating grids in this study that will be able to accurately capture the flow phenomena present in a high-lift configuration.

Spalart [42] presented guidelines for creating detached-eddy simulation (DES) grids for external flow applications. The DES method is aimed at modelling high Reynolds number separated flows. Spalart suggested a $y^+ = 2$ or less and a stretching ratio of 1.25 or less, for the RANS resolved attached boundary layer. Spalart defined the LES regions as regions that contained vorticity and turbulence at some point in the simulation that weren't boundary layers or thin shear layers along which the grid could be aligned. The grid spacing should be chosen to give adequate spatial resolution in the area of primary interest. According to Spalart, the least expensive way to obtain the desired resolution was to have cubic cells. For time step considerations, five time steps per period were recommended for the smallest resolved eddy in the LES region. These guidelines were followed in the creation of computational grids used in this present work.

2.4.4 Turbulence Modelling Issues

Godin and Zingg [43] assessed the Spalart-Allmaras one-equation [33] and the Menter two-equation [44, 45] turbulence models for RANS computations of high-lift aerodynamic flows. Cases considered were a separated flow over a single element airfoil at a high angle of attack, a fully-attached flow over an airfoil with a flap, and a separated flow over an airfoil with a flap. The Spalart-Allmaras turbulence model is a one-equation transport model for eddy viscosity. The Menter model combines the $k-\omega$ model with the $k-\epsilon$ model in a manner that exploits the best features of both [44]. It also includes the Shear Stress Transport (SST) model which accounts for the transport of principal turbulent shear stress in adverse pressure gradients [46]. This blends the robust and accurate formulation of the $k-\omega$ model in the near-wall region with the free-stream independence of the $k-\epsilon$ model in the far field [39]. The results of Godin *et al.* [43] showed the Menter model to be more accurate in separated flow regions. The Spalart-Allmaras model was more accurate in attached flows and wakes, including merging boundary layers and wakes. According to Godin and Zingg, the Spalart-Allmaras model was somewhat more robust and is therefore preferred for general computations of aerodynamic flows while the Menter model is the better choice if separated flows are of primary interest. As previously mentioned, in Section 2.4.2 Khorrami [34] used the Spalart-Allmaras turbulence model [33] with a solid-body rotation modification which produced better results for vortex dominated flows.

2.5 Flap Side-Edge Aeroacoustics

2.5.1 Experimental Studies

An experimental investigation was carried out by Macaraeg [47] at NASA Langley research centre into airframe noise mechanisms associated with high-lift devices. On-surface measurements included steady and unsteady pressure measurements, hot films, oil flow and pressure sensitive paint for flow visualisation. Off-surface measurements were five hole-probe, particle-image velocimetry, laser velocimetry and laser light sheet measurements. Microphone array measurements were used to obtain acoustic source maps on the model and quantitative spectra. The targeted frequency range was 2-30 kHz. The initially proposed noise generation mechanism was vibration of the flap side-edge vortical structure. According to Macaraeg, the laser light sheet data did not reveal significant vibration of this structure, although at low frequencies it was found to dominate the flap side-edge noise.

Source localisation maps from the large-aperture microphone array showed that at higher frequencies a source was localised on the edge of the flap. According to Macaraeg, this was consistent with the primary vortex grazing the edge of the flap. As the frequency decreased, the source moved downstream and inboard. This was due to the merged vortex system spilling over the side-edge and impinging on the upper surface of the flap. The shear layer instability was broadband in nature as the disturbance remained significant from 5 kHz ($St_F \approx 10$) to 30 kHz ($St_F \approx 63$)[2]. At lower frequencies, the vortex instability appeared to be stronger than that of the shear layer instability. From the 5 kHz noise map the maximum intensity occurred inboard of the flap side-edge at the location where the vortex moved rapidly over the side-edge and onto the suction surface. The high frequency noise maps indicated more maxima along the side-edge where shear layer instabilities were dominant. Macaraeg also found that an abrupt rise in noise intensity occurred following an increase in the flap deflection angle due to vortex bursting on the flap side-edge system. This reference was useful in determining noise generation mechanisms for a flap side-edge, namely cylindrical shear layer instabilities, instabilities in the primary vortical structure and vortex bursting. It was also useful in detailing acoustic source maps and quantitative spectra.

Brooks and Humphreys [48] performed an experimental study to investigate the sound generation mechanism of a flap side-edge. An acoustic database was obtained using a Small Aperture Directional Array (SADA) of microphones to obtain farfield noise spectra and directivity. The measurements revealed a dominant flap vortex structure that resulted from the merger of two upstream vortices; one strong vortex, formed on the pressure side which dominated the flap side-edge, and a weaker vortex formed at the

[2]Strouhal number is non-dimensionalised with respect to flap chord.

flap side edge on the suction surface. In the vicinity of the trailing edge, the vortex was far removed from the flap surface. Brook and Humphreys observed that as the flap side-edge was approached from inboard, the surface spectral levels increased. This trend of increasing spectral levels approaching the edge was opposite to that found for the classical turbulent-boundary-layer trailing-edge noise scatter problem. Therefore it suggested a different mechanism other than edge scattering [49].

Brooks and Humphreys [48] hypothesised a different mechanism consistent with shear layer instability models [32, 35] for noise production. This shear layer instability resulted in shedding of unsteady vortices from the flap side-edge and related pressure scatter. For higher flap angles the measured noise levels exceeded the predictions, which suggested additional contributions from surface sources that were not localised to the immediate flap side-edge region. This additional source was related to vortex bursting that occurred at high flap angles as observed by Khorrami *et al.* [32]. For a flat flap side-edge, Brooks and Humphreys [48] found a simple dipole directivity pattern at low frequencies and an approximate cardioid pattern for high frequencies. Contrary to thin edge scatter theory, the cardioid pattern was reversed with higher levels being found away from the extended flap side-edge. The explanation offered by Brooks *et al.* was that it was related to edge thickness to acoustic wavelength effects.

Meadows *et al.* [50] performed aeroacoustic measurements to investigate sound generation of a high-lift wing. The tests were performed on a NACA $65_2 - 215$ airfoil with a 30% chord half-span fowler flap. Flow speeds up to Mach 0.17 and Reynolds numbers up to 1.7×10^6 were tested. The measurement system included a Large Aperture Directional Array (LADA), to identify locally dominant noise sources by producing high spatial resolution noise source location maps along the airfoil surface; a Small Aperture Directional Array (SADA), to measure the directivity and spectra of selected portions of the wing-flap model; and unsteady surface pressure sensors, to quantify the wavenumber spectra over the surface and to correlate the surface pressure measurements with the farfield acoustic measurements. Like previous authors, Meadows *et al.* noted the presence of a dual vortex system. For the 39 degree flap deflection case the vortices were stronger and the side-edge vortex spilled over to the upper surface sooner. More interesting according to Meadows *et al.* [50] was the vortex bursting that occurred. Acoustic field maps obtained from the LADA measurements showed that the locally dominant noise source changed with frequency. A trend existed for low-frequency sound sources to be located near the flap trailing-edge. High-frequency sound sources were located near the flap mid chord for the 29 degree flap deflection case and near the flap-main element juncture for the 39 degree flap deflection case. According to Meadows *et al.* this trend of decreasing frequency with increasing streamwise distance was consistent with an increase in the scale of the dominant flow structures. This trend was also noticed by Kendall and Ahyte [6] who surmised that the growth of the flap side-edge vortex was

responsible for this trend.

From the SADA measurements it was found that for the 39 degree flap deflection angle, all spectra uniformly increased, typically 10 dB from the 29 degree flap deflection case, except for the very lowest frequencies. This level increase included the high frequency tonal features of the spectra. Meadows *et al.* [50] also noted additional broadband noise for the higher flap deflection angles that seemed to have a distinct Strouhal number dependence. This is characteristic of flow-surface interaction noise. The appearance of multiple broadband tonal features at high frequencies suggested that there was an altered flow condition at the flap side-edge that dominated the radiated noise field. The farfield directivity for the 39 degree flap deflection case was much less uniform in the streamwise direction compared to the relatively flat directivity for the 29 degree case. Analysis of the unsteady surface pressure measurements in the vicinity of the flap side-edge showed high coherence levels between adjacent sensors on the flap side-edge and the upper surface in the region where the side-edge vortex spilled over onto the upper surface. The frequency ranges where the high levels of coherence occurred were consistent with the frequency ranges where dominant features appeared in the farfield acoustic spectra measured by the SADA. Similar to Macaraeg [47], the flap side-edge vortex impinging on the suction surface of the flap was proposed as a mechanism for noise generation.

The split flap configuration contained an overlap region between the trailing-edge of the main element and the side-edge of the flap. This was referred to as the side-lap region by Choudhari *et al.* [51]. The side-lap region causes a high speed jet to flow through the gap region. This caused a strong shear layer that separated from the main element with an opposite sign of vorticity to that of the flap side-edge vortex. According to Choudhari *et al.* [51], this caused a flattening of the upper-surface flap vortex and delayed the merging between the two vortices.

From unsteady pressure transducer measurements, Choudhari *et al.* [51] found a relatively strong coherence in the frequency range of 1500 Hz ($St_F \approx 3.6$) to 4000 Hz ($St_F \approx 9.7$). From the phased microphone array measurements, the strongest noise source was a tone-like signal at slightly less than 5000 Hz, which corresponded to the trailing-edge of the flap, caused by the unsteady interaction between the merged vortex and the flap trailing-edge. As the frequency increased, the dominant noise source moved further upstream. These sources were associated with the turbulent shear layers.

2.5.2 Computational Studies

Streett [35] obtained a computational solution of the fluctuating flow field associated with the complex vortex system at the side of a flap in a multi-element wing system.

The goal was to estimate the spectral content of these fluctuations so that the spectrum of noise generated by such flowfields could be estimated. The fluctuations at the flap side-edge are broadband in frequency. Since the computational effort required to simulate unsteady phenomena is roughly proportional to the ratio of the highest to the lowest frequency, this led Streett to declare that the use of unsteady RANS to simulate these fluctuations was "out of the question" [35]. The first approximation used to estimate the origin and frequency content of the fluctuations was obtained using the Lighthill acoustic analogy [16]. According to Streett the primary noise generating fluctuations resulted from instabilities in the flow. Instabilities such as inflectional instabilities in shear layers resulted in the reorganisation of steady mean vorticity into fluctuating vorticity of potentially large amplitude. Streett suggested that the nonlinear interaction of these fluctuations in a rapidly-varying mean flow would be the mechanisms for noise generation.

Streett found two basic families of disturbance modes. The first was associated with the instability in the cylindrical shear layer, which overlies the side-edge separation in upstream stations, and feeds the trailing vortex in downstream stations. Streett proposed that the instability, strength, location and thickness of the cylindrical boundary layer were functions of configuration and loading. For the configuration examined by Streett, the shear layers over the two vortices present were relatively thin at 10 percent of the flap chord, which led Streett to expect higher frequencies to dominate. At 50 percent of the flap chord, the two vortices had merged and the cylindrical shear layer/vortex system was well established. The instability of the cylindrical shear layer was broadband in nature. Streett also noted that 5 kHz ($St_F \approx 12$) disturbances persisted with significant magnitude even as they were convected over the vortex.

The second disturbance mode was associated with the instabilities of the vortex and its "jet-like core" which possessed a significantly oscillatory structure in the streamwise direction. The dominant frequency band for these disturbances was considerably lower than that for the shear-layer instability. From the measured frequency spectra, the shear layer instability band was roughly 5 kHz ($St_F \approx 12$) to 30 kHz ($St_F \approx 73$), while for the vortex instability Streett found the band was roughly 1 kHz ($St_F \approx 2.4$) to 10 kHz ($St_F \approx 24$) with wavelengths corresponding to the order of 1/4 to 1/2 of the vortex diameter.

2.5.3 Vortex Breakdown

Numerous references have cited vortex breakdown as a mechanism for sound generation at high flap deflection angles. The following is an outline of references which examine the phenomenon. Vortex breakdown[3] classically refers to the appearance of a stagnation

[3]Synonymous with vortex bursting in this discussion

point on the vortex axis followed by a region of reversed flow [52]. Two categories of vortex breakdown have been identified. These are the axisymmetric bubble type and the asymmetric spiral type. Both involve a sudden expansion of the vortex core. Theoretical work conducted by Benjamin [53] showed that the phenomenon was a transition between two dynamically conjugate flow states. Harvey [54] performed a series of experiments and determined that vortex breakdown to be an intermediate stage of two types of rotating flows.

Bossel [55] challenged both these results and showed that the phenomenon was a regular solution to the linearised version of the axisymmetric incompressible Euler equations when retardation of the axial velocity and high swirl were introduced. Bossel showed that the breakdown was essentially an inviscid phenomenon and the swirl parameter was the determining factor as to whether or not vortex breakdown would occur. Grabowski and Berger [56] solved the Navier-Stokes equations for the breakdown of an unconfined viscous vortex. These results refuted the theory that the vortex breakdown was a finite reversible transition between two states. Further numerical results by Salas and Kuruvila [57] for axisymmetric breakdown showed that the swirl was the dominant parameter.

More recently, according to Gursul [58], it was generally agreed that the vortex breakdown phenomenon was a wave propagation problem and there was a strong analogy with shock waves in gas dynamics. Both experimental and theoretical explanations showed that swirl level and external pressure gradient outside the vortex core affected the occurrence and movement of vortex breakdown. Flow downstream of the vortex breakdown exhibited hydrodynamic instability. It was also observed in several experiments that the vortex breakdown location was not steady and exhibited fluctuations along the axis of the vortices.

2.6 Noise Generation Mechanisms

This is a summary of the major noise sources identified and proposed in the literature discussed above. Choudhari and Khorrami [59] list the noise producing features near the flap side-edge as free shear layers and their rollup, formation of multiple vortices, vortex merging, and vortex bursting when the flap deflection was sufficiently large. Various works mentioned in the above discussion outline two detached shear layers which roll up from the flap side-edge to form primary vortices as a noise source. Instability of these detached cylindrical shear layers, especially close to the lower surface, are considered as the source of high frequency broadband noise localised on the flap side-edge [8]. Both vortices merge further downstream to form a single side-edge vortex. According to Molin [8] this pairing, in itself, does not contribute significantly to the generation of noise.

The flap side-edge vortex was identified as a low frequency source radiated by interaction with the flap surface, mainly the suction surface close to the trailing-edge. This low frequency noise source was associated with the upper surface at the attachment line where the post-merged vortex impinged on the flap upper surface. Another low frequency noise source was associated with instabilities in the vortical structure itself in the streamwise direction. This was broadband in nature over a range of 1 – 10 kHz ($2.4 \leq St_F \leq 24$). A noise mechanism was associated with vortex bursting that was broadband and had tonal features at high frequencies.

The effect of edge scattering has been mentioned in the preceding discussion. Sound generated from dipole and quadrupole sources close to a sharp edge follows a scaling law of V_∞^5. In the absence of a sharp edge they would radiate proportional to V_∞^6 and V_∞^8 respectively [17]. The Brooks and Hodgson formula, which is based on a flat plate at zero incidence with a sharp trailing-edge, gives the farfield intensity as,

$$I \simeq \frac{\rho_\infty V_\infty^5}{2\pi^3 a_\infty^2} \frac{(u')^5}{V_\infty} \frac{S}{h^2} \frac{\ell_0}{\bar{c}} \,, \tag{2.6}$$

where u' is the fluctuation in velocity near the sharp edge, h is the distance from the trailing-edge to the observer and ℓ_0 is the corresponding correlation length of the acoustic source near the sharp edge. This formula has no angular dependencies and ignores Doppler effects associated with convection. Brooks and Hodgson used the boundary layer displacement thickness δ^* at the sharp edge for the correlation length. This relationship shows that the noise emitted is proportional to the volume of turbulence crossing the sharp edge. Possible noise reduction methods would be to reduce the volume to turbulence convecting past the sharp edge and to change the scattering by modifying the sharp edge [60].

Hardin [61] suggested that turbulence in the boundary layer that was convected around the side-edge was responsible for noise production. The magnitude of sound radiation was related to the strength of vorticity of the convected flow and its distance from the sharp edge. Turbulence convected past a sharp edge follows a V_∞^5 scaling law. However, in the measurements performed by Meadows *et al.* [50], the scaling law was found to be $V_\infty^{5.5}$ or higher at high frequencies. Since vortex merging and breakdown are low frequency phenomenon, this led the authors to conclude that shear layer instabilities were responsible for the bulk of the concentrated audible noise generation [50].

Sen [62] proposed the oscillation of the side-edge vortex as a mechanism for sound production at the side-edge. The frequency was dependent on circulation, edge thickness and mean distance from the edge. In Sen's model, the base vortex was perturbed using a smaller vortex to simulate the interaction between the side-edge vortex and upstream

unsteady flow structures. One of the conclusions of the vortex oscillation model was that when the vortical region was compact, i.e. far away from the flap surface, the vortices tended to move in a mutually cancelling manner, which resulted in low acoustic production.

A linear stability analysis was performed in the vicinity of a flap side-edge by Khorrami and Singer [63] based on a local meanflow determined from a RANS calculation. The two models proposed were cylindrical shear layer instabilities and streamwise vortex instabilities. The authors conjecture that the curved shear layer supported large scale flow perturbations. The fluctuations in the shear layer were brought close to the flap surface by the vortex velocity field. The fluctuations also amplified unsteady modes in the vortex. In the flow studied, peak amplification rates of vortex instabilities occurred for,

$$2 < \frac{\omega_r^* \, r_0}{V_\infty} < 4 \, , \tag{2.7}$$

where ω_r^* is the dimensionless real part of the angular frequency and r_0 is the vortex radius. The peak amplification rates correspond to $11 \leq St_F \leq 22$. The potential acoustic sources are summarised by Khorrami and Singer as follows [63].

1. Large scale flow fluctuations supported by a free shear layer emanating from the flap bottom edge and spanning the entire flap chord.
2. Large scale flow fluctuations supported by the post merged vortex downstream of the flap midchord region.
3. Convection of turbulent boundary layers past a sharp edge resulting in scattering and broadband sound radiation.
4. Vortex merging.
5. Vortex breakdown.

For the split flap configuration, Howe [64] formulated a model for the flow through the slot between the flap and the undeflected part of the main element. The gap between the side-edge of the flap and the undeflected main element was the main influence on the intensity of the radiated sound.

2.7 Noise Reduction Methods

This section outlines some of the potential noise reduction methods mentioned in the literature that have been applied to the flap side-edge problem.

2.7.1 Continuous Moldline Technology

Continuous Moldline Technology (CMT) involves a flexible panel that deforms to provide a continuous surface between two moveable parts. In a study conducted by Storms *et al.* [65], CMT was applied at the flap tip junction of a wind tunnel model comprised of a simplified wing with a half-span hinged flap. With an exposed flap tip a compact noise source was the dominant airframe source at high frequencies. CMT connected the flap side-edge to the adjacent wing surface with an elastomer panel that deformed during flap deflection to provide a continuous surface without abrupt changes in curvature. With CMT applied, the flap side-edge source was reduced below measurable levels. However, there was an aerodynamic penalty to be incurred since the application of CMT reduced the overall lift. This was due to the reduced loading on the main element near the flap side-edge.

2.7.2 Active Flow Control

A study was conducted by Koop *et al.* [66] on the reduction of flap side-edge noise by the use of active flow control. The source of noise at the flap side-edge was assumed to be the oscillation of the vortical structure at the flap side-edge. This led to pressure fluctuations at the rigid surface and thus to sound radiated to the farfield. One proposed method of reducing this noise was to displace or destroy the vortical structure by blowing air into it. This reduced the magnitude of surface pressure fluctuations and thus the amplitude of the radiated sound. According to Koop *et al.*, blowing air changed the circumferential velocity profile of the vortex and thus the dynamic interaction between the shear layer and the vortex instability. It also had the effect of displacing the vortical structure away from the solid surface, which reduced the sound pressure level and thus the amplitude of the radiated sound. Koop *et al.* showed using PIV measurements that with blowing the vortical structure had almost completely dispersed. The maximum vorticity in the vortex core was also reduced and moved away from solid surfaces. Using microphone array measurements Koop *et al.* found the sound pressure level in the acoustic farfield was reduced by 3 to 4 dB above 1.25 kHz.

2.7.3 Flap Edge Fences

According to Macaraeg [47] a low frequency noise source was located on the upper surface of the flap, which was a result of the post-merged vortex rolling around the side edge and impinging on the upper surface of the flap. A noise reduction scheme proposed by Horne *et al.* [67] used flap-edge fences to reduce the noise. The rationale underlying the use of a flap side fence was to increase the distance between the vortex system and the top surface of the flap. A series of studies conducted by Blackner and Davis [68] on a small-scale Boeing aircraft on approach used a large flap-tip fence extending above and

below the flap surface that reduced the peak noise levels by as much as 9 dB in the middle frequency range. Storms *et al.* [69] examined a lower tip fence that extended approximately one flap thickness below the flap lower surface. It was examined in flight tests by Ross *et al.* [70] on a general aviation aircraft. Measured directly overhead the noise reduction was 3 - 4 dB for frequencies between 4 kHz ($St_F \approx 25$) and 10 kHz ($St_F \approx 63$).

Guo and Joshi [71] performed airframe noise tests using a 4.7% DC-10 model. They found that the flap noise radiation was typically that of a dipole type caused by unsteady pressure fluctuations on the flap which resulted in a sixth power law velocity relationship. The effect of a flap side-edge fence on farfield noise was determined. Guo and Joshi found that in the high frequency range, the airframe noise was dominated by the separated shear layers in the flap crossflow [71]. These sources were found to be broadband in nature. According to Guo and Joshi, the exact mechanism by which noise was reduced by flap side-edge fences was not fully understood. The fences were shown to be most effective for high frequencies both with and without a slat. It was found that the amount of noise reduction did not increase linearly with fence height. Although flap side-edge fences were effective in reducing high-frequency noise it was found that they increased the noise level at low frequencies. Guo and Joshi postulated that the downward shift of dominant frequency was caused by the effective increase in flap thickness by the fences.

According to Choudhari and Khorrami [59], the flap side-edge fence delayed the roll-up of the shear layer and locked the position of the side-edge vortex near the bottom edge so that it could not merge with the vortex along the top edge and form a single dominant vortex. The side-edge fence was expected to add a small amount of weight to the high-lift system that would have to be carried during the entire flight. It may also have had a drag penalty associated with it.

2.7.4 Porous Materials and Brushes

Chow *et al.* [3] achieved a noise reduction by replacing part of the flap side-edge by brushes and also by an open cell porous edge. According to Chow *et al.* the combined effect of a porous flap side-edge and a slat cove filler (to eliminate the recirculation region in the slat cove)[4] demonstrated a noise reduction of more than 2 dB at some angles of emission on a $1/11^{\text{th}}$ scale model of an Airbus A320. For a flap side-edge with brushes there was a source strength reduction of approximately 5 dB. Aerodynamic tests were conducted to measure quantitatively the impact of these noise reduction methods on the aerodynamic characteristics. There was a slight decrease in $C_{L\,\max}$ in the order of 1%. Similar trends were found in pitch and roll moments. For a landing configuration, a slight increase in drag was measured, although the authors did not quantify this. For

[4]This is considered a source of slat noise

a take-off configuration Chow *et al.* observed a similar trend but with less impact due to the lower flap deflection angle in the take-off configuration.

Choudhari and Khorrami [59] performed steady-state Reynolds-Average Navier Stokes calculations to investigate porous side-edge treatment as a passive means for flap noise reduction. The authors postulated a dual mechanism for the effectiveness of the porous tip treatment. Firstly, the porous edge modified the local mean-flow due to flow leakage across the permeable skin. Secondly, there was a damping effect on pressure fluctuations near the flap side-edge, due to the finite impedance of the porous surface. The computational calculations were performed on a computational grid of 4.5×10^6 nodes distributed over 16 blocks. The Spalart-Allmaras and Menter's Shear Stress Transport (SST) turbulence models were used to establish that the inferred flow modifications were not specific to any particular turbulence model.

Choudhari and Khorrami [59] found that in the mid-chord region of the flap, the porous treatment weakened the main side-edge vortex. An effect of transpiration through the porous segments was to displace the side and top vortices and the connecting shear-layers away from the solid surfaces. In contrast to the untreated case, the interaction between the two vortices aft of the mid-chord region was a slow and benign process that took place far above the flap surface and never culminated in a fully merged single vortex. The porous surface treatment resulted in a milder variation in surface pressures along the flap side-edge. According to the authors this weakened a potential hot spot where high frequency, high amplitude pressure fluctuations would have been generated. A limitation of this work was that since the nearfield unsteadiness was not modelled, it was not possible to translate the above flow alterations into accompanying reductions in sound pressure levels. Importantly, the damping effect of the finite impedance of the porous material on the pressure fluctuations was not modelled. The application of the porous side-edge had two important effects to reduce the unsteadiness projected onto the flap edge surface. It diffused the local vorticity field prematurely and it pushed the source of hydrodynamic fluctuations away from the edge surface. Importantly it was found that the momentum flux associated with the leakage flow through the porous medium, had a negligible influence on the overall lift.

2.7.5 Fairings

The use of flap fairings led to a less violent vortex acceleration around the flap side-edge and therefore lower noise levels [72]. The fairing geometry reduced the strength of the flap side-edge flow by greatly increasing the edge thickness scale while increasing local edge turbulence intensities because of flow separation over the fairing.

2.8 Summary

A noise source located at the flap side-edge has been identified in the literature as an important contributor to airframe noise. Previous work has described the major flow features present at a flap side-edge and identified a mid-frequency noise source. Various noise reduction methods in the literature have been discussed. The use of a porous flap side-edge was shown to be effective in reducing the noise source associated with the flap side-edge. This present work contributes an experimental insight into the physics responsible for the flowfield and acoustic alterations with a porous side-edge. While previous work had identified the mean flow features computationally, this present work attempted to capture the unsteady flow and by the use of a FWH solver determine the aeroacoustics of the flap side-edge. The combination of experimental and computational approaches was used to attempt a better understanding of flap side-edge noise.

Chapter 3

Description of Experiments

This chapter outlines the experimental techniques employed in this research and a description of the wind tunnel model and apparatus. A series of wind tunnel experiments were conducted to investigate the aerodynamics and aeroacoustics of a flap side-edge and the effect of applying porous materials to this region. Previous experimental work [3, 47] had achieved noise reduction by replacing a part of the flap side-edge with brushes and an open cell porous edge, as discussed in Section 2.7.4. This present work was aimed at understanding the physical mechanisms by which this was achieved and understanding the flap side-edge noise generation mechanism.

3.1 Experimental Strategy

To begin with aerodynamic measurements of forces and surface pressures were performed to determine the aerodynamic performance of the wing-flap combination. To understand the potential noise sources at the flap side-edge flow, the unsteady flowfield in the vicinity of the side-edge was measured. This was done using particle image velocimetry (PIV), hotwire anemometry and on-surface microphone measurements. Three different porous treatments were then applied to the flap side-edge. The effect of the porous side-edge on the nearfield unsteady aerodynamics and aeroacoustics was measured using the aforementioned techniques. The aerodynamic penalty of applying the porous treatment to the flap side-edge was determined by measuring the aerodynamic forces on the model.

Another series of experiments were performed with a split flap configuration. This consisted of one semi-span flap extended and the other retracted to form an extended trailing-edge on the main element. The retracted flap also filled in the flap cove on the main element. This configuration altered the flowfield and aeroacoustics of the flap side-edge. The three porous materials were applied to the discontinuity that existed between the flap and the main element trailing-edge.

3.2 Wind Tunnel Model

The wing used in the experiments was of a high lift design with a fixed leading-edge and a half span trailing-edge flap, shown in Figure 3.1. The origin of the axis system was at the leading-edge of the main element in the $x - y$ plane and at the flap side-edge in the z direction. The chord of the main element was 0.71 m and the span was 1 m. The chord (c_F) and span (b_F) of the trailing-edge flap were 0.198 m and 0.5 m respectively. The maximum thickness (t_F) of the flap was 0.021 m. The reference length, based on the retracted chord of the model, was 0.8 m. The main element was machined from hardwood and the half-span flap was made from carbon-fibre skins and machined aluminium ribs. Attached to the wind tunnel model were two endplates machined from aluminium. The endplate dimensions were 1.5 m in the x direction and 0.5 m in the y direction with rounded edges as shown in Figure 3.1. The thickness of the endplate was 0.006 m. A fillet radius of 0.003 m was applied to all the edges on the endplate to avoid unwanted separation. A window was cut out of the endplate to allow a laser light sheet to illuminate the flap side-edge. The dimensions of this window were 0.38 m in the x direction and 0.2 m in the y direction.

The main element was fitted with 45 pressure taps along the mid-span and with 5 microphones; 3 around the nose and 2 in the flap cove region. The coordinates of the location of the on-surface microphones are tabulated in Appendix A. The half span flap was pressure tapped around the mid-span with 20 taps and also contained 15 taps in the spanwise direction. The locations of the pressure taps on the main element and semi-span flap are tabulated in Appendix A. The half-span flap also contained a microphone, flush mounted at the flap side-edge at $x_F/c_F = 0.27$. The positions of the two on-surface microphones are shown in Figure 3.2. The wind tunnel model with the split flap configuration is shown in Figure 3.3.

3.3 R.J. Mitchell Wind Tunnel

The experiments were conducted in the University of Southampton 3.5 m × 2.5 m wind tunnel. The tunnel was originally the number two tunnel at RAE, Farnbourogh. It was originally commissioned in 1937. It was moved to the University of Southampton in the early 1980's. The tunnel is a closed circuit return type with a closed working section. The cross section of the test section is rectangular with fillets in each of the corners. The fan consists of six blades and is driven by a 980 bhp motor. The wind tunnel incorporates an air conditioning unit that maintains the air temperature at 19 degrees C in the working section. The airconditioning unit was located after turn number four in the tunnel and spans the entire cross-section of the tunnel. The freestream turbulence level in the test section is less than 0.3% at 30 m/s [73]. A picture of the model in-situ

in the R.J. Mitchell tunnel is shown in Figure 3.4.

3.4 Measurement Techniques

3.4.1 Forces

The wind tunnel contained a six-component balance with Nutem load cells. Only lift, drag and pitching moment are presented in the results section. The force data was averaged over three runs. The repeatability for C_L and C_D was within 1.6% and for C_M the repeatability was within 2.1%. The angle of attack of the main element was set to ± 0.05 degrees. The freestream values of temperature, static pressure and velocity were averaged from the values at the beginning and the end of each run. The average variations between the start and the end of the run were ±0.5 °C for temperature, ±0.1 mmH_2O for pressure and ±0.01 m/s for velocity. The reference planform area used in the calculation of the coefficients was 0.8 m^2. The reference chord was 0.8 m. The tare corrections and blockage corrections applied to the force data are presented in Appendix B.

3.4.2 Surface Pressures

The pressures were measured using a ZOC22B (Zero, Operate and Calibrate) system from Scanivalve Inc. This system used individual silicon piezoresistive differential pressure sensors for each of the 32 sensors. Each pressure transducer was capable of measuring at 20 kHz. The range of measurement was 0 to 50 psi differential pressure. The input voltage was 15 VDC and the full scale output was ±2.5 VDC.

The procedure for obtaining the pressures is described as follows. Initially, a run was performed with the tunnel in the wind-off condition. This gave the zero value. The ZOC was then calibrated against a known input pressure by connecting each of the pressure sensors to a correct calibration pressure. In the operate mode each of the sensors was connected to the unknown pressure to be measured. The data was acquired using a Pi Research Ltd. Mistral system. The time averaged pressure was averaged over 30 seconds to obtain the mean pressure at each pressure tap on the model. The blockage corrections applied to the pressure coefficients are presented in Appendix B.

3.4.3 Particle Image Velocimetry

Particle Image Velocimetry (PIV) is a non-intrusive technique providing instantaneous velocity vector measurements in a cross-section of a flow. The fluid was seeded with

particles typically in the range 1 μm to 5 μm. The seeding particles needed to be small enough so that they followed the flow accurately. They also needed to be small in comparison to flow structures in the flowfield so that the velocity did not change significantly across the seeding particle. The quality of the data obtained was sensitive to the amount of seeding present in the flow, too little resulting in nothing been measured and too much resulting in a low signal-to-noise ratio.

The seeding particles in the plane of interest were illuminated with a laser sheet. The laser system consisted of two Gemini Nd:YAG lasers that were capable of running at 4 Hz, emitting 120 mJ pulses at 532 nm. The thickness of the laser sheet was varied. If the laser sheet was too thick, the illumination of the particles was not sufficient. On the other hand, if the laser sheet was too thin, the seeding particles had moved out of the measurement plane between successive images and therefore no data could be obtained. The laser was placed in a room on the port side of the working section. The laser sheet was pointed in a vertical plane through a glass window, which made up one wall of the working section and then through a second glass window that formed part of the endplate. The laser was mounted on a one-dimensional traverse that was placed parallel to the mean flow direction so that it could easily be moved from one plane to another. The PIV laser is shown in Figure 3.5. The camera was attached to a strut, which was mounted from the floor to the ceiling of the wind tunnel approximately 10 chord lengths downstream of the model. The position of the PIV camera attached to the strut is shown in the background of Figure 3.6. This allowed $y - z$ planes through the vortex core to be examined. The smoke generator was placed aft of the working section. This ensured the smoke had sufficiently diffused to ensure homogeneity in seeding levels by the time the smoke reached the model.

The images were recorded on a Dantec HiSense camera (type 13 gain 4). The camera had a resolution of 1280 $\times$ 1024 pixels. A 40 mm lens produced an image of approximately 180 mm $\times$ 150 mm. The measurement planes were in the $y-z$ plane so therefore there was a significant out-of-plane velocity component. This resulted in perspective error. Such errors are unavoidable without resorting to stereoscopic PIV techniques. An estimation of the perspective error is made in Appendix B.

The position of the seeding particles, illuminated by the laser sheet, were recorded on a Charge-Coupled Device (CCD) digital camera at two different times, approximately 20 μs apart. The exact timing depended on the laser sheet thickness and the freestream velocity. The cross correlation was performed on interrogation areas measuring 32 $\times$ 32 pixels. The horizontal and vertical overlap was 75%. The cross correlation was composed of two parts. Firstly, the cross correlation between images of particles in the first interrogation area with images of the same particles in the second area, which are referred to as particle pairs. Secondly, the cross correlation between images of particles in

the first interrogation area with images of different particles in the second area. These were random correlations that contributed to noisy peaks in the correlation plane. If an appropriate size of interrogation area was chosen, the displacement of each particle pair was approximately constant. This produced a prominent peak in the correlation plane, which gave a high signal to noise ratio.

The timestep was large enough so that the displacement of the particles were resolved accurately but small enough that the out-of-plane motion was small. The size of the interrogation areas was small enough so that the velocity gradients across them were negligible but large enough that they contained enough seeding particles to improve the accuracy of the statistical analysis. A peak validation of 1.2 was used to reject spurious vectors. The time averaged data was averaged over 300 images, which were sampled at a frequency of 2 Hz. This produced a vector map of 157 $\times$ 125 vectors. The physical resolution of the generated vector map was 1.2 mm $\times$ 1.2 mm. Non-dimensionalised with respect to the flap chord, this corresponds to a resolution of 6×10^{-3} in each direction.

3.4.4 Oil Flow Visualisation

A liquid suspension of titanium dioxide (TiO_2) in paraffin was used. The wind tunnel was run at the desired test condition until the solvent had evaporated. This left titanium dioxide powder streamlines on the surface.

3.4.5 On-Surface Microphones

The microphones for this application needed to be small in diameter, have a high dynamic range, have a large frequency bandwidth and low power consumption. The microphones used were Panasonic WM-60A omnidirectional condenser microphones with a diameter of 6 mm. These were flush mounted onto the surface of the model. The sensitivity was -44 ± 5 dB. The measurable frequency range was 20 - 20000 Hz. The operating voltage was 2 VDC provided by preamps. The signal to noise ratio was greater than 58 dB. The typical frequency response curve, supplied by the manufacturer, showed that the relative response was constant across the frequency range.

The microphones were calibrated using a pistonphone which produced a plane wave at 1000 Hz at an amplitude of 84 dB. Since the relative response of the microphone was constant over the frequency range this allowed the calibration to be applied across the frequency range to calculate the Sound Pressure Level (SPL).

3.4.6 Hotwire Anemometry

Constant Temperature Anemometry (CTA) was used to measure the spectral content of unsteady velocity perturbations in the flowfield. Hotwire anemometry is based on the cooling of a heated body by a flowfield. The convective heat transfer (Q) from a wire is a function of the velocity (V), the wire over-temperature ($T_w - T_\infty$) and the physical properties of the fluid. The following relationship was proposed by King [74] for a cylindrical wire.

$$Q = (T_w - T_\infty) A_w \, h = A + BV^n \, , \tag{3.1}$$

where $n \approx 0.5$, A_w is the wire area and h is the heat transfer coefficient. A and B are calibration constants.

A single hotwire was used for velocity measurements. The main advantages of CTA are a fast response, high spatial resolution, high dynamic range, and a continuous signal. There is also a small disturbance to the flow due to the diminutive size of the hotwire. The probe used had a 3 mm long platinum plated tungsten wire sensor. The diameter of the wire sensor was 5 μm. The wire ends were copper and gold plated to a thickness of between 15 μm and 20 μm. This resulted in an active sensor length of 1.25 mm. The effect of the plating on the wire ends was to help in the accurate definition of the length of the wire and also to aid in heat dissipation by the prongs. This resulted in a more uniform temperature across the wire.

The recommended overheat ratio for wire probes in air was 0.8 [75], which corresponded to an over-temperature between 200 K and 300 K. An analog to digital converter was used to convert the voltages from the Wheatstone bridge to a digital signal. An electronic test, which utilised a small voltage square wave, was used to check the frequency response of the Wheatstone bridge. The optimum circuit response was determined by Freymuth [76] and is shown in Figure 3.7. From this frequency response, the bandwidth was able to be estimated.

The hotwire probe was placed on a one-dimensional traverse placed vertically, which allowed the hotwire to traverse through the vortex core. This allowed the spectral content of the unsteady flow, induced by the flap-side edge, to be determined. The hotwire was calibrated in freestream using a pitot-static tube connected to a digital micromanometer. The freestream turbulence intensity was less than the 0.5% as recommended by Bruun [77]. The calibration was performed from 0 m/s to 36 m/s in steps of 3 m/s. The average error in the hotwire for the calibration run was 0.32%. A picture of the hotwire setup is shown in Figure 3.8.

3.4.7 Phased Microphone Array

The model was tested in a closed test section, hard-walled wind tunnel, which made acoustic measurements difficult. Problems included turbulent flow over the microphones, high background noise levels and apparent noise sources due to reflections from the hard wind tunnel walls. Therefore, the location of on-surface microphones had to be carefully chosen. An array of microphones was used to obtain a noise source distribution in the spatial domain. The array consisted of electret microphones instead of more expensive instrumentation-grade microphones. This made accurate qualitative data difficult to obtain. The array was designed on the principle of a multi-arm logarithmic spiral, where the location of the microphones were chosen by a log-spiral intersecting a series of concentric circles. This ensured that the vector spacing between any two microphones was not repeated, which prevented the spatial aliasing effects from summing together. Multi-arm log spiral arrays are prone to sidelobes, or phantom images. The levels of the sidelobes increase as the frequency of the source increases.

The array consisted of 63 microphones. The aperture of the array (the longest dimension that encompassed all the sensors) was 0.7 m. The resolution of the array (the finite size of a point source as it appeared on a beamforming plot) was 0.85λ for a scan plane parallel to the array, at a perpendicular distance of 1 m from the array. A porous cloth was applied over the array to smooth the flow over the microphones. The microphones had a variable gain preamplifier. This ensured the signal to noise ratio was optimised for each microphone. A high pass filter was used to remove the low frequency boundary layer noise from the measured signal. The variable gain was set to 30 dB to avoid overloading the preamplifier at a freestream velocity of 30 m/s. The microphones were calibrated using a pistonphone which produced a plane wave at 1000 Hz at an amplitude of 84 dB. Since the relative response of the microphone was constant over the frequency range this allowed the calibration to be applied across the frequency range.

The data acquisition equipment used was National Instrument's 24 bit Dynamic Signal Acquisition. The data acquisition was controlled by Labview 7.1 software, which defined parameters such as block size and sample rate. A typical run was done at a sampling rate of 48 kHz. 100 blocks were acquired each of which contained 2048 samples. The post processing technique used was frequency domain beamforming. Beamforming theory assumes that the focus point is a discrete point source and that other sources do not interfere. The phased microphone array was placed on the floor of the wind tunnel facing the suction surface of the flap as shown in Figure 3.9. The scan plane of the array was aligned with the flap deflection angle as shown in Figure 3.10.

3.5 Summary of Test Conditions

The range of Reynolds numbers tested were 7.0×10^5 to 2.0×10^6, based on the reference length. The angle of attack range was 0 degrees to 15 degrees and the flap deflection range was 29 degrees to 39 degrees. A summary of the experiments performed are tabulated in the following tables.

Baseline	Forces	Oil Flow	Press.[1]	HWA	PIV	MICS	PMA
Hardwall	✓	✓	✓	✓	✓	✓	
Porous	✓			✓	✓	✓	

TABLE 3.1: Baseline Experiments.

Split Flap	Forces	Oil Flow	Press.	HWA	PIV	MICS	PMA
Hardwall		✓			✓	✓	✓
Porous					✓	✓	✓

TABLE 3.2: Split Flap Experiments.

[1] On-Surface Pressures

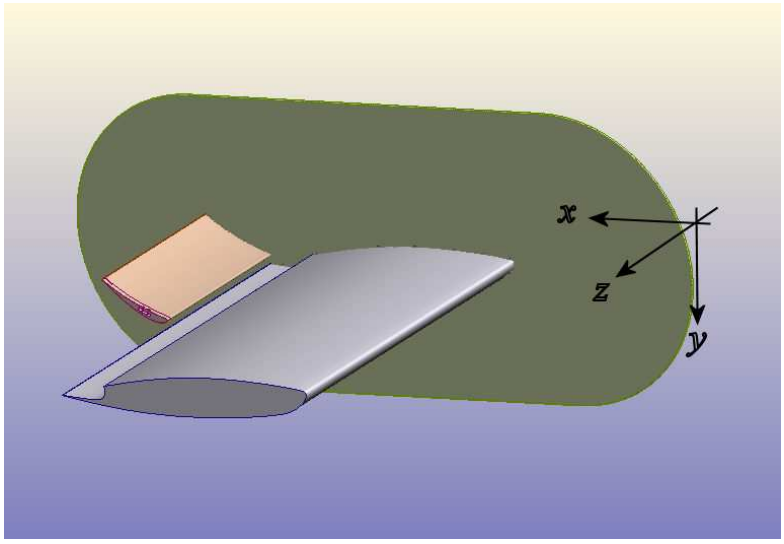

FIGURE 3.1: Wind tunnel model with port endplate removed. Flow is from right to left.

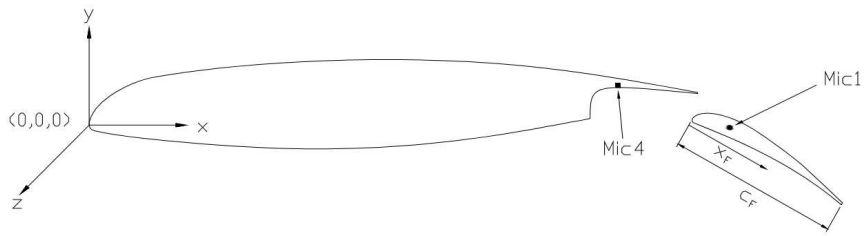

FIGURE 3.2: Geometry showing the definition of axes and location of microphones. Flow is from left to right.

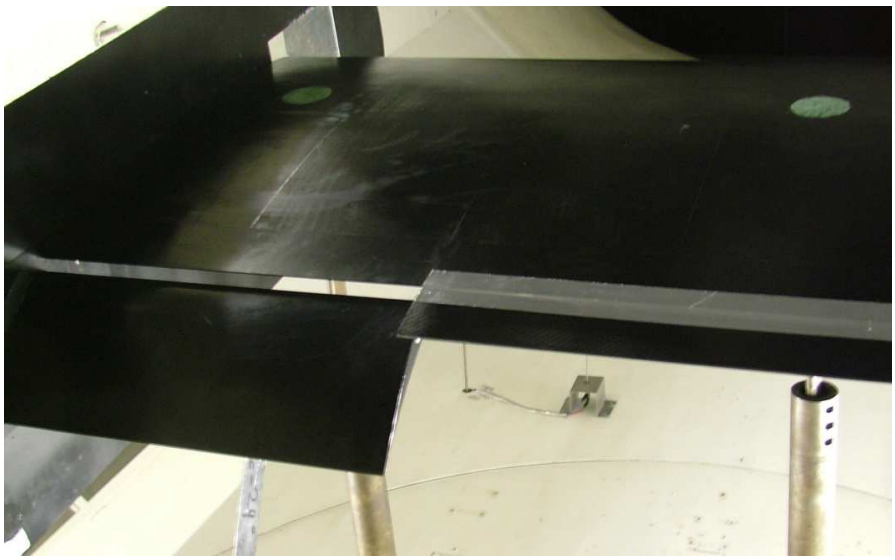

FIGURE 3.3: The split flap configuration with a second semi-span flap retracted to fill in the main element cove and extend the main element trailing-edge. View looking upstream and down on the suction surface.

FIGURE 3.4: The wind tunnel model in-situ in the R.J. Mitchell wind tunnel.

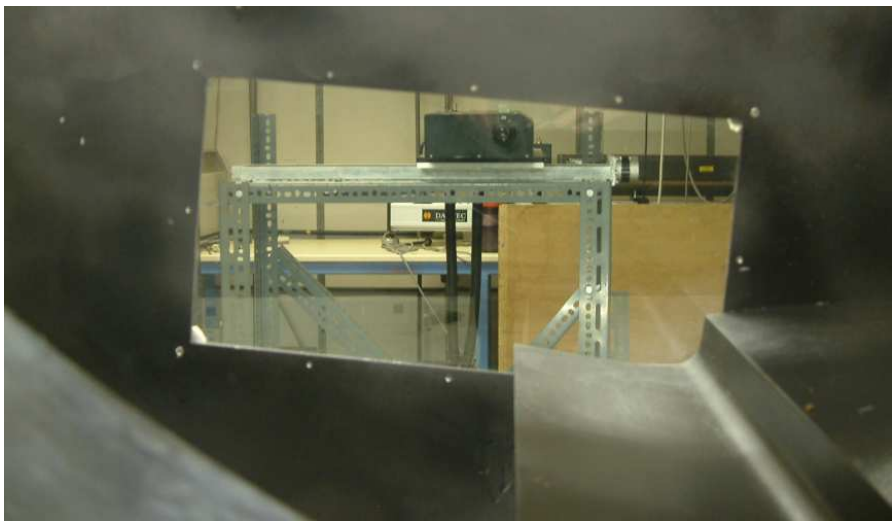

FIGURE 3.5: A view of the PIV laser through the starboard endplate window. Flow is from right to left.

FIGURE 3.6: A downstream view of the porous flap side-edge. The PIV camera can be seen mounted on the strut in the background. The laser sheet shines from right to left in a vertical plane.

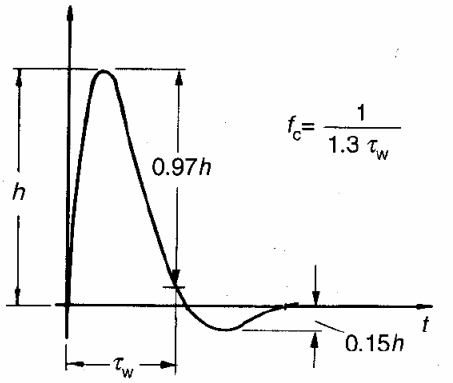

FIGURE 3.7: Optimum square wave frequency response [75].

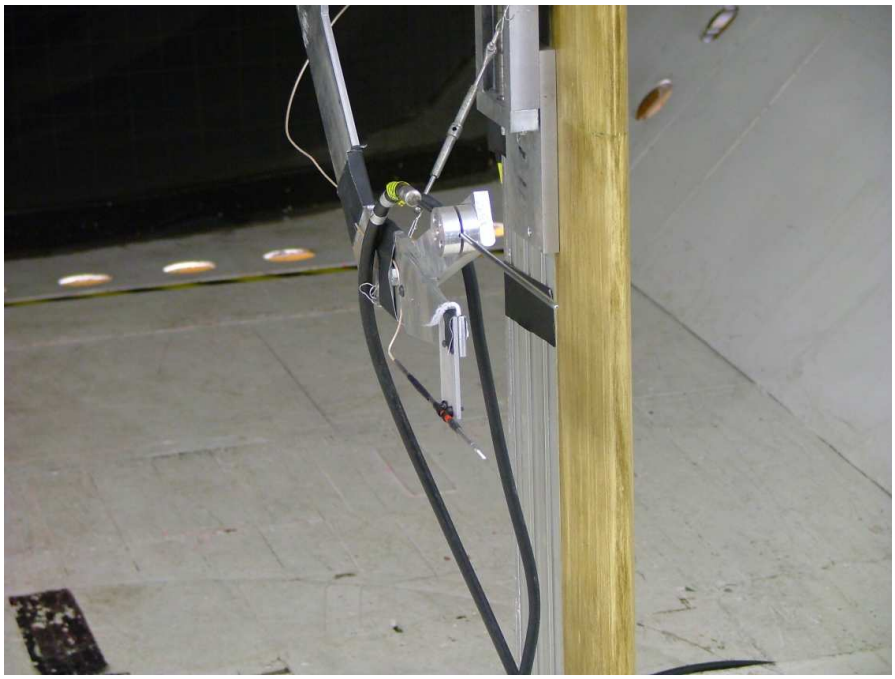

FIGURE 3.8: A view of the hotwire setup mounted on the one-dimensional traverse. The pitot-static tube is located above the hotwire probe and was used for calibration. View looking downstream.

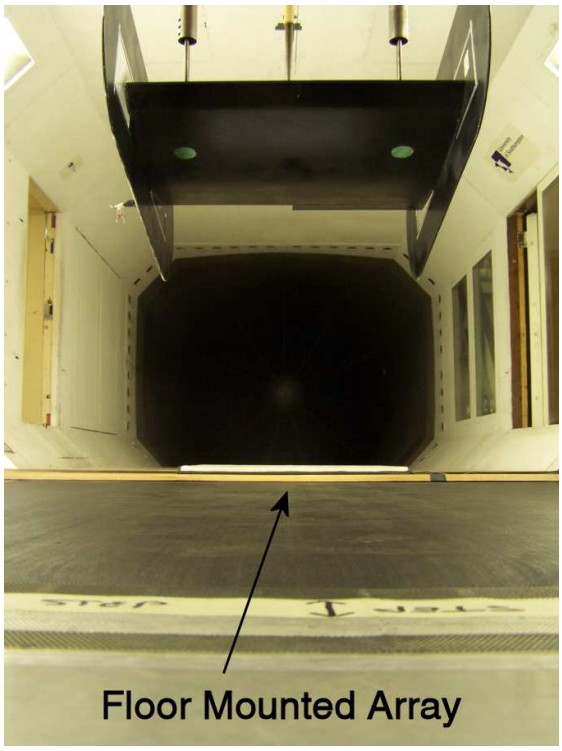

FIGURE 3.9: Phased microphone array mounted in the working section of the wind tunnel.

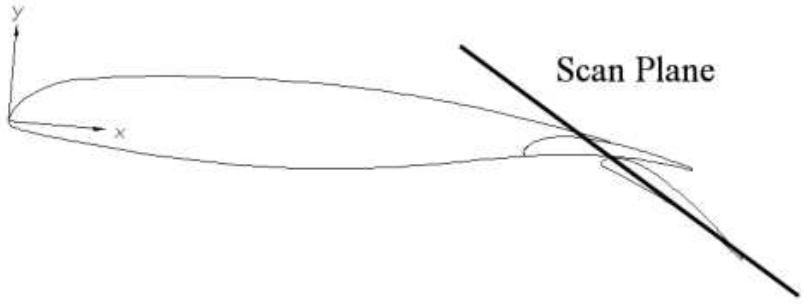

FIGURE 3.10: Location of scan plane for phased microphone array measurements.

Chapter 4

Experimental Results for Hardwall Case

This chapter outlines experimental results obtained in the R.J. Mitchell Wind Tunnel. These tests were performed with no treatment applied to the flap side-edge. The purpose of these tests was to investigate the aerodynamic flowfield and to gain a greater understanding of the physics responsible for noise generation at the flap side-edge. The hardwall experiments also provided a baseline for comparison with the results in Chapter 5 with the porous side-edges applied and Chapter 6 with the split flap configuration.

4.1 Forces

The lift, drag and pitching moment results are shown in Figures 4.1 - 4.3, adjusted for wind tunnel blockage correction factors [78] as calculated in Appendix B. The lift results showed little Reynolds number dependence. Increasing the Reynolds number from 0.7×10^6 to 2.0×10^6 resulted in an offset in C_L of 0.002 on average across the angle of attack range measured. The lift curve had a linear response up to an angle of attack of 20 degrees. This indicated that the two-element geometry did not stall up to this angle of attack. The drag values showed a slight Reynolds number dependence. The flap had a small region of separated flow towards the trailing-edge, as discussed in the oil flow visualisation results presented in Section 4.3.1. The position of this separation point had a slight dependence on Reynolds number over the range measured. The higher the Reynolds number, the further aft along the flap chord the separation occurred. This resulted in a slight reduction in the wake size, which resulted in a small reduction in drag. Increasing the Reynolds number from 0.7×10^6 to 2.0×10^6 resulted in an reduction in C_D of 0.019, averaged over the angle of attack range.

The pitching moment was measured about the mount points on the main element, which were located at $x = 0.26$ m. The pitching moment was defined as positive about the z-axis, i.e. nose down. Initially due to the deflection of the flap, the centre of pressure was located significantly aft of the mount points and therefore resulted in a positive pitching moment coefficient. As the angle of attack of the main element increased, the separation on the flap covered more of the suction surface. This caused a reduction in loading on the flap, which resulted in the centre of pressure moving forward towards the pivot points, thereby reducing the pitching moment. This region of the pitching moment coefficient curve showed significant Reynolds number dependence since the centre of pressure was dependent on the separation location on the flap suction surface.

4.2 Surface Pressures

The results for the pressure distribution over the main element and the flap at two different angles of attack at a Reynolds number of 1.1×10^6 are presented in Figure 4.4. Just aft of the peak suction on the nose of the main element there was a separation bubble. This was indicated by a small decrease in the surface pressure before the bubble at $x/c = 0.02$. The pressure distribution flattened over the length of the bubble and was then followed by a sharp adverse pressure gradient at $x/c = 0.06$. This point corresponded to the end of the bubble where the turbulent flow reattached to the surface. The presence of the flap cove at $x/c = 0.72$ can be seen on the pressure surface of the main element. Immediately behind the cove the flow was separated and this caused a decrease in the pressure. The pressure then increased towards the point where the shear layer reattached onto the cove surface. As the flow accelerated through the flap gap, the pressure again decreased. The pressure distribution in the cove region appeared not to be influenced by the angle of attack, within the range of angles measured. Oil flow visualisation, presented in Section 4.3.1, showed that the flow was clearly separated at this spanwise location. However, it was difficult to detect the separation point on the pressure distribution over the flap at both angles of attack. The spanwise pressure distribution on the flap is shown in Figure 4.5. At $y/b_F \leq 0.1$ the pressure distribution showed a large and sudden decrease in pressure. This was due to the low pressure in the vortex core. The on-surface pressures on the flap are useful for validating the CFD results in Chapter 8.

4.3 Flap Side-Edge Flowfield

4.3.1 Surface Flow Visualisation

Near the leading-edge of the flap, evidence of a dual vortex system can be seen in the oil flow visualisation given in Figure 4.6. The main vortex separated from the lower edge of the flap and reattached along the primary attachment line. Because of the sharp edge, the separation line was fixed at the bottom edge. At the upper edge of the flap a secondary vortex separated from the sharp edge and reattached on the suction surface of the flap on the secondary vortex reattachment line, as indicated in Figure 4.7. The main vortex grew rapidly in size in the streamwise direction as evidenced by the primary attachment line moving towards the suction surface of the flap side edge. At the primary attachment line, the flow stagnated and bifurcated into streamlines that flowed towards the upper and lower surface. The flow above the primary attachment line separated from the upper edge to form a secondary vortex, which reattached on the suction surface of the flap. The flow on the lower half of the primary attachment line separated at the secondary separation line before it reached the lower edge. This is shown in the schematic in Figure 4.8. This formed a small region of separation that grew slowly in the streamwise direction just above the lower edge of the flap, since it was dominated by the stronger primary vortex on the side-edge. As the vortices on the side-edge and upper surface merged, they separated from the flap surface.

A focal point was situated between the side-edge and the suction surface of the flap at approximately two thirds of the flap chord. This was evidenced by an accumulation of oil during the run. Aft of this focal point the flow was reversed as seen in Figure 4.7. Khorrami *et al.* [34, 32] noted a similar phenomenon located entirely on the side edge. In the oil flow performed in this experiment the location of the focal point was higher up and had moved onto the suction surface. This was caused by a change in the spanwise location of the off-surface vortex.

4.3.2 Formation and Evolution of Vortical System

The nearfield formation and evolution of the vortex was examined using PIV in five $y - z$ planes along the flap chord, which are tabulated in Table 4.1. The nearfield flow structures were then related to the nearfield unsteadiness and potential acoustic sources. Similar flow features were found as reported by other authors [32].

The presence of a dual vortex system and vortex merging were captured. The off-surface vortex, one chord length aft of the flap trailing edge, was also examined using PIV for both the hard wall and the porous side-edge cases. The PIV measurements showed significant displacements of the vortex core. This unsteadiness was caused by the unsteady

PIV Plane	x_F/c_F
1	0.2
2	0.4
3	0.6
4	0.7
5	0.8

TABLE 4.1: PIV planes.

flow originating upstream of the flap. A shear layer separated from the sharp cusp in the flap cove region on the main element. This shear layer had an inflectional instability, which led to a low frequency pressure disturbance in the cove region. The vorticity that was produced in the shear layer was convected through the flap gap above the flap suction surface. Vorticity was also shed from the blunt main element trailing-edge. These two sources of vorticity contained different length scales and were convected at different speeds. They interacted above the flap suction surface to produce a significantly unsteady flowfield. Another source of vorticity was in the separated wake of the flap on the suction surface. Therefore, the flap side-edge vortex was formed in a highly unsteady flowfield caused by all the non-linear interactions of vortical flows. This unsteady flowfield was computed in Chapter 8. This provided the necessary perturbations for the instabilities to grow. The proposed sources of vorticity in the $x-y$ plane are shown schematically in Figure 4.9. The potential acoustic sources arising from vorticity-surface interactions are illustrated schematically in Figure 4.10. These will be discussed as they arise in the PIV measurements. The vorticity is non-dimensionalised as follows,

$$\Omega = \frac{\omega\, c_F}{V_\infty}\,. \tag{4.1}$$

Plane 1 for the hardwall case is shown in Figure 4.11(a). The presence of a dual vortex system with the primary vortex attaching on the flap side-edge and a significantly weaker vortex on the suction surface can be seen. The shed vorticity from the wake of the main element can also be seen. The deflection of this wake due to the presence of the vortex was minimal at this plane since the strength of the vortex was small. Significant on-surface unsteadiness was produced where the turbulent shear layer impinged on the flap side-edge as shown schematically in Figure 4.10(a). Plane 2, which corresponded to the point of vortex merging, is displayed in Figure 4.11(b). At this plane the primary vortex attachment line moved to the suction surface of the flap. The effect of the vortex on the main element wake can be seen in this plane. Due to the induced flowfield caused by the vortex, the wake vorticity was displaced away from the surface outboard but brought closer to the flap surface inboard of the side-edge. As the vortex grew in strength and separated from the flap surface, the main element wake vorticity was wrapped around the vortex and convected onto the solid surface of the flap. This non-linear interaction of vorticity was a significant source of unsteadiness and led to a significantly unsteady

vortex. This is illustrated in Figure 4.10(b).

The third plane is displayed in Figure 4.11(c). This plane showed the vortices merged into a single large vortex whose reattachment point was on the flap suction surface. The vortex grew rapidly in the streamwise direction and the strength of vorticity in the shear layer increased. Plane 4, which is shown in Figure 4.11(d), showed the vortex was detached from the surface. As the vortex grew in strength, the seeding particles were forced from the centre of the vortex due to the centrifugal force of the spinning vortex. This can clearly be seen by the lack of vectors in the vortex core. Also due to reflections of the laser sheet from the solid flap side-edge, there was a small vertical band where no PIV data was obtained. The unsteady pressure field induced by the off-surface vortex interacted with the flap suction surface and sharp side-edges as illustrated in Figure 4.10(c). The fifth and final plane, just upstream of the trailing-edge, is displayed in Figure 4.11(e). The vortex exhibited significant unsteadiness constantly fed from the shear layer that originated from the lower surface of the flap side-edge.

4.4 Spectral Content of Off-Surface Vortex

Hotwire measurements were made of the vortex core and the surrounding flow five chord lengths downstream of the flap trailing edge. This was to determine the unsteadiness inherent in the fully-formed, off-surface vortex for the hardwall case. The frequencies are non-dimensionalised as follows,

$$St_F = \frac{f\, c_F}{V_\infty} \,. \tag{4.2}$$

Three different y positions were measured, which corresponded to the centre of the vortex core at three specific test conditions. These are tabulated in Table 4.2.

Hotwire Position	*Vortex Core at Test Conditions*
1	α= 5°, δ_F = 29°
2	α= 10° , δ_F = 29°
3	α= 10°, δ_F = 39°

TABLE 4.2: Hotwire positions.

At the first position measured, the vortex showed a strong tonal feature at a frequency of 670 Hz ($St_F = 13.2$) before the drop off in the energy cascade. The main element angle of attack was 5 degrees and the flap deflection angle was 29 degrees (Figure 4.12(a)). As the main element angle of attack was increased to 10 degrees (Figure 4.12(b)) a tone appeared at 270 Hz and a smaller broadband like peak centered around 470 Hz ($St_F = 9.3$). This was due to the change in trajectory of the vortex as the main element

angle of attack was increased. At an angle of attack of 5 degrees, the hotwire probe was in the centre of the vortex. At an angle of attack of 10 degrees, the hotwire probe was outside of the vortex. As the vortex moved even further away from the hotwire probe the velocity fluctuations dissipated rapidly (Figure 4.12(c)). The low frequency feature measured at 470 Hz ($St_F = 9.3$) on the edge of the vortex was due to instabilities that originated in the flap cove region. The frequency at this airspeed matched the frequency measured in the flap cove by the on-surface microphone presented in Section 4.5. This suggested that this unsteadiness was driven by flow that originated in the flap cove on the main element.

The second position corresponded to the centre of the vortex at an angle of attack of 10 degrees and a flap deflection angle of 29 degrees. A feature at a Strouhal number of 13.2 based on flap chord was measured at the higher Reynolds numbers due to unsteadiness of the vortex downstream of the flap trailing-edge (Figures 4.12(d) and (e)). PIV measurements of the downstream vortex showed large displacements of the vortex. This feature was also measured by the microphone on the flap surface near the trailing-edge. At a Reynolds number of 0.7×10^6, the hotwire spectra in Figure 4.12(c) showed a tonal peak at a Strouhal number of 10. As the Reynolds number increased to 1.4×10^6 and 2.0×10^6, the frequency of this peak increased to a Strouhal number of 13.2 at both Reynolds numbers. As the Reynolds number increased the width of the peak also increased. This result showed the importance of Reynolds number on the instabilities in the flap side-edge vortex.

The third position corresponded to the edge of the vortex at 10 degrees angle of attack and 39 degrees flap deflection angle. The low frequency tonal instabilities of the laminar vortex core were no longer measured as distinctly as before. Instead mid-frequency instabilities that were slightly more broadband in nature were measured. At 20 m/s (Figure 4.12(g)) three broadband peaks occurred from approximately 2 kHz ($St_F \approx 20$) to 5 kHz ($St_F \approx 50$). These features were due to shed vorticity in the turbulent shear layer that impinged on the flap side-edge. These measurements corresponded to on-surface microphone measurements of the reattachment point of the turbulent shear layer in Section 4.5.

4.5 Nearfield Pressure Fluctuations

On-surface microphone measurements were made on the main element cove and on the flap side-edge using omni-directional microphones to determine the nearfield pressure fluctuations. Furthermore, microphones were placed in different locations around the model and test section, to determine tonal components of the spectrum that were clearly due to noise associated with running the wind tunnel and not aerodynamic phenomena

associated with the model.

Four microphones were used to record the nearfield acoustics. Mic 1 was flush mounted on the flap side-edge at $x_F/c_F = 0.27$, Mic 2 was placed on the tail bar pointing towards the flap side-edge at $x_F/c_F = 0.8$ and Mic 3 was flush mounted on the starboard endplate pointing towards the flap side-edge at $x_F/c_F = 0.4$. Mic 4 was flush mounted on the main element flap cove at $x = 0.623$ m, to measure the unsteadiness upstream of the flap in the cove region.

In the cove region weak tonal features were measured at 460 Hz ($St_F = 9.1$) and 1120 Hz at 10 m/s with Mic 4, as shown in Figure 4.14(c). As the airspeed increased to 20 m/s these tonal features were lost beneath the boundary layer noise of the flow over the microphone. The origin of these tones was the unsteady pressure field induced by the inflectional instability of the shear layer. The instabilities at this point, due to the shed vorticity from the cove, were important as they were convected through the flap gap and interacting with the side-edge vortex. Mic 2, which was located near the trailing-edge of the flap, showed a feature at a Strouhal number based on flap chord of 13.2. This feature corresponded to the hotwire measurements made in the downstream vortex.

For the hardwall case the most notable feature in the spectra was the presence of a broadband hump measured from the microphone flush mounted to the flap side-edge (Mic 1). The characteristics of this feature depended on airspeed and flap deflection angle. This broadband hump was centered around a frequency of 4000 Hz. This broadband hump was due to the impingement of the turbulent shear layer onto the flap side-edge. The microphone was placed on the primary attachment line determined from the oil flow at a flap deflection angle of 29 degrees. At the flap deflection of 29 degrees the broadband peak was centered around 69 dB at 4050 Hz (Figure 4.13(a)). As the flap deflection angle increased to 39 degrees the broadband peak was centered around 60 dB at 4200 Hz (Figure 4.13(b)). The reason for the reduction in Sound Pressure Level (SPL), at the increased flap deflection angle, was that the microphone was no longer directly on the primary attachment line. The slight shift in frequency indicated a decrease in the length scales responsible for the disturbance due to the modified flow velocities around the flap side-edge at the higher deflection angle.

As the airspeed increased to 20 m/s, there was a double peak in the broadband hump. This suggested that there were two length scales responsible for the nearfield noise. At a flap deflection angle of 29 degrees the second peak was dominant at 4500 Hz and 89 dB (Figure 4.13(c)). At the 39 degrees flap deflection case a new peak appeared at 7200 Hz at a magnitude of 76 dB. At an airspeed of 30 m/s (Figure 4.13(e)) the broadband feature displays three distinct peaks at a flap deflection angle of 29 degrees. The third peak was at a frequency of 6500 Hz and a magnitude of 94 dB. As the flap deflection

angle was increased to 39 degrees the three peaks merged into two distinct peaks (Figure 4.13(f)). The second peak was centered around 8500 Hz and had a magnitude of 88 dB. This broadband hump showed dependence on the flap deflection angle and airspeed but was insensitive to the main element angle of attack.

4.6 Summary

The aerodynamic properties of a high-lift wing equipped with a half span flap were determined by means of on-surface pressures and by measuring integrated quantities like forces and moments. PIV was used to examine the formation of the vortex. Oil flow visualisation was performed in conjunction with the PIV to determine the nearfield flow. From the flow visualisation and PIV measurements three potential noise sources were proposed at the flap side-edge. Firstly, near the leading-edge, the turbulent shear layer that separated from the pressure surface of the flap, attached to the side-edge. An on-surface flush mounted microphone was placed at this attachment point to measure the unsteadiness caused by the impingement of the turbulent shear layer. Secondly, near the mid-chord of the flap, the dual vortex system on the flap side-edge had merged to become a single vortex. The attachment point of the turbulent shear layer had now moved to the upper surface. The location of the source and the length scales responsible for it had changed. Thirdly, as the trailing edge was approached, the vortex was located off-surface above the flap side-edge. The vortex exhibited a low frequency instability due to unsteady flow originating upstream of this point. This caused pressure perturbations from the unsteady vortex to interact with the sharp flap side-edge and trailing edge. There was no evidence of vortex bursting in these measurements.

From the hotwire measurements, the vortex downstream of the flap exhibited low frequency instabilities centered around a Strouhal number based on flap chord of 9.3. This corresponded to the on-surface microphone measurements in the cove region of the main element where a similar frequency was measured. This suggested that the low frequency instabilities in the downstream vortex were dominated by unsteadiness originating upstream of the flap. As the hotwire was moved towards the core of the vortex a large broadband peak was detected at a Strouhal number of 13.2. This was due to instabilities in the vortex core downstream of the flap. This spectral feature was also measured by an on-surface microphone near the flap trailing-edge. At higher airspeeds and flap deflection angles, the spectra demonstrated mid frequency features between 2000 and 5000 Hz. The frequencies matched those measured by the on-surface microphone at the flap side-edge. The origin of these instabilities was shed turbulence from the flap side-edge.

Although the mid frequency disturbances were small as measured by the hotwire far downstream, they dominated the nearfield. The on-surface microphone, located at the

primary vortex attachment line, showed a broadband hump between 2000 Hz and 7000 Hz depending on airspeed and flap deflection angle. The effect of increasing the flap deflection angle was to decrease the magnitude of these disturbances, since the vortex separated from the flap surface further upstream. Therefore, for the 39 degree flap deflection case the vortex was already off-surface and therefore the shed turbulence was moved further away from the on-surface microphone.

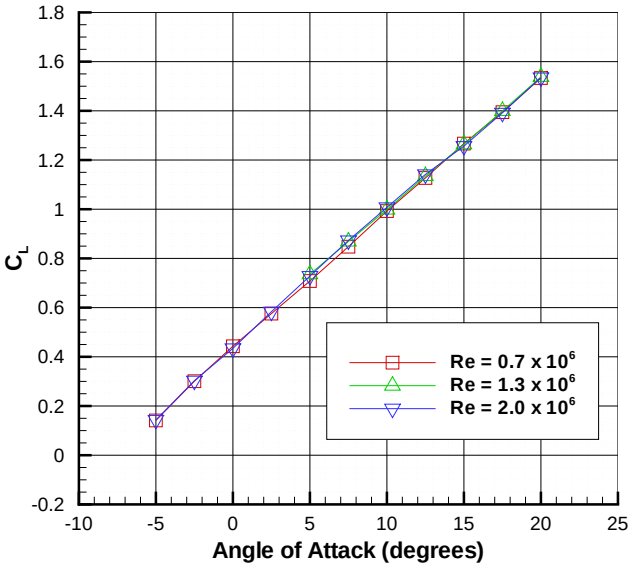

FIGURE 4.1: C_L variation with angle of attack.

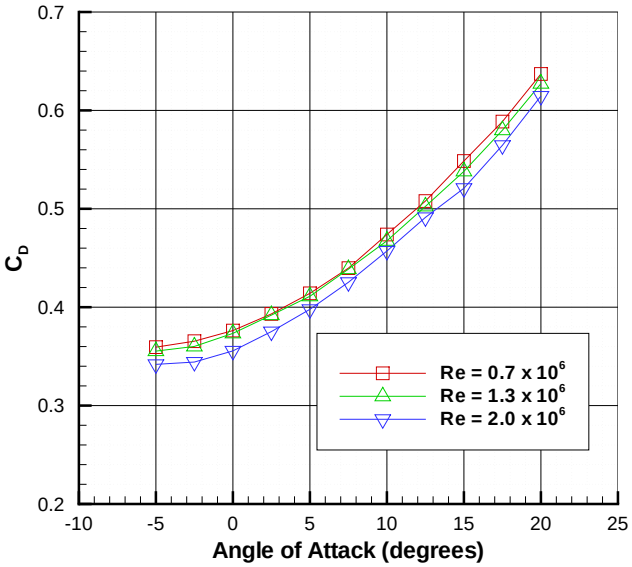

FIGURE 4.2: C_D variation with angle of attack.

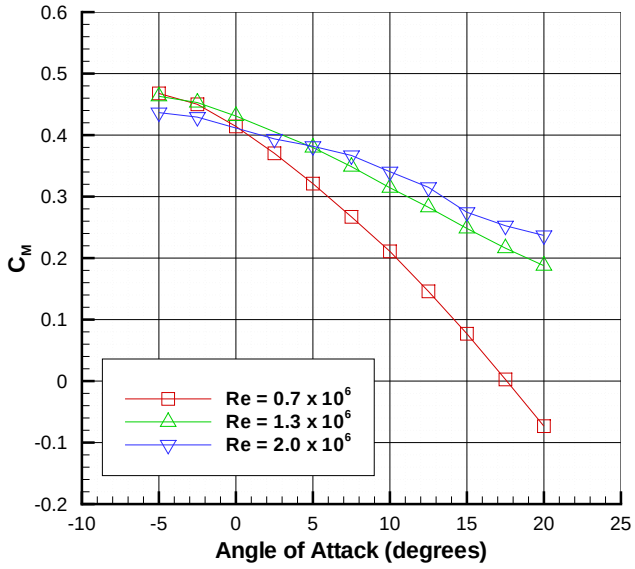

FIGURE 4.3: C_M variation with angle of attack.

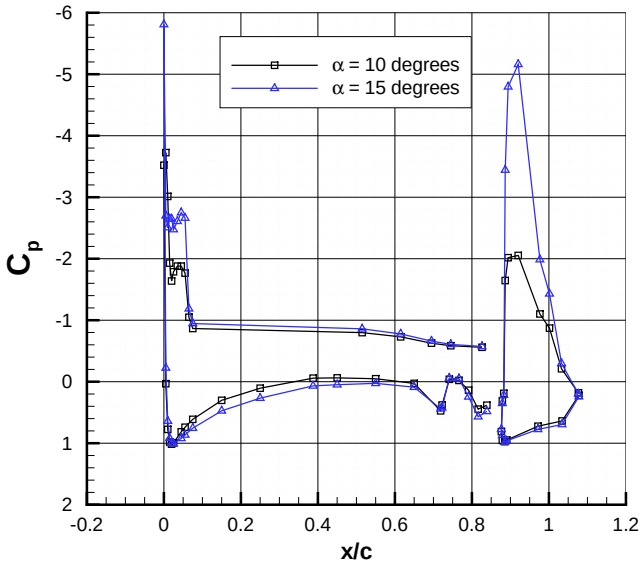

FIGURE 4.4: C_p distribution over the main element and flap at 20 m/s.

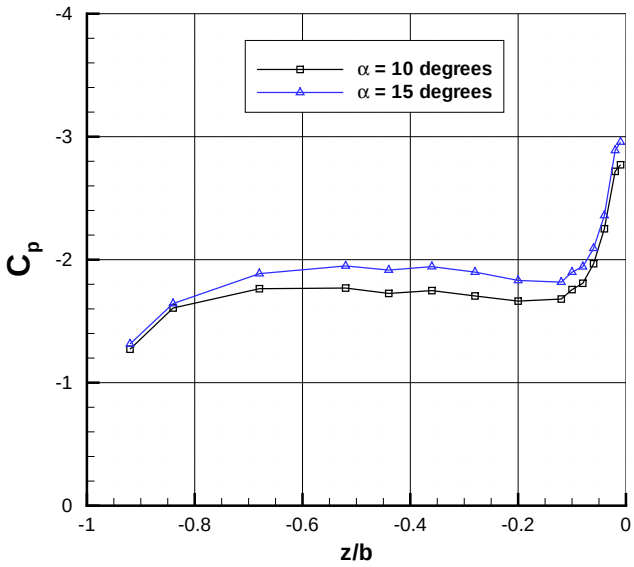

FIGURE 4.5: The spanwise C_p distribution over the flap at 20 m/s.

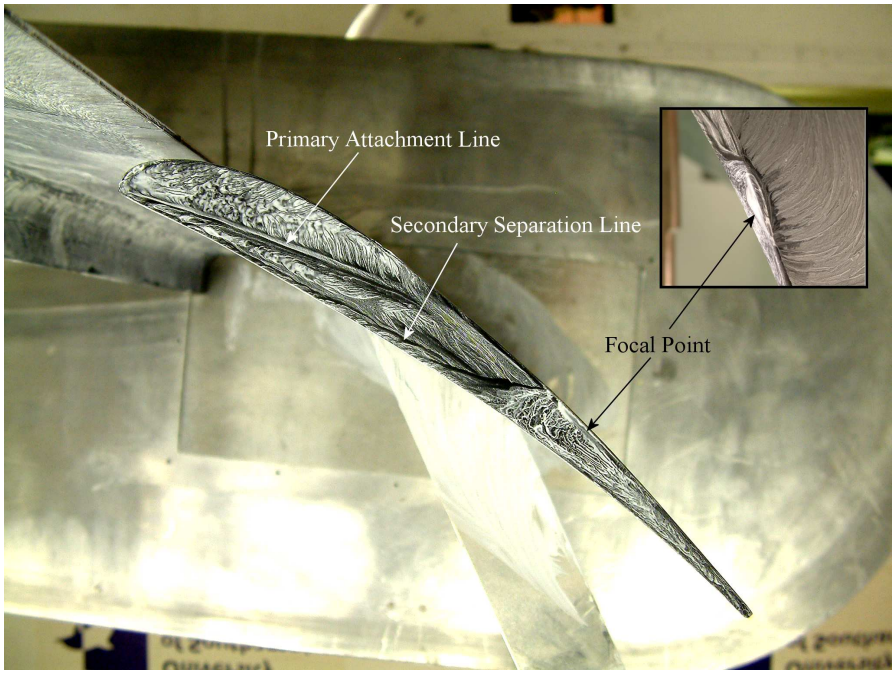

FIGURE 4.6: Oil flow of flap side edge showing major flow features. View looking starboard, flow is from left to right. $V_\infty = 20$ m/s.

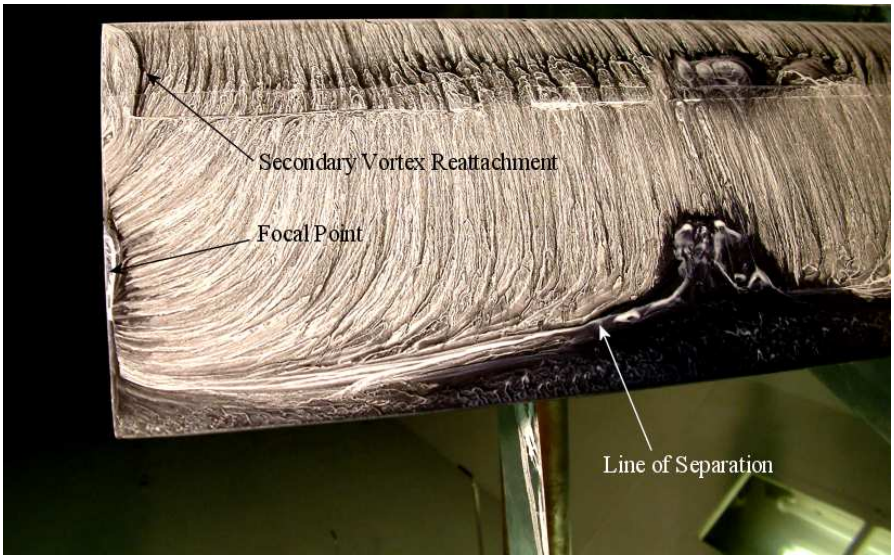

FIGURE 4.7: Oil flow of suction surface of flap. View looking upstream. $V_\infty = 20$ m/s.

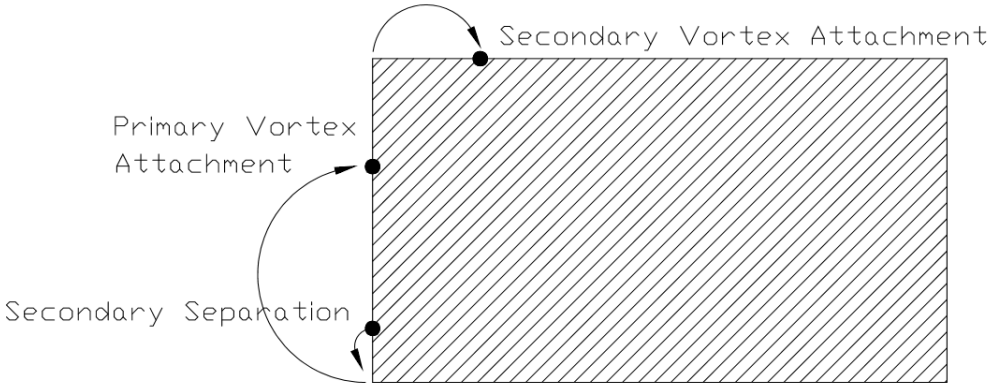

FIGURE 4.8: Schematic of flap side-edge flow in $y - z$ plane at $x_F/c_F = 0.27$. View looking upstream.

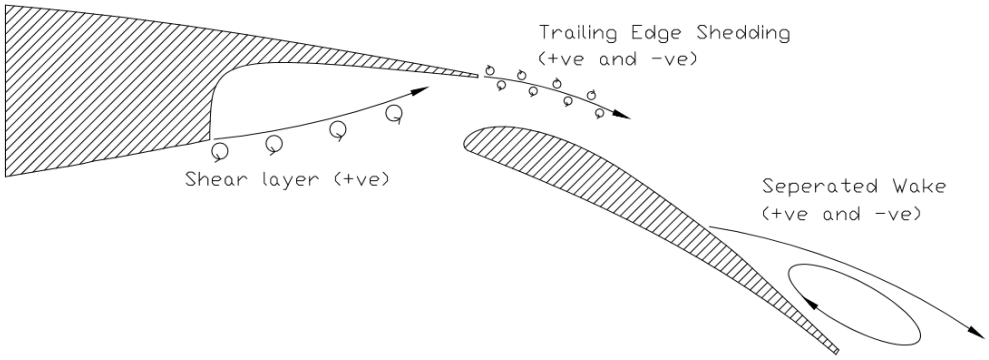

FIGURE 4.9: Schematic of vorticity sources in $x - y$ plane.

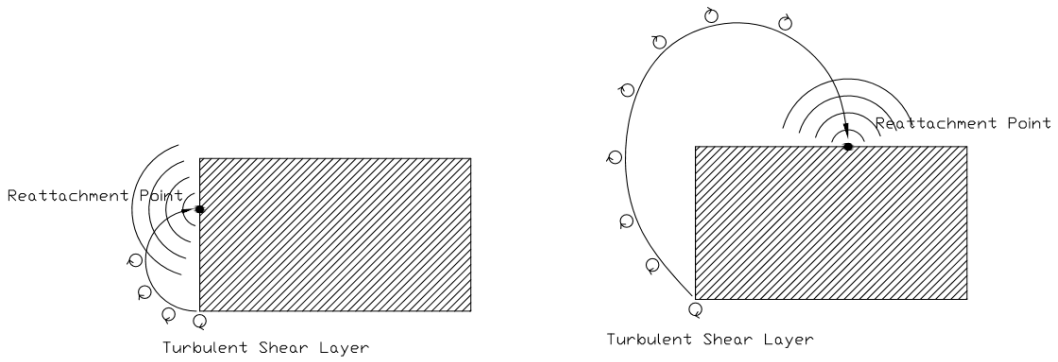

(a) $x_F/c_F = 0.2$

(b) $x_F/c_F = 0.4$

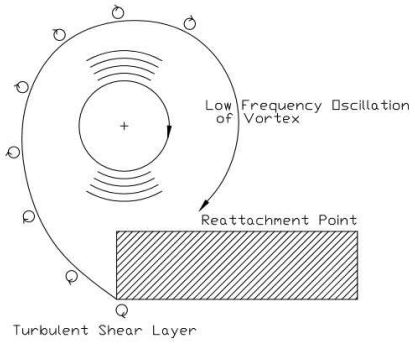

(c) $x_F/c_F = 0.8$

FIGURE 4.10: Potential acoustic sources due to vorticity-surface interactions.

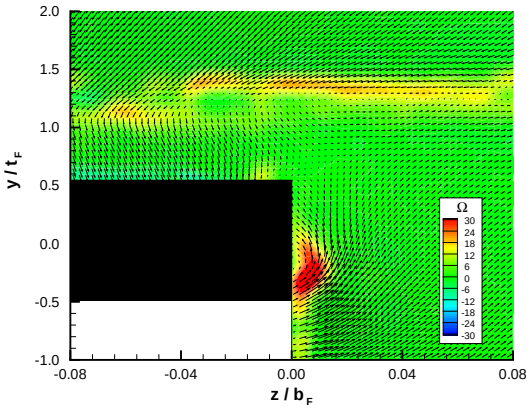

(a) $x_F/c_F = 0.2$

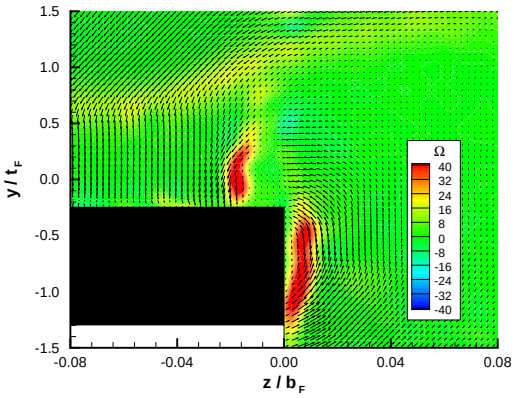

(b) $x_F/c_F = 0.4$

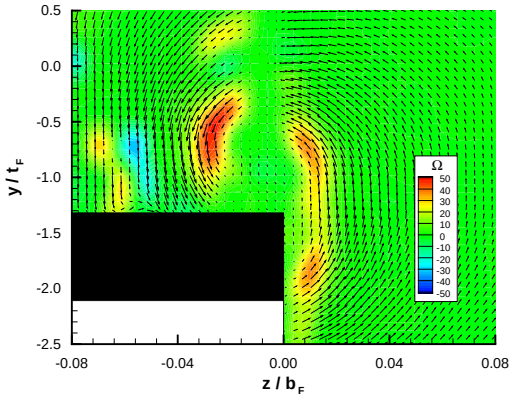

(c) $x_F/c_F = 0.6$

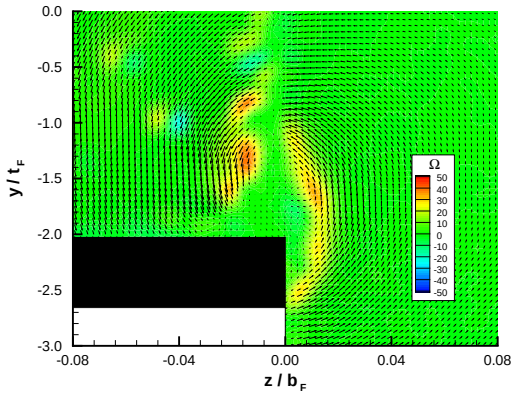

(d) $x_F/c_F = 0.7$

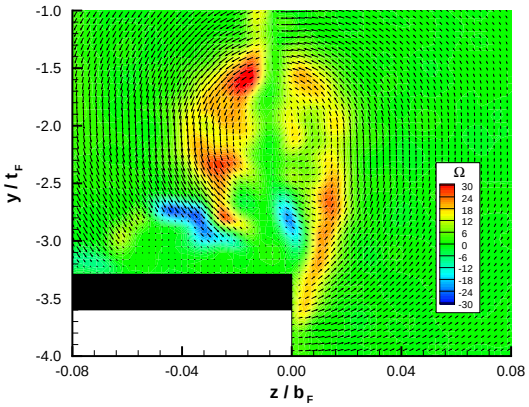

(e) $x_F/c_F = 0.9$

FIGURE 4.11: PIV data for the hardwall case. $V_\infty = 20$ m/s.

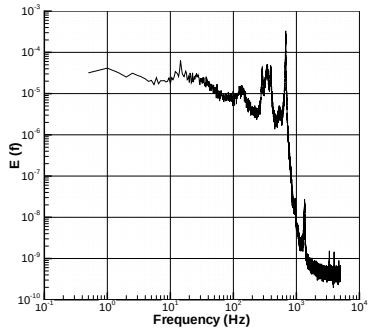

(a) $V_\infty = 10$ m/s, $\alpha = 5$ deg, $\delta_F = 29$ deg, Position 1.

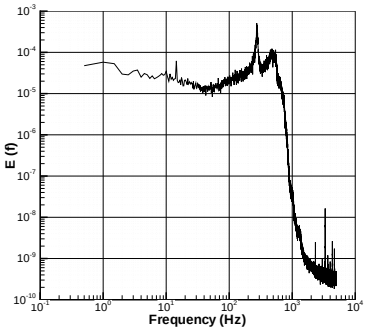

(b) $V_\infty = 10$ m/s, $\alpha = 10$ deg, $\delta_F = 29$ deg, Position 1.

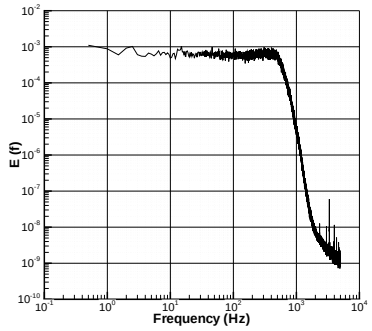

(c) $V_\infty = 20$ m/s, $\alpha = 10$ deg, $\delta_F = 29$ deg, Position 1.

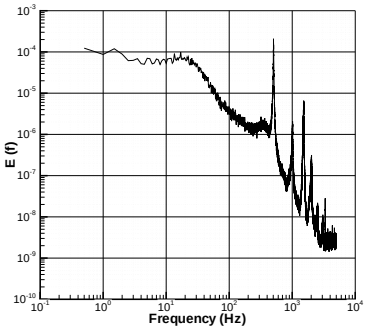

(d) $V_\infty = 10$ m/s, $\alpha = 10$ deg, $\delta_F = 29$ deg, Position 2.

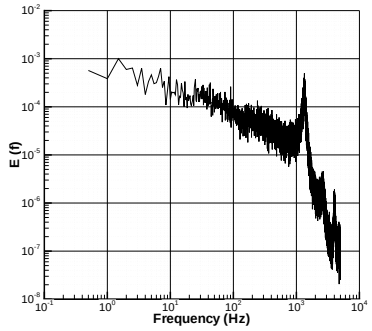

(e) $V_\infty = 20$ m/s, $\alpha = 10$ deg, $\delta_F = 29$ deg, Position 2.

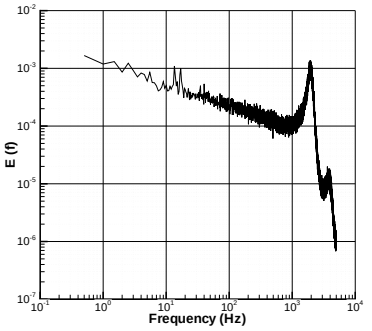

(f) $V_\infty = 30$ m/s, $\alpha = 10$ deg, $\delta_F = 29$ deg, Position 2.

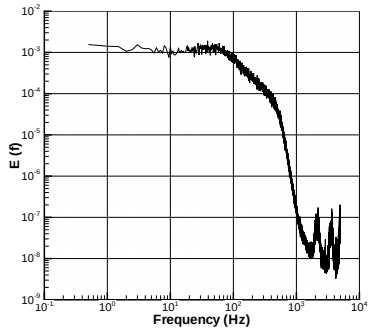

(g) $V_\infty = 10$ m/s, $\alpha = 5$ deg, $\delta_F = 39$ deg, Position 3.

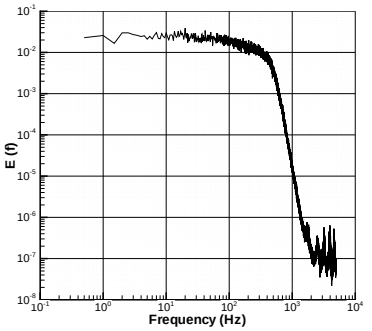

(h) $V_\infty = 20$ m/s, $\alpha = 5$ deg, $\delta_F = 39$ deg, Position 3.

FIGURE 4.12: Hotwire measurements in the downstream vortex.

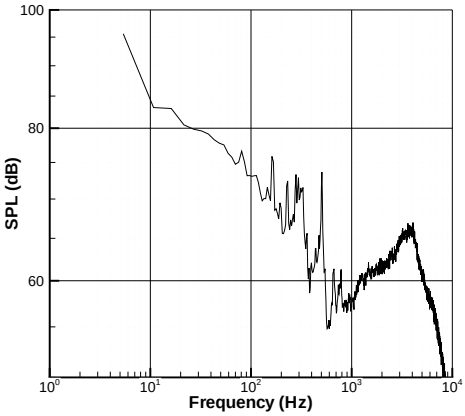

(a) $V_\infty = 10$ m/s, $\alpha = 5$ deg, $\delta_F = 29$ deg.

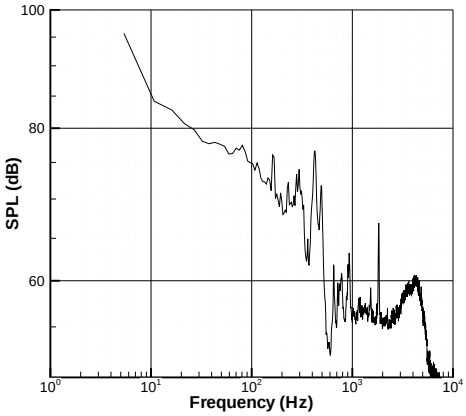

(b) $V_\infty = 10$ m/s, $\alpha = 5$ deg, $\delta_F = 39$ deg.

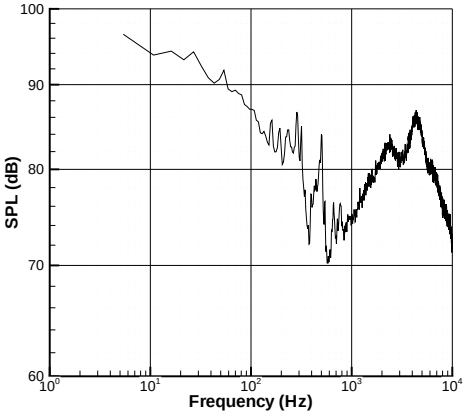

(c) $V_\infty = 20$ m/s, $\alpha = 5$ deg, $\delta_F = 29$ deg.

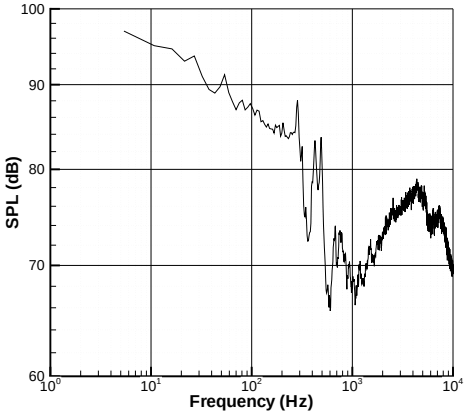

(d) $V_\infty = 20$ m/s, $\alpha = 5$ deg, $\delta_F = 39$ deg.

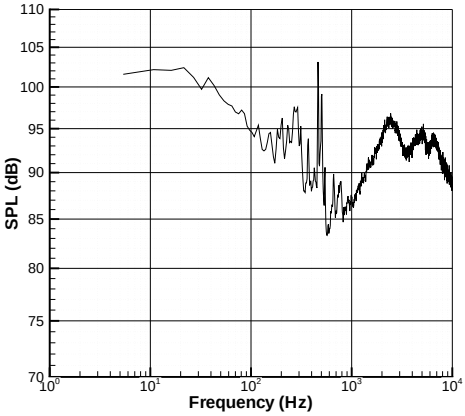

(e) $V_\infty = 30$ m/s, $\alpha = 5$ deg, $\delta_F = 29$ deg.

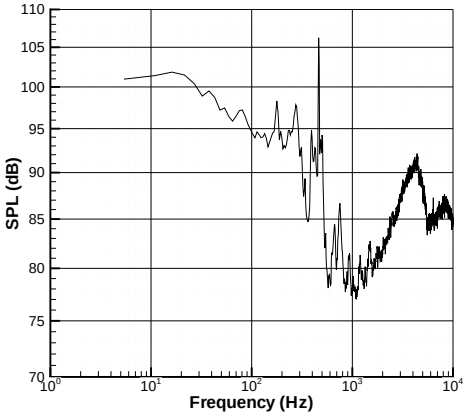

(f) $V_\infty = 30$ m/s, $\alpha = 5$ deg, $\delta_F = 39$ deg.

FIGURE 4.13: On-Surface microphone measurements for Mic 1 - hardwall case.

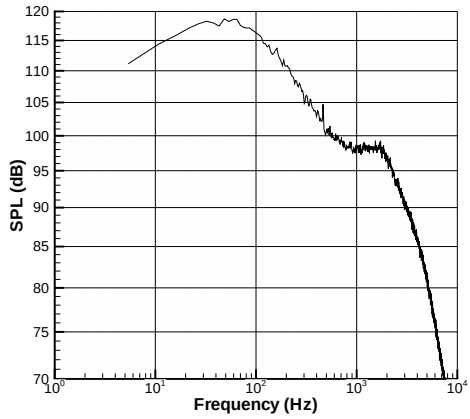

(a) $V_\infty = 30$ m/s, $\alpha = 5$ deg, $\delta_F = 29$ deg, Mic 2.

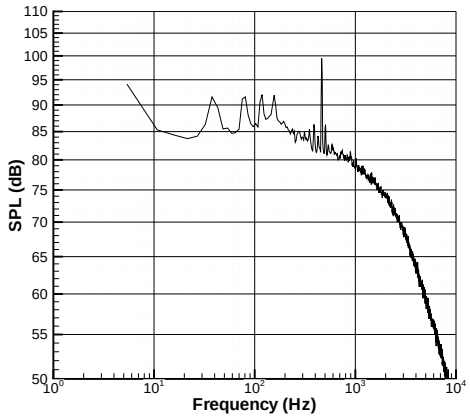

(b) $V_\infty = 30$ m/s, $\alpha = 5$ deg, $\delta_F = 29$ deg, Mic 3.

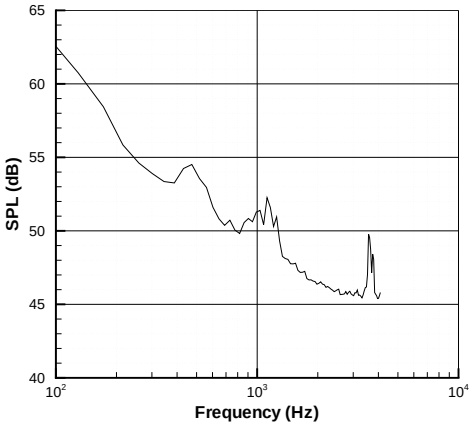

(c) $V_\infty = 10$ m/s, $\alpha = 5$ deg, $\delta_F = 29$ deg, Mic 4.

FIGURE 4.14: On-surface microphone measurements for Mic 2 , Mic 3 and Mic 4 - hardwall case.

Chapter 5

Experimental Results for Porous Side-Edge

This chapter presents the results for a series of experiments performed with a porous side-edge treatment applied to a flap side-edge. The effect of applying the porous side-edge treatment in general is discussed as well as the effect of different porosities on the nearfield flow around a flap side-edge. The structure of this chapter is similar to Chapter 4, which described the experiments with the hard flap side-edge.

5.1 Porous Side-Edge Treatment

Three different porous side-edges were investigated. These are tabulated in Table 5.1. The porous side-edges were made from Duocel aluminium foam made by ERG Materials and Aerospace Corporation. The aluminium alloy used was 6101. The foam was open-cell in nature. The permeability of the porous material was related to the number of pores per linear inch (PPI) and the relative density of the material to the solid base metal. In general, the typical pore dimension was related to the number of pores per linear inch for a given relative density. The aluminium foam had a reticulated structure of open duode-cahedronal-shaped cells connected by continuous, solid metal ligaments [79]. The matrix of cells and ligaments was completely repeatable, regular and uniform throughout the entire material. The width (measured in the z direction) of the porous side-edge attached to the flap side-edge was 0.02 m, which corresponded to 4% of the span of the flap. The thickness of the porous side-edge was the dimension in the y direction.

	Porosity (PPI)	Relative Density (%)
1	20	5 - 7
2	40	5 - 7
3	40	10 - 12

TABLE 5.1: Material properties of porous side-edge treatments.

5.2 Forces

Force measurements were taken with the three different porous treatments applied to the side-edge to determine the aerodynamic penalty associated with their use. This was an important measurement to be able to quantify. The aerodynamic loading on the flap was caused by the pressure differential between the pressure and suction surfaces. The porous material at the flap side-edge could not support a pressure differences without allowing a transpiration velocity through the material. It will be shown in the subsequent sections in this chapter that the porous side-edge was beneficial in reducing the mid frequency noise measured at the flap side-edge. However the use of porous materials to reduce noise was of little practical benefit if there was a large aerodynamic penalty associated with their use.

The lift, drag and pitching moment were measured at three different Reynolds numbers, 0.7×10^6, 1.3×10^6 and 2.0×10^6. Eleven angles of attack were measured ranging from -5 degrees to 20 degrees in steps of 2.5 degrees. Since the span of the flap was increased by 0.02 m with the porous side-edge, direct comparisons with the experimental results presented in Chapter 4 were not useful. To estimate the aerodynamic penalty associated with the use of porous flap side-edges, the surface of the porous material was covered in aluminium tape to determine the hardwall forces. This prevented any transpiration velocity through the porous flap side-edge.

The lift, drag and pitching moment measurements for the porous treatment of porosity 20 PPI and a relative density of 5-7% are shown in Figure 5.1. The application of the porous material resulted in a reduction of C_L of 0.008 ± 0.004 averaged over three runs. The reduction in the lift force was diminutive and was close to the repeatability of the experiments. The drag curve had a dependency on Reynolds number as discussed in Section 4.1 for the hardwall case. At a Reynolds number of 2.0×10^6, the C_D was 0.015 ± 0.004 greater than the hardwall values averaged over the angle of attack range. The aerodynamic force results for a porous treatment of 40 PPI 5-7% are shown in Figure 5.2. The C_L for this treatment was 0.008 ± 0.005 lower than the hardwall case. The C_D was 0.015 ± 0.003 greater than the hardwall values.

The final porous treatment was the least permeable with a porosity of 40 PPI and a relative density of 10-12%. The aerodynamic forces are shown in Figure 5.3. The lift

coefficient was 0.006 ± 0.004 less than the hardwall case. The drag coefficient (C_D) was 0.014 ± 0.006 greater than the hardwall case. This porous treatment had the least loss in lift at the side-edge due to its reduced permeability. The previous two treatments, both with a relative density of 5-7%, had similar losses in aerodynamic lift. At the flap side-edge, the loading was reduced due to the spanwise pressure distribution on the flap. Also since only a small portion (0.02 m) of the flap had the porous treatment applied, the effects were small. The slight increase in aerodynamic drag was due to the nature of the porous material. The flow through the porous material resulted in a pressure loss across the material, which produced a drag force. Compared to the accuracy of the measurements of the aerodynamic forces, the aerodynamic impact of the porous side-edge was small.

5.3 Influence of Porous Material on Flap Side-Edge Flowfield

The flowfield around the porous flap side-edge was measured in three $y-z$ planes that corresponded to the last three planes measured in the hardwall case. These planes are shown tabulated in Table 5.2. The same numbering was used as the hardwall results presented in Section 4.3.2. The PIV data obtained at planes 1 and 2 with the porous side-edges was of poor quality. The first two planes were through the dual vortex system that was present on the flap side-edge. Since the vortices were relatively weak at this point and were close to the surface, the PIV data was swamped by surface reflections from the porous material. The porous side-edges were painted black to reduce the reflections but due to the cellular structure of the material, the scattering of the laser light sheet was significant. Therefore, the quality of PIV data near the surface was not adequate.

PIV Plane	x_F/c_F
3	0.6
4	0.7
5	0.8

TABLE 5.2: PIV planes for porous side-edge experiments.

The velocity vectors and vorticity contours around the flap side-edge with a porous side-edge of porosity 20 PPI and a relative density of 5-7 % at $x_F/c_F = 0.6$ are shown in Figure 5.4(a). The effect of the porous side-edge was to reduce the magnitude of vorticity in the shear layer that was wrapped around the vortex. The maximum non-dimensional vorticity in the shear layer was 15.1 with a porous treatment of 40 PPI 5-7%. For the hardwall case, the maximum vorticity was 42.6. This shear layer originated at the separated boundary layer from the flap pressure surface. As discussed in

Chapter 4, it was this source of vorticity in the shear layer that fed the vortex increasing its strength and also causing it to become unsteady. The strength of the flap side-edge vortex was proportional to the discontinuity in loading that existed at the flap side-edge. The porous flap side-edge alleviated the pressure differential between the pressure and suction surfaces of the flap reducing large gradient changes in spanwise loading. This led to a weaker flap side-edge vortex.

The three porous treatments at $x_F/c_F = 0.7$ are shown in Figure 5.5. As the vortex increased in strength, the effect of different degrees of porosity became more apparent. The strongest vorticity in the shear layer was for the 40 PPI 5-7% case, shown in Figure 5.5(b). The lower the number of pores per linear inch for a given relative density, the higher the permeability of the material. Therefore, the transpiration velocity through the material was higher for a given pressure differential. The higher the relative density of the material, the more pressure differential it could support across the porous material.

As well as reducing the magnitude of vorticity in the shear layer wrapped around the vortex, the porous side-edge also had the effect of displacing the vortex further away from the surface. This can be seen in Figure 5.5 where the vortex was elongated in the vertical (y) direction. The displacement of the centre of the vortex core could not be measured directly. This was due to a lack of seeding particles in the vortex core. This was due to the centrifugal force in the vortex core, which pushed the seeding particles outside of the core. The displacement of the shear layer wrapped around the top of the vortex could be measured. At a plane of x_F/c_F of 0.7, the shear layer around the top of the vortex was $y/t_F = 3.05$ from the suction surface of the flap for the 40 PPI 10-12% treatment. The distance for the hardwall case at the same plane was $y/t_F = 2.05$. This corresponded to an increase in vertical displacement of the shear layer of approximately one maximum flap thickness. As the relative density of the porous material was reduced to 5-7%, the displacement distance from the suction surface increased to $y/t_F = 3.10$. Therefore, decreasing the relative density of the material increased the displacement effect. The lower the relative density, the less resistance the material offered, which led to higher transpiration velocities through the material. The spatial resolution of the PIV measurements was 0.0012 m or $\Delta y/t_F = 0.05$.

Shown in Figure 5.6 are three PIV planes at $x_F/c_F = 0.9$ with the three porous treatments applied. At this plane where the vortex was the largest and furthest away from the surface, the effect of porosity could be seen most clearly. The porous side-edge treatment with porosity of 20 PPI and density of 5-7% had the weakest shear layer wrapped around the vortex. The maximum vorticity magnitude was 9.6 in the shear layer with this treatment, compared to 14.9 with the 40 PPI 10-12% treatment. The 20 PPI 5-7% was the most permeable material tested and therefore could not support a significant pressure differential across the material between the pressure and suction surfaces of the

flap. This resulted in a vortex of lower strength and less vorticity in the weak shear layer that was wrapped around the vortex. At a plane of x_F/c_F of 0.9, the displaced shear layer had increased to $y/t_F = 3.2$ compared to the hardwall case of $y/t_F = 2.0$. This displacement effect was due to the finite mass flux through the porous material caused by the pressure differential between the suction and pressure surfaces of the flap.

Although it was not possible to capture velocity vectors within the porous material in PIV measurements, there were significant velocity components in the y and z directions within the porous side-edge. The computational results with the porous side-edge treatment discussed in Chapter 8 provided more detail of the flow through the porous side-edge than was possible with the PIV measurements. This was due to the difficulties in obtaining adequate PIV data near the surface. As the PIV plane moved aft along the flap chord, the point on the porous side-edge where the shear layer exited into the external flow moved towards the pressure surface. This was due to a reduction in the thickness of the porous side-edge as the trailing-edge was approached. As the leading-edge was approached, the porous side-edge was of significant thickness and contained a significant proportion of the shear layer.

The effect of the transpiration velocity in the y direction was most apparent at the $x_F/c_F = 0.9$ plane. There was a weak jet-like flow through the porous material in the vertical direction which is discussed in the computational results presented in Chapter 8. This had the effect of displacing the vortex and the shear layer that was wrapped around the vortex, away from the flap surface. The vortex was a significant source of unsteadiness, due to the nonlinear vortical interactions, discussed previously. Since it was located above a solid flap surface with sharp edges, it was a significant acoustic source. The displacement of this unsteadiness away from the solid surface had the advantage of reducing the acoustic source strength. Choudhari and Khorrami [59] stated that the amplification of the disturbances, which caused the instabilities, depended on the magnitude of the shear in the background mean velocity field. Therefore, they concluded that to lessen the magnitude of the unsteadiness projected onto the flap surface, the local vorticity field needed to be diffused or the source of hydrodynamic fluctuations needed to be displaced from the surface. The porous side-edge was shown in these PIV measurements to achieve both of these effects.

The width of porous material chosen was 0.02 m which corresponded to approximately 4% of the span of the flap. The decision of the extent of the porous treatment over the span of the flap was based on previous work [3, 59, 69] and on manufacturing considerations. By examining the PIV data and understanding the mechanism by which the porous side-edge modified the flowfield around the flap side-edge, better judgement can be made on the necessary width of the porous side-edge. The larger the spanwise extent of the porous side-edge, the less pressure differential can be supported between

the suction and pressure surfaces of the flap. This has the favourable result of a weaker vortex but reduces the aerodynamic loading on the flap.

Another favourable effect of a porous side-edge was the transpiration velocity through the porous side-edge. The porous side-edge needs to be of sufficient width to allow sufficient mass flux through the porous side-edge to displace the vortex core away from the surface. Near the trailing-edge the vortex core was at its largest. By examining the PIV image for the hardwall case at $x_F/c_F = 0.9$ (Figure 4.11(e)), the edge of the shear layer, at its most inboard location, was at $z/b_F = -0.042$. Therefore, to displace the vortex and the shear layer away from the surface due to the mass flux through the material, a porous material width of $z/b_F = 0.04$ seemed close to the optimum at this plane. In order to minimise the loss in aerodynamic performance due to the porous side-edge, a tapered design with variable width would be preferable. Since the maximum loading on the flap was near the leading-edge, where the width of the porous side-edge would be minimal, the loss in loading on the flap would be diminished.

5.4 Spectral Content of Off-Surface Vortex

This section details the hotwire anemometry measurements taken with the porous side-edge treatment. The hotwire measurements were used to obtain the spectral content of the flowfield containing the vortex downstream of the flap. The hotwire positions for the measurements with the porous treatment were the same for the hardwall case tabulated in Table 4.2.

The results for the three porous side-edges in the downstream wake outside of the vortex core are shown in Figure 5.7 for 10 m/s. All the spectra were broadband in nature. As the relative density of the material was increased and the characteristic pore dimension reduced, the spectra level increased across the frequency range measured. The reason for this additional energy in the wake with the change of porosity needed to be determined. A possible explanation was that the significant u component of velocity passing through the open cell porous material generated turbulence, which was then convected downstream in the wake. The mechanism was analogous to the turbulence generated by a mesh placed normal to the flow. A higher relative density of porous material meant that the characteristic pore dimension was smaller, and therefore the integral length scale of the generated turbulence was smaller. This was consistent with the higher levels and shift in frequencies at higher relative densities.

The spectra in the vortex core are shown in Figure 5.8 at a freestream velocity of 10 m/s. These spectra were significantly more noisy than their hardwall counterparts. A prominent feature in the spectra was a broadband hump centered around approxi-

mately 7 kHz ($St_F \approx 70$). At a porosity of 20 PPI, the height of this peak was reduced compared to the 40 PPI side-edge. As the relative density was increased from 5-7% to 10-12% for a porosity of 40 PPI, the level of this peak increased. For the hardwall case shown in Figure 4.12(g), there were a series of peaks from 2100 Hz ($St_F \approx 20$) to 4880 Hz ($St_F \approx 50$). The effect of applying the porous material was to merge these peaks together to form a broadband hump and to shift the dominant frequencies. A similar phenomenon was found by Khorrami and Choudhari [80] when they applied a porous treatment to the trailing-edge of a slat to reduce the trailing-edge noise. They found a reduction in the strength of Strouhal shedding from the finite thickness trailing-edge and also an upward shift in the Strouhal shedding frequency.

On the flap side-edge, the origin of these mid-frequency disturbances was turbulence in the shear layer being convected around the vortex and impinging on the flap side-edge. The further along the flap chord the boundary layer separated from the pressure surface, the larger the characteristic length scale of the turbulence due to the increased boundary layer thickness. The effect of the porous side-edge was to decrease the characteristic length scale of the energy bearing eddies responsible for this feature in the spectra. Khorrami and Choudhari [80] did not offer an explanation for the shift in frequency they determined in their calculations with a porous slat trailing-edge. A possible explanation may be that due to the interaction between the turbulent eddies in the shear layer and the reticulated structure of the porous side-edge, smaller energy bearing eddies were created. The analogy with flow over a turbulence generating mesh in a wind tunnel is again used. Large vortices that interact with a fine mesh are broken down to smaller vortices and there is a corresponding shift in dominant frequency.

The results for 20 m/s are shown in Figure 5.9. Again, a prominent feature in the spectra was the 7 kHz hump. The highest levels of this broadband hump corresponded to the porous side-edge with the smallest pore diameters, i.e. 40 PPI and a relative density of 10-12%. It should be noted that hotwire anemometry measures hydrodynamic instabilites, which may or may not propagate as acoustic waves. So although flow through the porous material, produced more turbulence in the wake downstream of the side-edge, this does not necessarily mean the farfield noise generated by the flap side-edge was greater. The on-surface microphone measurements, presented in the next section were more useful for determining nearfield acoustic perturbations.

5.5 Nearfield Pressure Fluctuations

This section presents and discusses results from measurements with on-surface microphones with a porous side-edge treatment applied. The first section discusses the results for a porous side-edge treatment of 20 PPI 5-7%. The changes in the spectra, compared

to the hardwall case, are noted. These changes are applicable to all the porous treatments applied. Changes in the 20 PPI 5-7% spectra with airspeed, angle of attack and flap deflection angle are discussed. Again these are generally applicable to all the porous treatments. Finally the relative differences, where they existed, between the remaining two porous treatments and the 20 PPI 5-7% spectra are discussed.

5.5.1 Porous Side-Edge Treatment of 20 PPI 5-7%

This section contains the results with a porous side-edge treatment with a porosity of 20 PPI and a relative density of 5-7%. Mic 3 was located on the port endplate facing the flap side-edge. A feature in the spectra of Mic 3 was a small broadband hump centered around 7000 Hz at 10 m/s, shown in Figure 5.10(a). This broadband feature was less pronounced at Mic 1 since the overall sound pressure levels were higher (Figure 5.11(a)). At 20 m/s, the feature was noticeable as a broadband hump centered around 12000 Hz as seen in Figure 5.11(c). The SPL of this feature was higher at the flap side-edge (Mic 1) than the port endplate facing the side-edge (Mic 3) (Figure 5.10(b)), which was 0.48 m from the porous side-edge.

The spectrum measured at Mic 1, at a freestream velocity of 10 m/s, an angle of attack of 5 degrees and a flap deflection angle of 29 degrees, is shown in Figure 5.11(a). The major feature in the hardwall measurements at these conditions was a large broadband hump centered around 4000 Hz with an amplitude of 69 dB (Figure 4.13(a)). The effect of applying the porous treatment to the flap side-edge was to remove this broadband hump almost completely. As mentioned previously in Section 4.5, the location of Mic 1 corresponded to the reattachment point of the primary shear layer on the flap side-edge. One of the proposed noise generation mechanisms in Chapter 4 was the turbulence in this shear layer interacting with the solid surface. Due to the finite impedance effect of the porous material, the convected turbulence impinging on the solid surface was greatly reduced. Instead of the large broadband hump centered around 4000 Hz, the spectrum with the porous side-edge at 10 m/s was more noisy and contained a small feature centered around 7000 Hz similar to the hotwire measurements in Section 5.4. The correlation between the two sources suggested that the porous side-edge was the source of the unsteadiness measured in the downstream vortex by hotwire anemometry.

At a freestream velocity of 30 m/s, a double tone like peak occurred at 470 Hz and 500 Hz as shown in Figure 5.11(e). A similar feature was measured for the hardwall case (Figure 4.13(e)), which only appeared at an airspeed of 30 m/s. The peak at 470 Hz, which appeared at 30 m/s, was the dominant feature measured by Mic 3 on the port endplate, shown in Figure 5.10(c). This suggested that this disturbance propagated efficiently. The magnitude of this double peak was significantly reduced for the porous treatment compared to the hardwall case. Similar to the other freestream velocities,

the most noticeable effect of applying the porous material, was a large reduction in the mid-frequencies measured at the flap side-edge.

The effect of increasing the angle of attack from 5 degrees to 10 degrees on both spectra measured on the flap side-edge surface and the endplate was negligible. This was true of the three airspeeds that were measured. An example at an airspeed of 30 m/s, an angle of attack of 10 degrees and a flap deflection angle of 29 degrees is shown in Figure 5.10(d). Therefore, the nearfield sound levels at the flap side-edge with the porous treatment were not sensitive to the angle of attack, similar to the hardwall case.

Although there was no sensitivity to the main element angle of attack over the range measured, the spectra were sensitive to the flap deflection angle. The spectrum at an airspeed of 10 m/s, an angle of attack of 5 degrees and a flap deflection angle of 39 degrees, is shown in Figure 5.11(b) with a porosity of 20 PPI and a relative density of 5-7%. The effect of increasing the flap deflection angle was to create a tone at 1450 Hz with an amplitude of 67 dB. For the hardwall case, the new tone that appeared at a flap deflection angle of 39 degrees was at a frequency of 1820 Hz and a magnitude of 70 dB, as seen in Figure 4.13(b). With the porous side-edge treatment there was also an additional tone at 4930 Hz with an amplitude of 48 dB. In the hardwall case this tone was not visible since it was below the mid frequency broadband hump. Again the application of the porous treatment resulted in lower sound pressure levels compared to the hard wall case across the frequency range measured.

At 20 m/s the effect of increasing the flap deflection angle to 39 degrees can be seen by comparing Figure 5.11(d) with Figure 5.11(c). The amplitude of the broadband hump at 12300 Hz increased by 4 dB to 45 dB with an increase in flap deflection angle. Compared to the hardwall case, these levels though were significantly lower due to the porous side-edge. The spectrum at 30 m/s for a flap deflection angle of 39 degrees is shown in Figure 5.11(f). The effect of increasing the flap deflection angle at this airspeed was to increase the amplitude of the low frequency tone at 470 Hz. It was still lower than the equivalent tone for the hardwall case. The broadband hump centered around 12800 Hz also increased in amplitude by approximately 4 dB. Increasing the flap deflection angle led to the formation of a stronger vortex at the flap side-edge. This increased the spanwise velocity component of the boundary layer past the flap side-edge in the z direction, which increased the magnitude of vorticity in the shear layer. As mentioned previously, Choudhari and Khorrami [59] noted that the amplification of disturbances depended directly on the magnitude of the shear, i.e. vorticity, in the background mean velocity field. Therefore, with the stronger vortex and shear layer, there was an increase in sound pressure levels at the flap side-edge for an increase in flap deflection angle.

The above discussion on the effect of applying a porous material to a flap side-edge

concerned a single porous material, i.e. a porosity of 20 PPI and a relative density of 5-7%. The effect of the other two porous materials relative to the 20 PPI 5-7% treatment are discussed in the next two sections.

5.5.2 Porous Side-Edge Treatment of 40 PPI 5-7%

At a porosity of 40 PPI and a relative density of 5-7%, the slight broadband hump around 7000 Hz at 10 m/s was no longer noticeable (Figure 5.12(a)). At 20 m/s, the broadband hump at 12300 Hz decreased by 6 dB compared to the 20 PPI 5-7% case (Figure 5.12(c)). The tonal peak at 470 Hz occurred again at 30 m/s as shown in Figure 5.12(e). The amplitude of this peak was higher than the 20 PPI 5-7% porous treatment. The broadband hump at 12300 Hz was significantly lower for 40 PPI 5-7% than for 20 PPI 5-7% case shown in Figure 5.11(e).

As the flap deflection angle was increased to 39 degrees for the 40 PPI 5-7% porous side-edge, further changes were seen in the spectra compared to the 20 PPI 5-7% porous treatment. As previously discussed, there was a new tonal feature that appeared when the flap deflection angle was increased to 39 degrees. At 10 m/s, this tone was at 1450 Hz (Figure 5.11(b)). With a porous treatment of 40 PPI 5-7%, the amplitude of this tone had decreased by 4 dB. There was also a peak at 4930 Hz, which had disappeared for the 40 PPI 5-7% case. As the airspeed was increased to 20 m/s, the broadband hump at 12300 Hz had decreased by 7 dB with the smaller diameter pores as shown in Figure 5.11(d). At a flap deflection angle of 39 degrees and an airspeed of 30 m/s, the tone at 470 Hz had increased compared to the 20 PPI 5-7% case (Figure 5.11(f)). A similar trend was seen for the lower flap deflection angle of 29 degrees. The broadband hump at 12800 Hz had decreased by 7 dB with the 40 PPI 5-7% treatment at 30 m/s as it had for an airspeed of 20 m/s .

5.5.3 Porous Side-Edge Treatment of 40 PPI 10-12%

The final porous treatment applied was a porosity of 40 PPI and a relative density of 10-12%. This was the least permeable of all the materials applied. Although all three of the porous treatments performed significantly better than the hardwall case, there were differences between each of the treatments. At an airspeed of 10 m/s, an angle of attack of 5 degrees and a flap deflection angle of 29 degrees there was a broadband hump centered from 3000 Hz to 6000 Hz at an amplitude of 36 dB as shown in Figure 5.13(a). This only occurred with this porous treatment. This broadband peak corresponded with the mid frequency peak measured in the hardwall case shown in Figure 4.13(a), which was caused by turbulence in the shear layer impinging on the flap side-edge. The amplitude of this broadband feature with this porous treatment was lower than the hardwall case due to the impedance of the porous material.

As the airspeed was increased to 20 m/s (Figure 5.13(c)), the amplitude of the broadband hump at 12300 Hz was 45 dB, which was higher than the other two porous treatments. At 30 m/s (Figure5.13(e)), the amplitude of the tone at 470 Hz was 93 dB, which was similar to the level with the 20 PPI 5-7% treatment. The porous treatment of 40 PPI 5-7% produced the worst tone at 30 m/s at this frequency. However, all three porous treatments greatly reduced this tone from its amplitude of 103 dB for the hardwall case. The broadband hump centered around 12800 Hz had an amplitude of 56 dB. This again was the highest of all the porous treatments.

Figure 5.13(b) shows the spectrum for 10 m/s and a flap deflection angle of 39 degrees. The peak at 5000 Hz for the 20 PPI 5-7% case (Figure 5.11(b)) had disappeared with this porous treatment. Also the additional peak at 1450 Hz, which was due to the increase in flap deflection angle, had a lower level than the other two porous treatments. The spectrum at 20 m/s with a flap deflection angle of 39 degrees is shown in Figure 5.13(d). The amplitude of the broadband feature at 12300 Hz was between the two other porous treatments. The treatment of 40 PPI 5-7% produced the lowest amplitude of this feature. Similarly at 30 m/s the amplitude of the peak at 12800 Hz lay between the amplitude at the other two porous treatments, as shown in Figure 5.13(f).

The change in sound pressure level for all three porous materials is shown in Figure 5.14 for a main element angle of attack of 5 degrees and a flap deflection angle of 29 degrees. These spectra were averaged over one-third octave bands and subtracted from the hardwall spectrum at the same condition. The peak reduction with the porous material was centered around 10 kHz. The major reductions in the nearfield sound pressure levels were from 2 kHz to 12.5 kHz. The porous flap side-edge treatment of 40 PPI 5-7% produced the most reduction in sound pressure levels. However, at frequencies less than 200 Hz the magnitude of the reduction was less compared to the other two treatments. The least permeable of the treatments (40 PPI 10-12%) resulted in the smallest peak reduction. At frequencies less than 1 kHz the reduction is similar to the treatment with 20 PPI 5-7%.

5.6 Chapter Summary

A series of experiments were performed with three porous flap side-edges to determine their effect on the aerodynamics and aeroacoustics of a flap side-edge flowfield. The aerodynamic penalty associated with the use of a porous flap side-edge was an increase in drag of 0.014 with the 20 PPI 5-7% treatment. This value was averaged over three runs and varied ± 0.004 across the angle of attack range measured. There was a slight decrease in the lift coefficient of approximately 0.008 ± 0.005 due to the reduction in

loading on the porous side-edge. The magnitude of the loss in aerodynamic lift was comparable to the accuracy of the measurements.

The PIV measurements showed that a porous side-edge of 20 PPI 5-7% produced the weakest shear layer around the side-edge vortex. The positive effects of the porous side-edge on the nearfield flow was to reduce the strength of the vortex and the shear layer that fed vortex. Another favourable effect was the displacement of the vortex away from the surface. The hotwire anemometry measurements showed that the spectrum levels were higher in the wake possibly due to increased turbulence production in the porous material. An effect of the adding the porous material was a broadband hump centered around 7000 Hz.

The on-surface microphones showed that the amplitude of this additional 7000 Hz hump was significantly lower in the flap side-edge nearfield than the hardwall spectra measured at the same flow conditions. The major effect of adding the porous-edge on the nearfield acoustics was a significant reduction in the levels of the mid frequencies. This was not only due to a weaker vortex but also the finite impedance effect of the porous material as the turbulent shear layer impinged on it. The porous side-edge of 40 PPI 10-12% had the least aerodynamic penalty associated with it, but performed the worst in reducing the mid frequency noise. A porous treatment of 20 PPI 5-7% resulted in the weakest shear layer and lowest sound pressure levels.

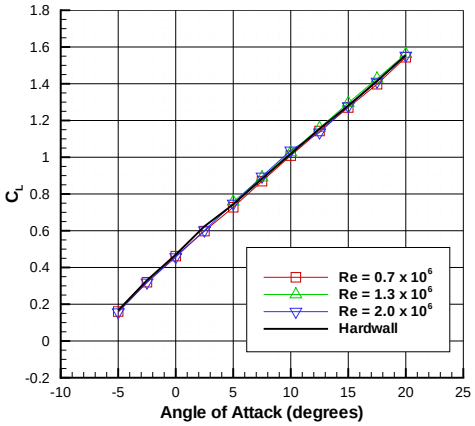

(a) C_L versus α.

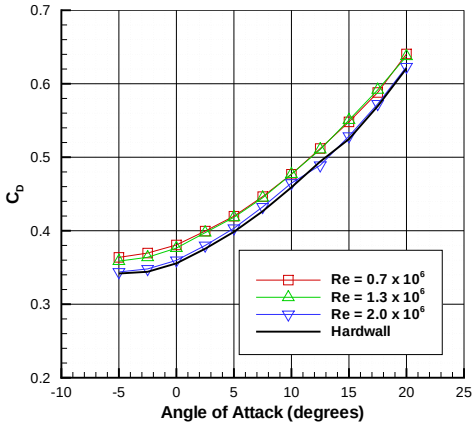

(b) C_D versus α.

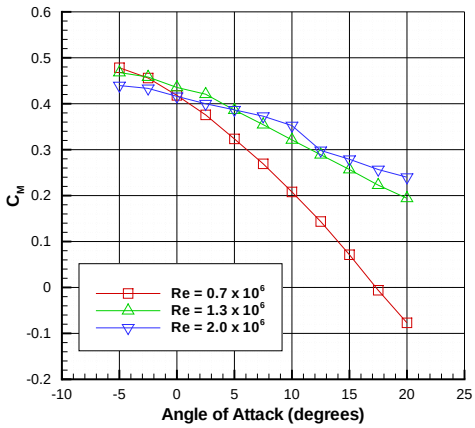

(c) C_M versus α.

FIGURE 5.1: Aerodynamic forces and moments with 20 PPI 5-7% porous treatment.

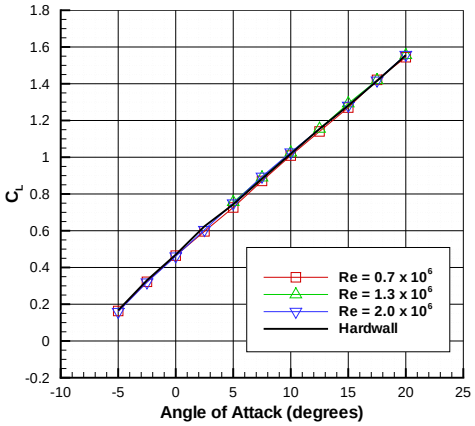

(a) C_L versus α.

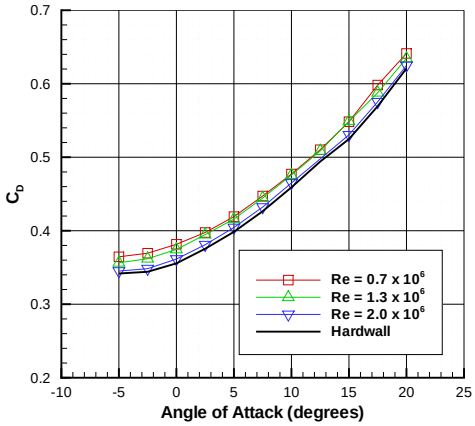

(b) C_D versus α.

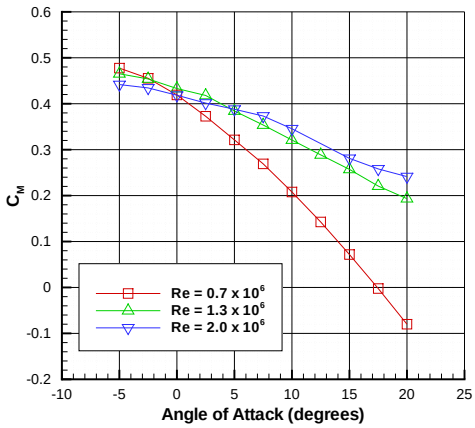

(c) C_M versus α.

FIGURE 5.2: Aerodynamic forces and moments with 40 PPI 5-7% porous treatment.

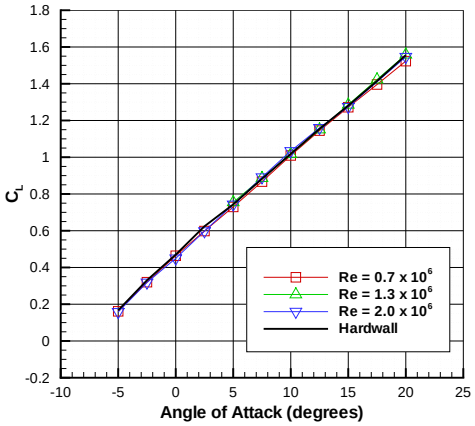

(a) C_L versus α.

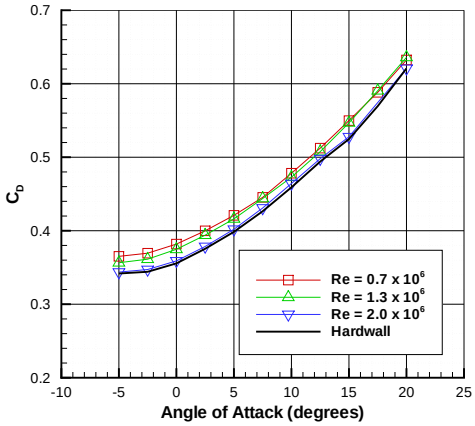

(b) C_D versus α.

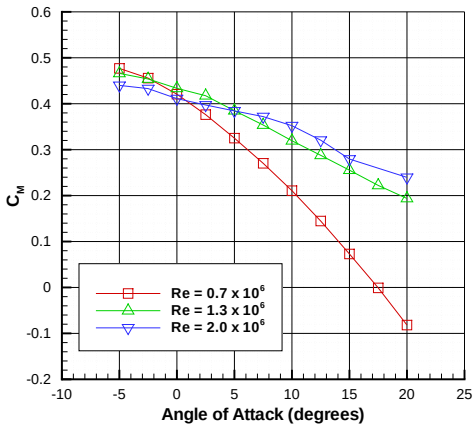

(c) C_M versus α.

FIGURE 5.3: Aerodynamic forces and moments with 40 PPI 10-12% porous treatment.

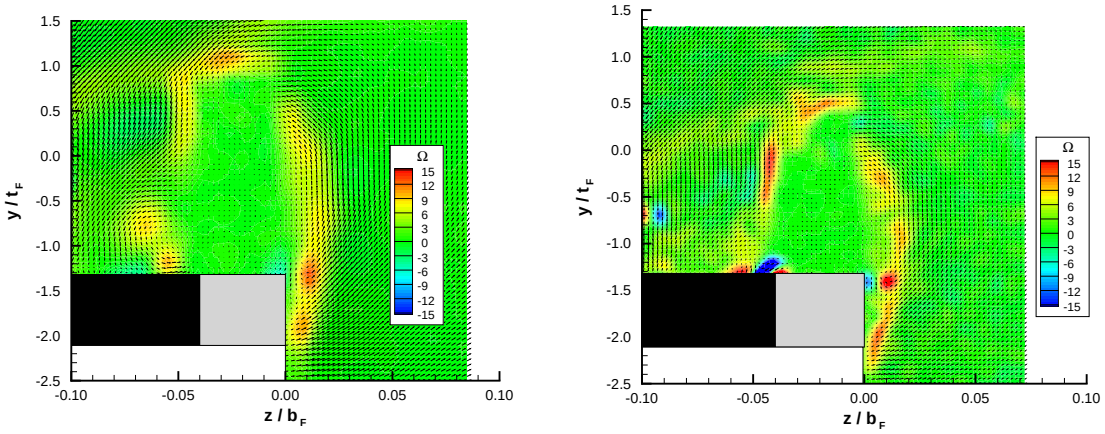

(a) 20 PPI 5-7%.

(b) 40 PPI 5-7%.

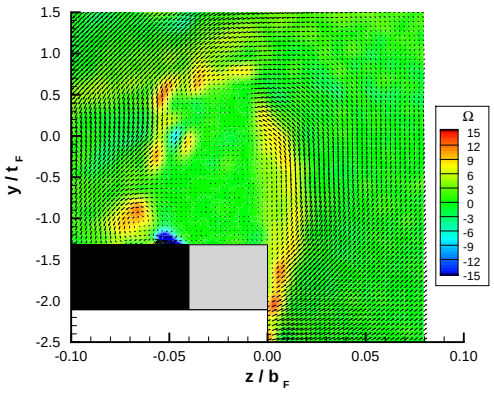

(c) 40 PPI 10-12%

FIGURE 5.4: PIV planes at $x_F/c_F = 0.6$ with porous side-edge treatments. $V_\infty = 20$ m/s.

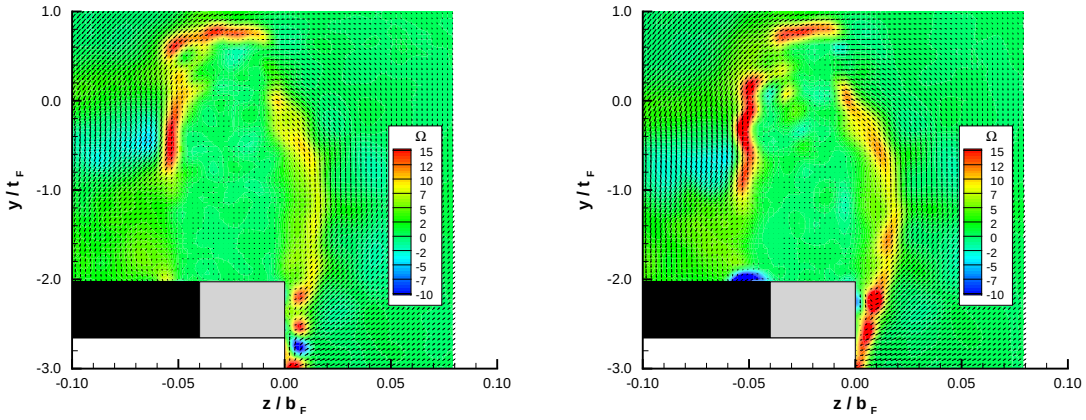

(a) 20 PPI 5-7%.

(b) 40 PPI 5-7%.

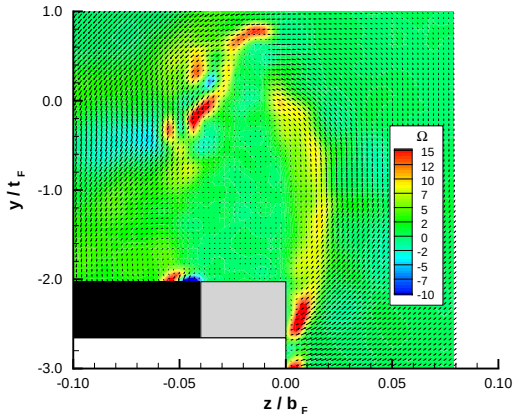

(c) 40 PPI 10-12%

FIGURE 5.5: PIV planes at $x_F/c_F = 0.7$ with porous side-edge treatments. $V_\infty = 20$ m/s.

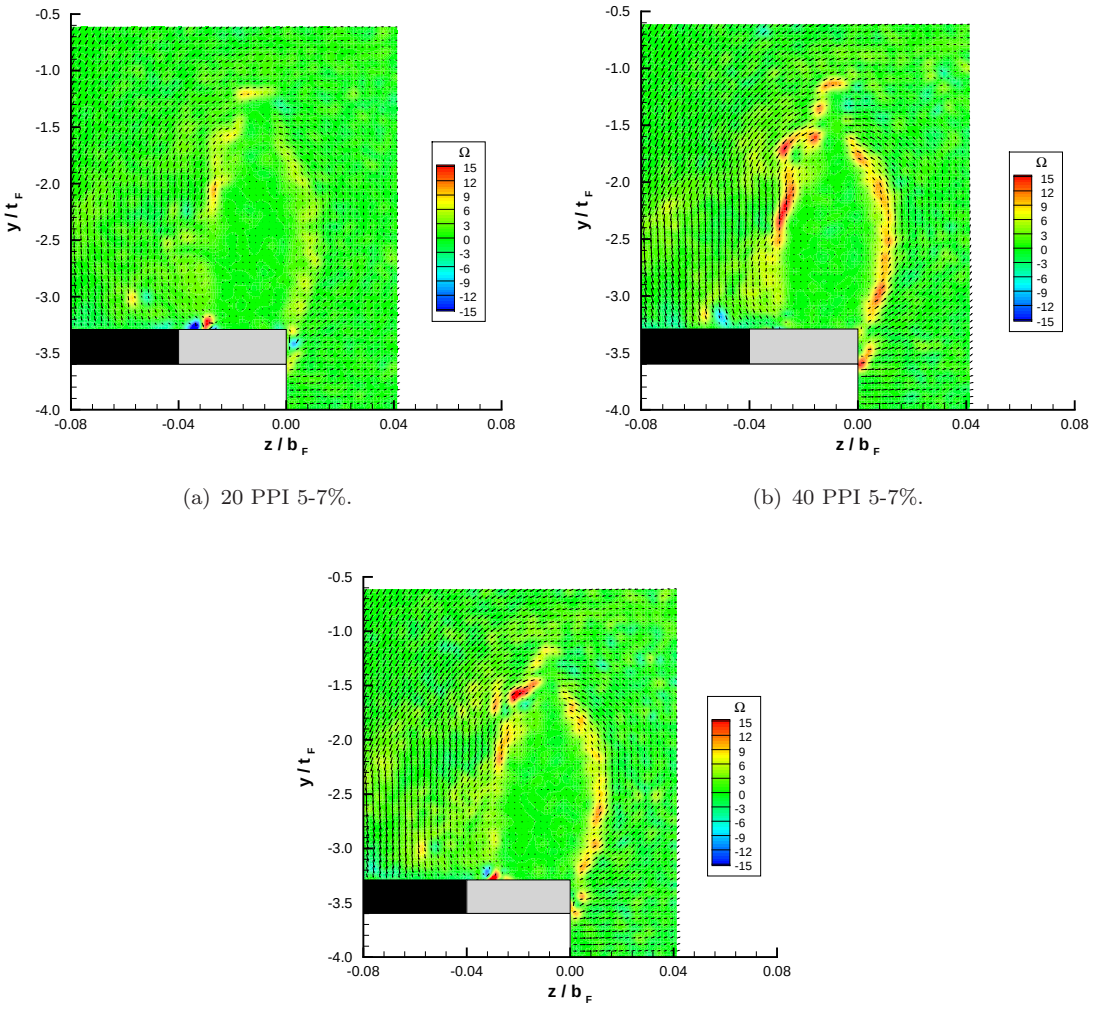

(a) 20 PPI 5-7%.

(b) 40 PPI 5-7%.

(c) 40 PPI 10-12%

FIGURE 5.6: PIV planes at $x_F/c_F = 0.9$ with porous side-edge treatments. $V_\infty = 20$ m/s.

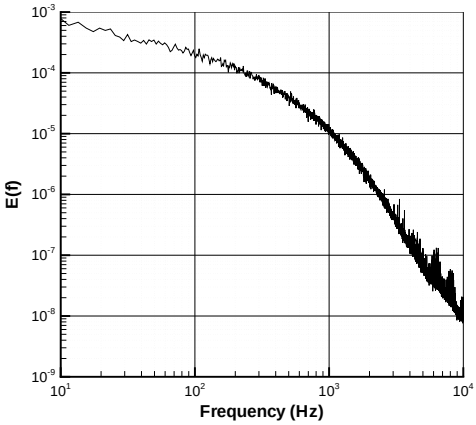

(a) $V_\infty = 10$ m/s, $\alpha = 5$ deg., $\delta_F = 29$ deg. 20 PPI 5-7%.

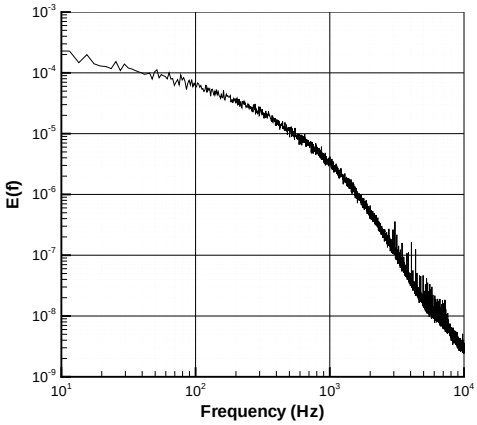

(b) $V_\infty = 10$ m/s, $\alpha = 5$ deg., $\delta_F = 29$ deg. 40 PPI 5-7%.

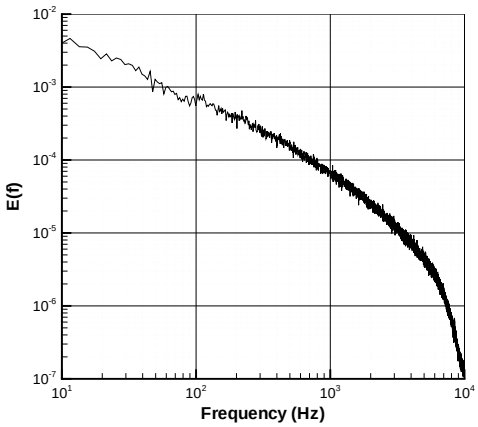

(c) $V_\infty = 10$ m/s, $\alpha = 5$ deg., $\delta_F = 29$ deg. 40 PPI 10-12%.

FIGURE 5.7: Hotwire data outside of vortex core.

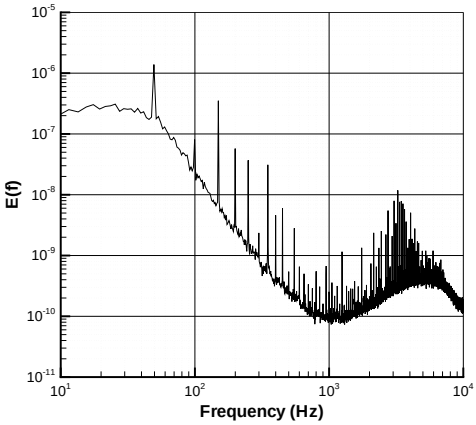

(a) $V_\infty = 10$ m/s, $\alpha = 5$ deg., $\delta_F = 29$ deg. 20 PPI 5-7%.

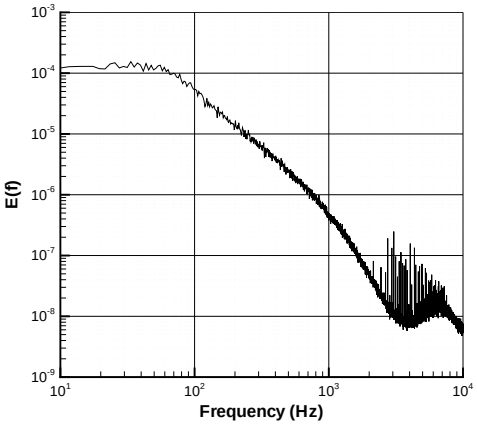

(b) $V_\infty = 10$ m/s, $\alpha = 5$ deg., $\delta_F = 29$ deg. 40 PPI 5-7%.

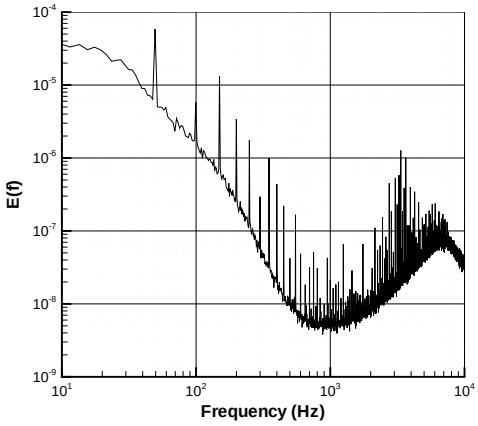

(c) $V_\infty = 10$ m/s, $\alpha = 5$ deg., $\delta_F = 29$ deg. 40 PPI 10-12%.

FIGURE 5.8: Hotwire data in vortex core at 10 m/s.

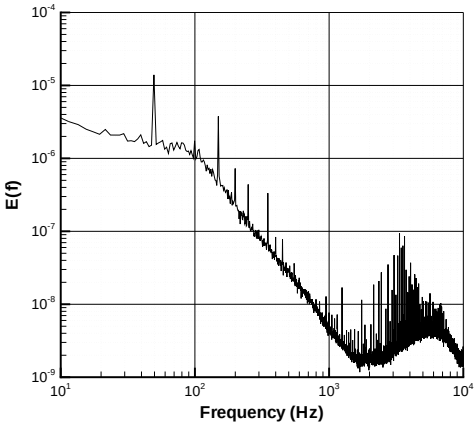

(a) $V_\infty = 20$ m/s, $\alpha = 5$ deg., $\delta_F = 29$ deg. 20 PPI 5-7%.

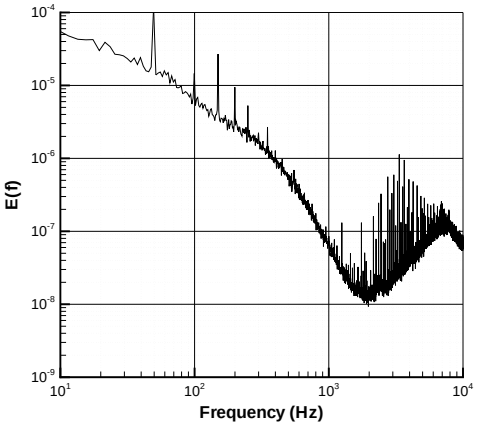

(b) $V_\infty = 20$ m/s, $\alpha = 5$ deg., $\delta_F = 29$ deg. 40 PPI 10-12%.

FIGURE 5.9: Hotwire data in vortex core at 20 m/s.

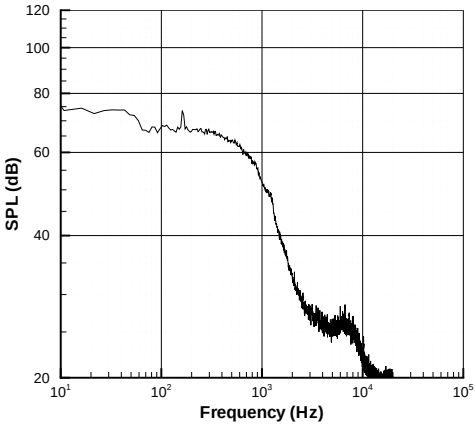

(a) $V_\infty = 10$ m/s, $\alpha = 5$ deg., $\delta_F = 29$ deg.

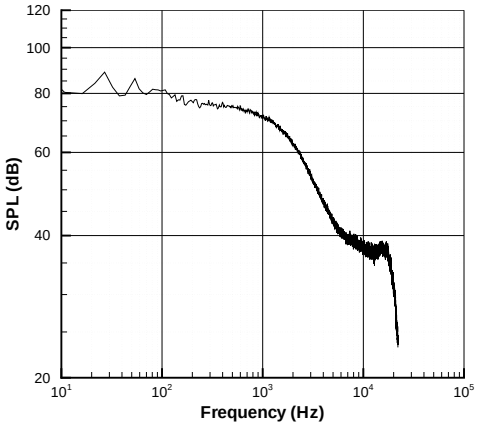

(b) $V_\infty = 20$ m/s, $\alpha = 5$ deg., $\delta_F = 29$ deg.

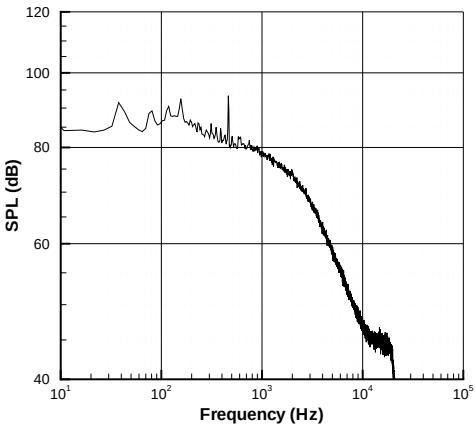

(c) $V_\infty = 30$ m/s, $\alpha = 5$ deg., $\delta_F = 29$ deg.

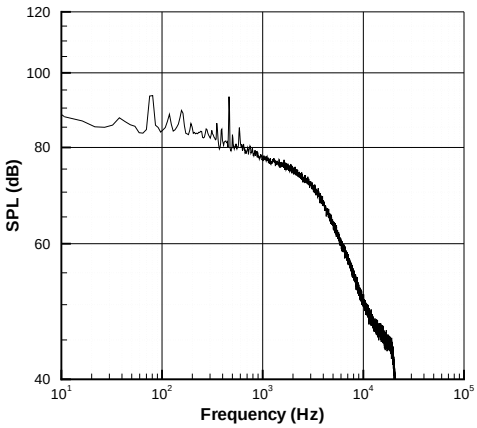

(d) $V_\infty = 30$ m/s, $\alpha = 10$ deg., $\delta_F = 29$ deg.

FIGURE 5.10: Microphone measurements for Mic 3. 20 PPI 5-7%.

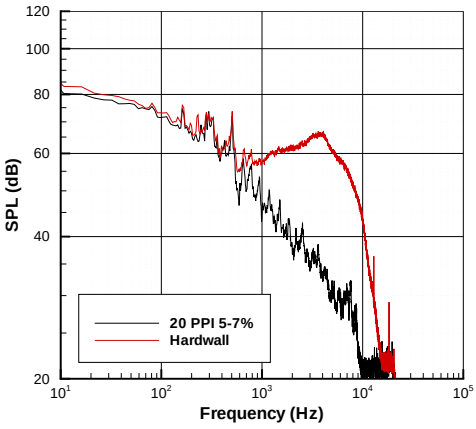

(a) $V_\infty = 10$ m/s, $\alpha = 5$ deg., $\delta_F = 29$ deg.

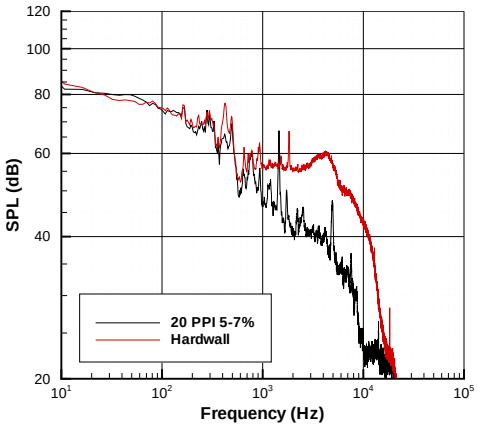

(b) $V_\infty = 10$ m/s, $\alpha = 5$ deg., $\delta_F = 39$ deg.

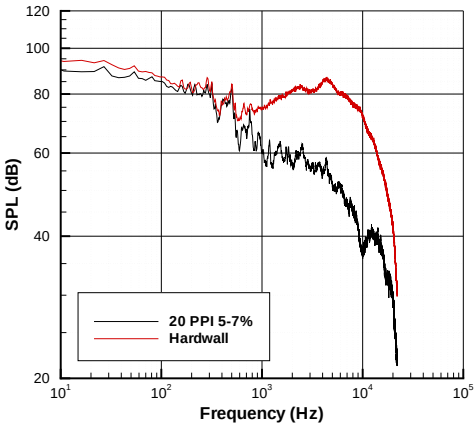

(c) $V_\infty = 20$ m/s, $\alpha = 5$ deg., $\delta_F = 29$ deg.

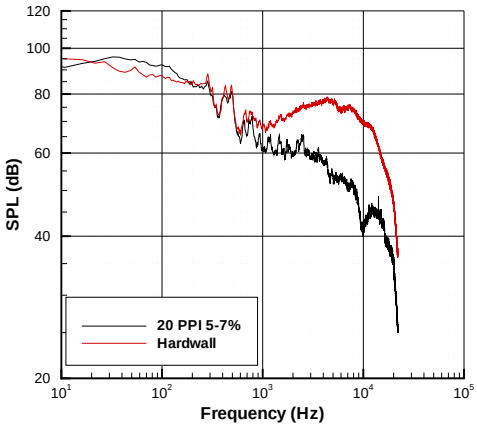

(d) $V_\infty = 20$ m/s, $\alpha = 5$ deg., $\delta_F = 39$ deg.

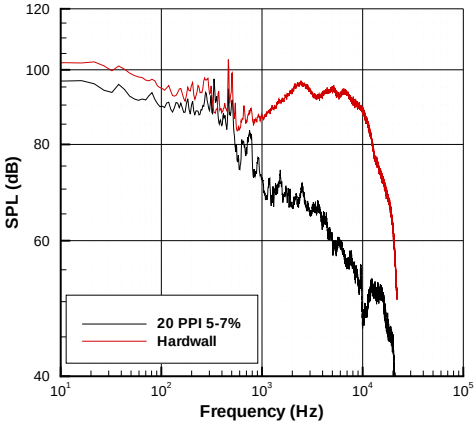

(e) $V_\infty = 30$ m/s, $\alpha = 5$ deg., $\delta_F = 29$ deg.

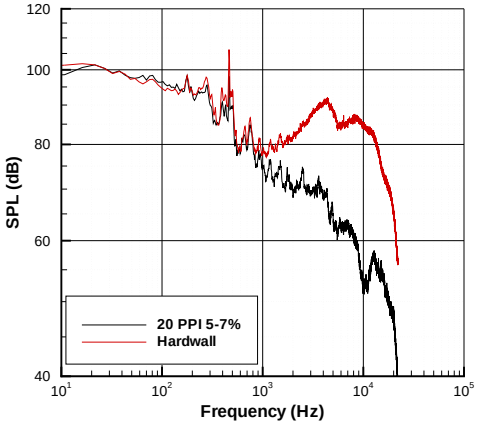

(f) $V_\infty = 30$ m/s, $\alpha = 5$ deg., $\delta_F = 39$ deg.

FIGURE 5.11: Microphone measurements for Mic 1. 20 PPI 5-7%.

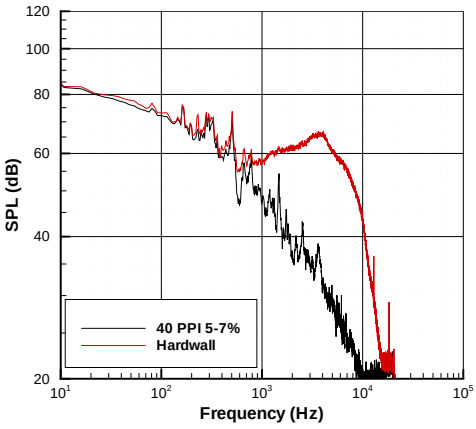

(a) $V_\infty = 10$ m/s, $\alpha = 5$ deg., $\delta_F = 29$ deg.

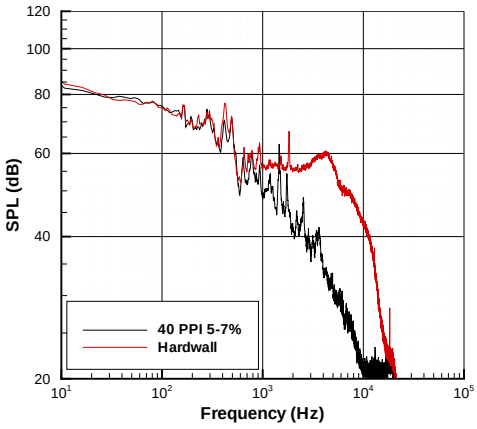

(b) $V_\infty = 10$ m/s, $\alpha = 5$ deg., $\delta_F = 39$ deg.

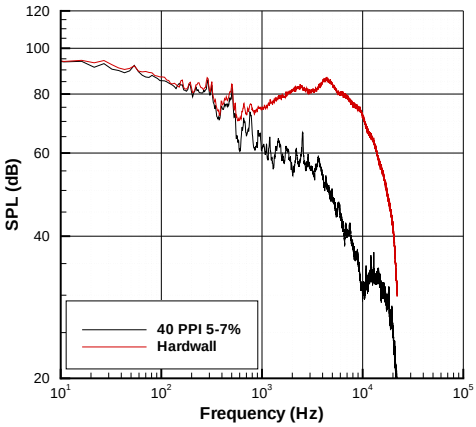

(c) $V_\infty = 20$ m/s, $\alpha = 5$ deg., $\delta_F = 29$ deg.

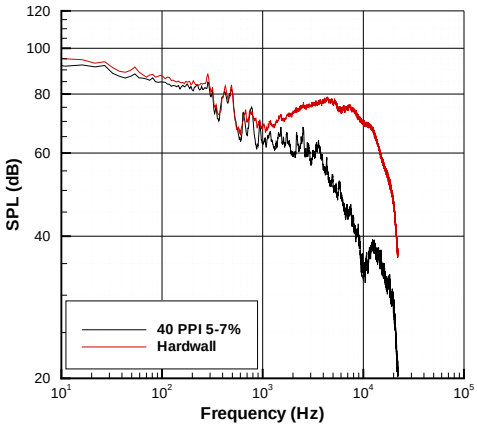

(d) $V_\infty = 20$ m/s, $\alpha = 5$ deg., $\delta_F = 39$ deg.

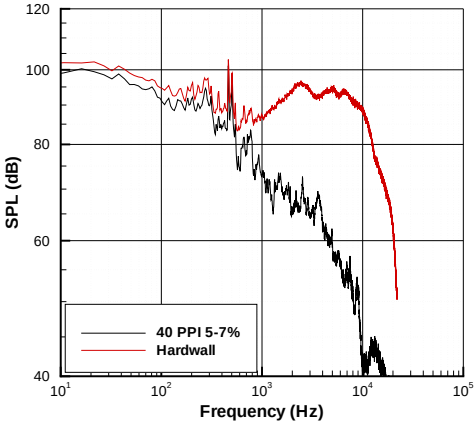

(e) $V_\infty = 30$ m/s, $\alpha = 5$ deg., $\delta_F = 29$ deg.

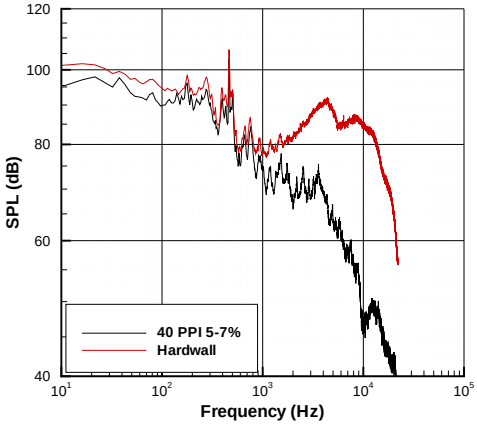

(f) $V_\infty = 30$ m/s, $\alpha = 5$ deg., $\delta_F = 39$ deg.

FIGURE 5.12: Microphone measurements for Mic 1. 40 PPI 5-7%.

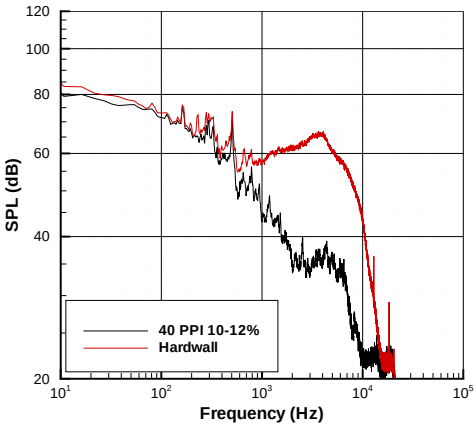

(a) $V_\infty = 10$ m/s, $\alpha = 5$ deg., $\delta_F = 29$ deg.

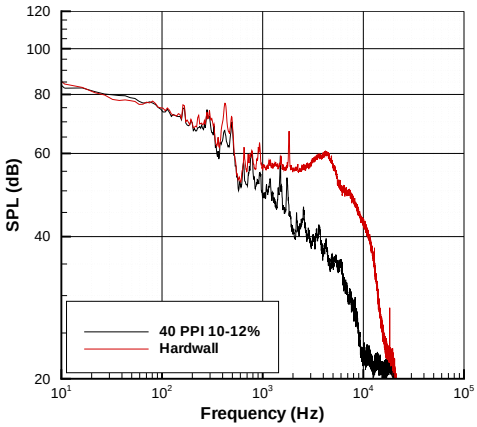

(b) $V_\infty = 10$ m/s, $\alpha = 5$ deg., $\delta_F = 39$ deg.

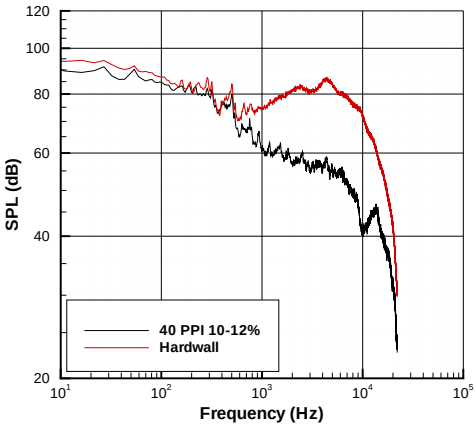

(c) $V_\infty = 20$ m/s, $\alpha = 5$ deg., $\delta_F = 29$ deg.

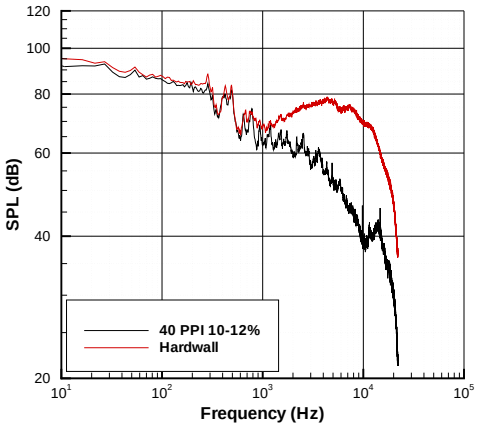

(d) $V_\infty = 20$ m/s, $\alpha = 5$ deg., $\delta_F = 39$ deg.

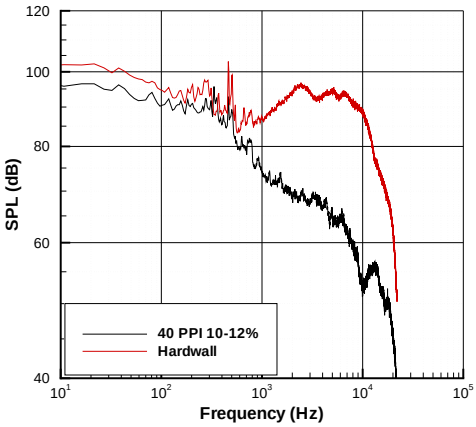

(e) $V_\infty = 30$ m/s, $\alpha = 5$ deg., $\delta_F = 29$ deg.

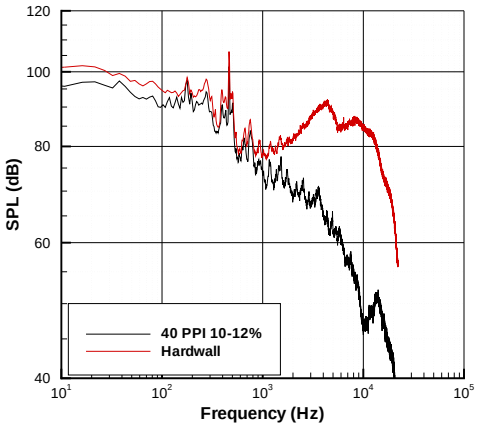

(f) $V_\infty = 30$ m/s, $\alpha = 5$ deg., $\delta_F = 39$ deg.

FIGURE 5.13: Microphone measurements for Mic 1. 40 PPI 10-12%.

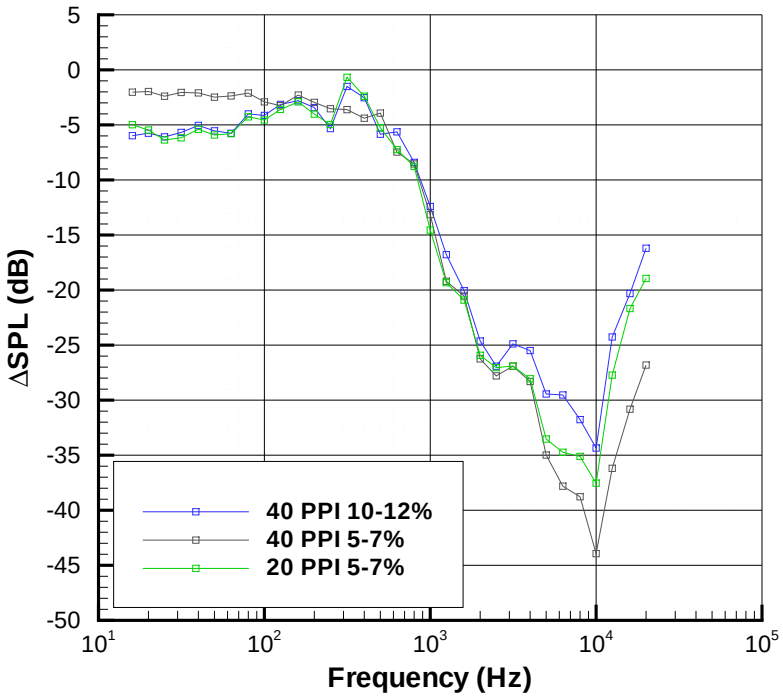

FIGURE 5.14: Change in sound pressure level with different porous materials relative to hardwall case.

Chapter 6

Experimental Results for Split Flap Configuration

This chapter investigates the aerodynamics and aeroacoustics of a split flap configuration. The split flap configuration consisted of a deflected semi-span flap and a second flap that was retracted, shown in Figures 6.1 and 6.2. This retracted flap formed an extended main element trailing-edge. This configuration added a further degree of complexity and was more realistic compared to the idealised flowfield presented in Chapters 4 and 5, where the formation of the flap side-edge vortex was unimpeded by the presence of an extended main element trailing-edge.

6.1 Split Flap Configuration

The gap between the main element trailing-edge and the flap was referred to as the side-lap region by Choudhari *et al.* [51]. According to Choudhari *et al.*, the side-lap region caused a high speed jet to flow through the gap region. This caused a strong shear layer that separated from the main element with an opposite sign of vorticity to that of the flap side-edge vortex. The cross flow through the gap had an effect of flattening the upper-surface flap vortex and delayed the merging between the two vortices.

Hardin [61] presented an idealised two-dimensional theory of the flap side-edge noise mechanism. The magnitude of the sound depended on the strength of boundary layer vorticity swept around the side-edge and the distance of the vortex from the edge. The spanwise mean flow around the flap side-edge was modelled by potential flow theory. This mechanism, without the additional noise arising from flow through the side-lap region, was similar to the experimental set-up presented previously in Chapters 4 and 5. Howe [64] claimed that Hardin's model took no account of the important effects arising from the proximity of the wing ahead of the flap and in particular the adjacent

trailing-edge of the wing, i.e. a split flap configuration. Howe formulated a model for the flow through a gap between the side-edge of the flap and the undeflected portion of the neighbouring wing trailing-edge. In Howe's model the length of the gap (L) was equal to the chord of the flap. The width ($2s$) was taken to be equal to the mean distance between the flap side-edge and the adjacent undeflected portion of the wing. It was found that the sound produced by turbulent fluctuations in the spanwise flow near the side-edge was dependent on the size of the gap. A schematic of Howe's model is shown in Figure 6.3.

Howe derived high and low frequency asymptotic formulae which expressed the acoustic frequency spectrum in terms of the wavenumber-frequency spectrum of surface pressure fluctuations on the suction surface of the part span flap just inboard of the side-edge. The radiation efficiency of the flap side-edge noise depended on the mean gap Strouhal number based on the magnitude of the spanwise flow (w) and the gap dimension ($2s$). At high frequencies the radiation had monopole characteristics and was associated with the unsteady flux through the slot induced by turbulence present at the flap side-edge. At low frequencies, when the gap could be considered acoustically compact, the flux was equivalent to a dipole source at the flap side-edge. Howe states the importance of taking into account the undeflected portion of the neighbouring trailing-edge in estimating the radiated sound pressure level.

6.2 Split Flap Flowfield

6.2.1 Surface Flow Visualisation

The split flap configuration altered the aerodynamics and aeroacoustics of the flap side-edge flowfield. The flowfield was characterised by a high speed flow through the gap between the trailing-edge of the main element and the deflected portion of the flap. This caused a strong shear layer, of opposite sign vorticity to that of the side-edge vortex, which separated from the main element trailing-edge. It also caused a flattening of the secondary vortex on the suction surface of the flap. This is shown schematically in Figure 6.4.

Oil flow was performed to visualise the on-surface flow of the split flap configuration. The surface features of the flap side-edge can be seen in Figure 6.5. The gap between the extended trailing-edge of the main element and the flap suction surface is also shown. The main vortex separated from the lower edge of the flap and reattached along the primary attachment line. Because of the sharp edge, the separation line was fixed at the bottom edge. The effect of the extended trailing-edge of the main element was to impede the formation of the vortex near the flap leading-edge. It also affected the growth of the

primary vortex on the flap side-edge compared to the configuration without the split flap.

The flow features on the suction surface of the flap are shown in Figure 6.6. The shear layer that originated from the pressure surface of the flap flowed through the gap under the influence of the induced velocity field by the side-edge vortex. This flow reattached on the suction surface of the flap on the secondary vortex reattachment line. The effect of the flow through the gap was to flatten the secondary vortex in the split flap configuration and to move it further inboard. Away from the flap side-edge, the flow separated before the trailing-edge of the flap. The influence of the low pressure vortex core was to delay the separation as the side-edge was approached. The secondary reattachment line and the trailing-edge coalesce to a single line where the vortex core separated from the surface.

6.2.2 Influence of Split Flap on Flap Side-Edge Flowfield

A series of PIV measurements were taken in $y-z$ planes to characterise the flow around the split flap configuration. The first plane was at $x_F/c_F = 0.2$. A contour plot of x vorticity is shown in Figure 6.7. Every fourth vector is shown. The presence of a flap side-edge vortex induced a large spanwise flow in the negative z direction. A shear layer of positive vorticity separated from the pressure surface of the flap. This shear layer was convected through the gap between the flap and the extended trailing-edge main element. As shown in the oil flow visualisation it impinged on the suction surface of the flap.

A shear layer of negative x-vorticity originated at the trailing-edge of the main element due to the boundary layer, which separated from the surface. The shear layer that contained negative vorticity was deflected downwards from the main element trailing-edge towards the suction surface of the flap due to the velocity field induced by the vortex. The shear layer that contained negative x vorticity that existed at $y = 0.38$ in Figure 6.7 was caused by the flow to the port of the trailing-edge of the main element being in the shadow of the laser sheet. Therefore, no vectors were measured there. This resulted in vorticity being generated at the fringe of the laser sheet which was not physical. The physical shear layer that originated from the negative vorticity generated in the boundary layer of the spanwise flow along the main element trailing-edge was the shear layer that was deflected towards the suction surface.

The flow around the split flap configuration was characterised by a spanwise flow through the gap between the flap and the main element trailing-edge. A contour plot of velocity magnitude (V_{mag}) is shown in Figure 6.8. The velocity magnitude in the $y-z$ plane was defined as $\sqrt{v^2+w^2}$. Velocity distribution curves through the gap are shown in Figure 6.9 at five different spanwise locations. The velocities through the gap have been non-dimensionalised with respect to the freestream velocity of 20 m/s. The maxi-

mum non-dimensionalised w velocity through the gap was -0.81. The spanwise velocity initially increased through the gap until $z/b_F = -0.01$. After this point as the distance from the gap increased, the magnitude of the spanwise velocity decreased. The magnitude of the spanwise velocity decreased as the secondary reattachment line was approached.

The vorticity field at the same $y - z$ plane is shown in Figure 6.10 as the flap deflection angle was increased to 39 degrees. The strength of the vortex increased as the flap deflection angle increased. The size of the gap between the main element trailing-edge and the flap also increased at the higher flap deflection angle. This allowed the vortex to form relatively unimpeded by the presence of the main element trailing-edge compared to the lower flap deflection angle configuration. The stronger vortex, due to the increased gap, induced a larger spanwise component of velocity through the gap. A contour plot of velocity magnitude is shown in Figure 6.11.

Velocity distribution curves through the gap at the flap side-edge are plotted in Figure 6.12 for this flap deflection angle at various spanwise stations. Similar to the previous flap deflection angle, the magnitude of the spanwise velocity increased initially as the distance along the flap increased. The maximum non-dimensional spanwise velocity was -1.17 at $z/b_F = -0.01$. This was over 40% greater than the flap deflection angle of 29 degrees configuration. As the distance from the flap side-edge increased further, the magnitude of the spanwise velocity component decreased as the influence of the vortex became weaker. The influence of the vortex caused a small area of positive spanwise velocity (w), and therefore negative vorticity, to be generated on the flap suction surface where the shear layer reattached on the surface and flowed towards the side-edge. This can be seen in Figure 6.12 at $z/b_F = -0.028$ and $z/b_F = -0.033$. Further inboard from the secondary reattachment line, the flow is away from the flap side-edge.

The effect of increasing the flap deflection angle was to increase the strength of the side-edge vortex. The gap between the main element trailing-edge and the flap suction surface also increased. This led to higher induced spanwise velocities through the gap. The negative vorticity, which was contained in the boundary layer on the main element trailing-edge, separated and was deflected towards the flap suction surface due to the velocity field induced by the vortex. Similarly, the positive vorticity in the shear layer associated with the flap side-edge vortex was convected through the gap and impinged on the flap suction surface.

A second plane, which corresponded to $x_F/c_F = 0.1$, was measured. This was the point where the gap was a minimum at a flap deflection angle of 29 degrees. The vorticity field is shown in Figure 6.13 and velocity magnitude contours are shown in Figure 6.14. A small primary vortex on the flap side-edge is shown. The shear layer that orig-

inated at the pressure surface of the left, reattached on the flap side-edge. The flow through the gap was almost negligible due to the small gap dimension and no vectors were measured. The secondary vortex on the suction surface near the leading-edge did not exist. Since the flow was constrained through the gap, the shear layer curved significantly and reattached on the flap side-edge.

For a flap deflection angle of 39 degrees, a small amount of flow went through the gap. The vorticity contours and velocity magnitude contours are shown in Figures 6.15 and 6.16 respectively. The shear layer was curved less severely, which resulted in less vorticity for the larger flap deflection angle. This was due to the small gap size. Once the size of the gap was significant enough to allow some flow through it for both flap deflection angles, the higher flap deflection angle always resulted in a stronger vortex and higher levels of vorticity. The small amount of flow through the gap at this flap deflection angle is shown in Figure 6.17. The maximum spanwise velocity measured was $w/V_\infty = -0.3$.

The last plane was at $x_F/c_F = 0.8$, towards the trailing-edge of the flap. The gap between the main element and the flap was no longer present at this plane. At a flap deflection angle of 29 degrees, the vortex was located just off-surface. The x vorticity and velocity contours are shown in Figures 6.18 and 6.19 respectively. An area of negative vorticity is seen on the suction surface of the flap where the flow reattaches on the surface of the flap and flows towards the flap side-edge. This created a boundary layer with negative x vorticity between the secondary reattachment line and side-edge. As the flap deflection angle increased to 39 degrees, the vortex increased in size as shown in Figures 6.20 and 6.21. The high levels of vorticity in the vortex core were not measured in this condition since the vortex was of sufficient strength that very few seeding particles were in the vortex core due to inertial effects. There was also a thin vertical band where no data was measured. This was due to reflection and diffraction of the laser sheet off the solid flap side-edge.

6.3 Acoustics Source Maps

6.3.1 Hardwall

A series of phased microphone array measurements were taken to determine the acoustic source location on the split flap configuration. The variables changed were flap deflection angle, main element angle of attack, and freestream velocity. The array was facing the suction surface of the flap and main element. The flowfield results had shown that a high speed flow existed through the gap between the extended main element trailing-edge and the flap suction surface. There was also a shear layer that originated from the

main element trailing-edge that was convected towards the suction surface of the flap. The purpose of these phased microphone measurements were to determine whether an acoustic source could be identified in this gap region.

The scan plane for the split flap configuration at a flap deflection angle of 29 degrees and a main element angle of attack of 5 degrees is shown in Figure 3.10. Eleven different airspeeds were measured for each configuration. The results for a freestream velocity of 20 m/s, a main element angle of attack of 5 degrees and a flap deflection angle of 29 degrees are presented in Figure 6.22. The resolution of the array is too poor below 2 kHz for the data to be of any use. A beamforming plot at 2 kHz is shown in Figure 6.22(a). The plot shows there was a strong noise source associated with the vortical structure off the surface of the flap as it separated before the trailing-edge. The resolution of the array at this frequency was 145 mm. By comparison the chord of the flap was 198 mm and therefore the mid frequency noise associated with the unsteadiness inherent in the vortex was not well spatially resolved. At 4 kHz there was a source on the suction surface on the flap side-edge but it was only barely perceptible above the broadband background noise of the wind tunnel.

At a frequency of 8 kHz there was a source associated with the flow through the gap between the extended main element trailing-edge and the flap. The oil flow visualisation and the PIV measurements showed a significant spanwise flow through the gap with the associated generation of free shear layers that impinged on the flap suction surface. The spanwise flow and associated vorticity was also convected over the sharp flap edges and therefore acted to efficiently scatter any generated acoustic waves. At 10 kHz the noise source was still present. At higher frequencies, the source no longer existed.

As the airspeed increased to 30 m/s (Figure 6.23), the low to mid frequency data were swamped by broadband background noise. At 8 kHz, the noise source associated with the gap increased by 11 dB. This increase was associated with the higher airspeed and the stronger flap side-edge vortex, which resulted in a higher flow speed though the gap. At a frequency of 10 kHz, the source was still present. The resolution of the array at this frequency was 30 mm. The dimension of the gap along the flap chord from the minimum gap, where the gap was effectively closed, to the main element trailing-edge was approximately 90 mm. The approximate dimension of the source greater than 6 dB over the background levels in the x direction was 60 mm. The source was concentrated towards the trailing-edge of the main element where the gap dimension was largest. Near the leading-edge of the flap, the gap was small and the flow was constrained through the gap. This led to the formation of a weaker vortex and therefore the noise associated with the spanwise flow through the gap was less.

As the flap deflection angle was increased to 39 degrees (Figure 6.24), the beamforming

plots at 20 m/s and frequencies of 2 kHz and 4 kHz were dominated by the wind tunnel broadband noise. At 8 kHz the spatial extent of the source had greatly increased over its value at a flap deflection angle of 29 degrees. This was caused by the increase in the gap dimension with an increase in flap deflection angle. There was also an increase in the strength and size of the vortex at the higher flap deflection angle. The increase was caused by the greater circulation around the flap at the higher flap deflection angle, thereby creating a stronger side-edge vortex. The increase in vortex strength is also contributed to by the larger gap dimension, which allowed a stronger secondary vortex to form on the suction surface of the flap. It also allowed vortex merger to occur earlier than for the smaller flap deflection case. The source strength was 2 dB higher than the flap deflection angle of 29 degrees case at 8 kHz. At a frequency of 10 kHz a prominent source occupied a large part of the suction surface of the flap. This source was located forward of the point where the vortex separated from the flap suction surface as determined by the oil flow measurements. At this frequency the source strength was 4 dB higher than the 29 degree flap deflection angle configuration.

As the airspeed was increased to 30 m/s for this configuration (Figure 6.25), the beamforming plots of the mid frequencies of 2 kHz and 4 kHz were again dominated by broadband background noise. At 8 kHz the source was located at the overlap region between the flap side-edge and the trailing-edge of the main element. Similar features were found for the other high frequencies as for the flap deflection angle of 29 degrees. The main element angle of attack was increased to 10 degrees (Figure 6.26). The effect of the increase in angle of attack was to move the source on the flap side-edge towards the trailing-edge. There was also a slight increase of 1.5 dB in the magnitude of the source at 8 kHz. This was associated with a stronger vortex at the increased angle of attack.

6.3.2 Porous Side-Edge

An open cell porous material was applied to the last 4% of the half-span flap as shown in Figure 6.27. The beamforming plots for a freestream velocity of 30 m/s, a main element angle of attack of 5 degrees and a flap deflection angle of 39 degrees are shown in Figure 6.28. At 2 kHz and 4 kHz the wind tunnel background noise dominated and the plots were broadband in nature. At 8 kHz there was a slight reduction in the source strength at the flap side-edge compared to the hardwall case in Figure 6.25. The ΔdB reduction in the peak source strength was 2 dB at a distance of 1.061 m from the flap. At a frequency of 10 kHz there was a 3.5 dB reduction in the noise.

A plot of the change in sound pressure level with the application of a porous side-edge is shown in Figure 6.29 averaged over one-third octave bands. The change in sound pressure level is calculated by subtracting the hardwall data from the porous flap

side-edge data. The same flow conditions and configuration were applied except for the application of the porous material. The porous material was most efficient at reducing the mid frequency noise. This was achieved by reducing the magnitude of vorticity in the turbulent shear layer and displacing the vortex further away from the surface. For the split flap configuration it also had the advantage of impeding the flow through the gap between the flap and the extended trailing-edge of the main element. This reduced the magnitude of the spanwise component of the flow through the gap. The porous material had the effect of shifting the frequency of the noise higher in the spectrum. The noise at 10 kHz and above were greater than hardwall case. However, the sound pressure levels were much reduced at the higher frequencies since most of the flap side-edge noise was generated at mid frequencies. The frequencies mentioned in this discussion were model frequencies. At an approach Mach number of 0.2 and a geometric chord of 3.5 m, the full scale frequencies are $0.78f_m$ and $0.52f_m$ at an airspeed of 20 and 30 m/s respectively, where f_m is the model frequency.

6.4 Nearfield Acoustics

6.4.1 Hardwall

At a flap deflection angle of 29 degrees, the gap was narrowed between the deflected and the undeflected portions of the flap near the leading-edge of the flap, as shown in Figure 6.2. This greatly impeded the flow around the flap side-edge, which interrupted the formation of the side-edge vortex. At an airspeed of 10 m/s, an angle of attack of 5 degrees and a flap deflection angle of 29 degrees, Mic 1 on the side-edge, showed a peak at 2200 Hz with an amplitude of 62 dB. This is shown in Figure 6.30(a). These results are compared to the values for the hardwall case without the split flap, where the formation of the flap side-edge vortex was unimpeded, presented previously in Chapter 4. The original configuration without the split flap is referred to as the baseline configuration.

As the flap deflection angle was increased to 39 degrees, the gap between the deflected and undeflected portions of the flap increased (Figure 6.2). The high speed flow through this gap induced higher velocities around the flap side-edge. This high speed flow was in the vicinity of sharp edges, which acted to efficiently scatter generated acoustic waves. The features of note in the spectra at 39 degrees flap deflection angle, shown in Figure 6.30(b), were a removal of the low frequency tonal features as the spectra became more broadband. Compared to the hardwall case without the split flap, the levels of the low to mid frequencies were higher up to a frequency of 4000 Hz. The additional noise arose from the high speed flow through the gap at this flap deflection angle as determined in the flowfield measurements.

6.4.2 Porous Side-Edge

A porous side-edge of 40 PPI and a relative density of 10-12% was applied to the flap side-edge. This allowed some velocity to permeate through the porous material even at a flap deflection angle of 29 degrees where the gap was reduced. For both the flap deflection angles of 29 and 39 degrees, shown in Figure 6.31(a) and Figure 6.31(b) respectively, there was a reduction in levels over all the frequencies measured. The results were compared with the hardwall results for the split flap, discussed above and shown in Figure 6.30. At a flap deflection angle of 29 degrees, the flow was constricted through the gap between the main element trailing-edge and the flap. The application of a porous material to the flap side-edge alleviated this constriction and allowed a small transpiration velocity to pass through the material.

The spectra at an airspeed of 20 m/s and a flap deflection angle of 29 degrees and 39 degrees are shown in Figures 6.30(c) and Figure 6.30(d) respectively. At a flap deflection angle of 29 degrees, there were higher levels in the mid frequencies from 1400 Hz - 7000 Hz compared to the 10 m/s case. Again these levels were lower than the hardwall case without the split flap due to the limited gap between the two flaps constraining the flow around the flap side-edge. At a flap deflection angle of 39 degrees, there was a loss of tonal features as the broadband levels rose. The mid frequency broadband peak centered around 4000 Hz, which was characteristic of the hardwall case without the split flap, was not measured for this configuration. The effect of applying a porous material to the split flap configuration was again to reduce the mid frequencies compared to the hardwall case (Figure 6.31(d)).

The spectra at 30 m/s for the two flap deflection angles are shown in Figures 6.30(e) and 6.30(f) for the hardwall case. For the 29 degrees flap deflection angle, the main feature in the spectrum was a broadband hump from 2000 Hz to 7000 Hz. Again the sound pressure levels across the frequency range were lower than the hardwall case without the split flap. The effect of applying the porous side-edge at both flap deflection angles was to produce a significant drop in the mid frequencies compared to the hardwall case (Figures 6.31(e) and 6.31(f)). This was caused by the porous material reducing the strength of the vortex and slowing the flow rate through the gap resulting in weaker shear layers being generated.

6.5 Summary

The split flap configuration altered the formation and evolution of the flap side-edge vortex system. It also introduced an additional noise source, i.e. the high speed flow through the gap between the main element trailing-edge and the deflected flap. The

split flap configuration had additional noise in the nearfield compared to the baseline configuration. It was found that the gap between the trailing-edge of the main element and the flap was a crucial parameter in determining the noise generated. When the flow was constrained through the gap, lower levels of nearfield noise in the mid frequency range were measured. The application of a porous flap side-edge reduced the strength of the vortex and therefore the magnitude of the crossflow component of velocity through the gap. This resulted in a reduction in the efficiency of the source present at the gap.

6.6 Figures

FIGURE 6.1: Picture of wind tunnel model with a split flap. Flow is from left to right.

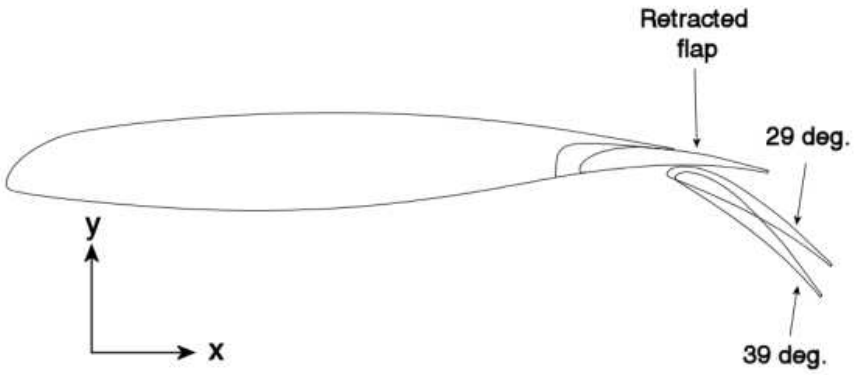

FIGURE 6.2: Schematic showing the two flap deflection angles and the retracted flap that formed the main element trailing-edge.

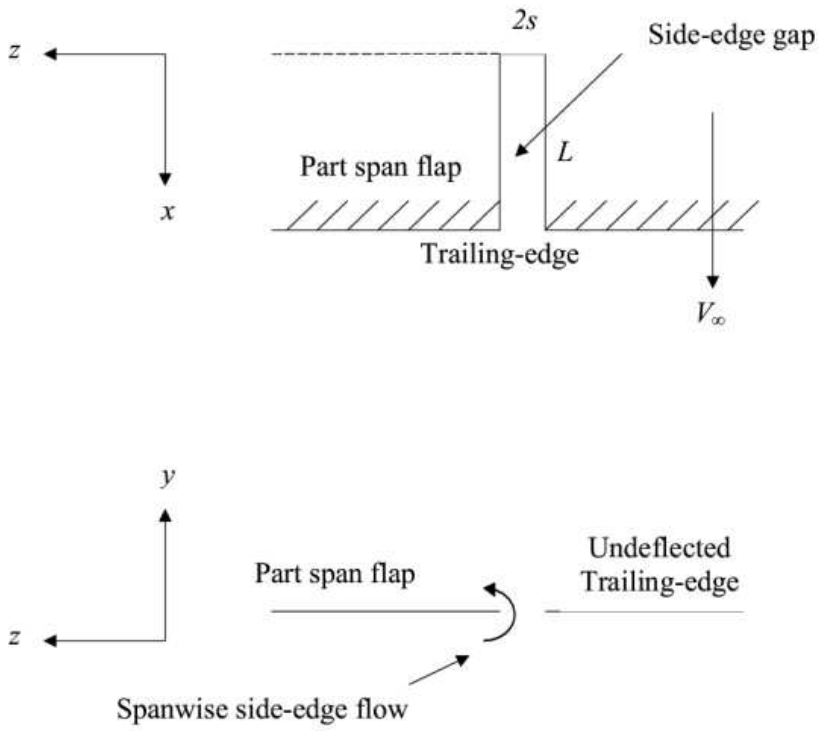

FIGURE 6.3: Schematic of Howe's model using coordinate system as defined in this work [64].

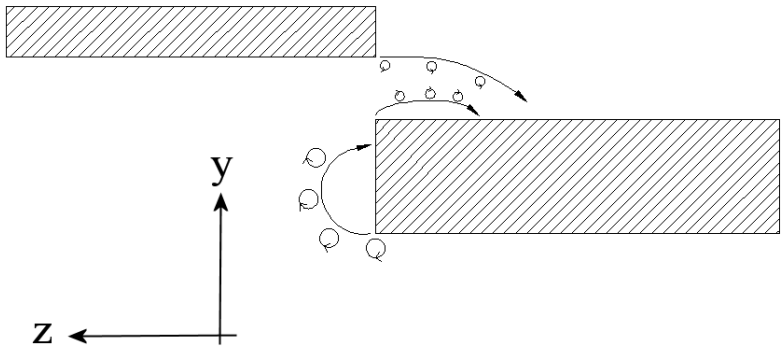

FIGURE 6.4: Schematic of flow around split flap configuration. The freestream velocity vector points out from the page.

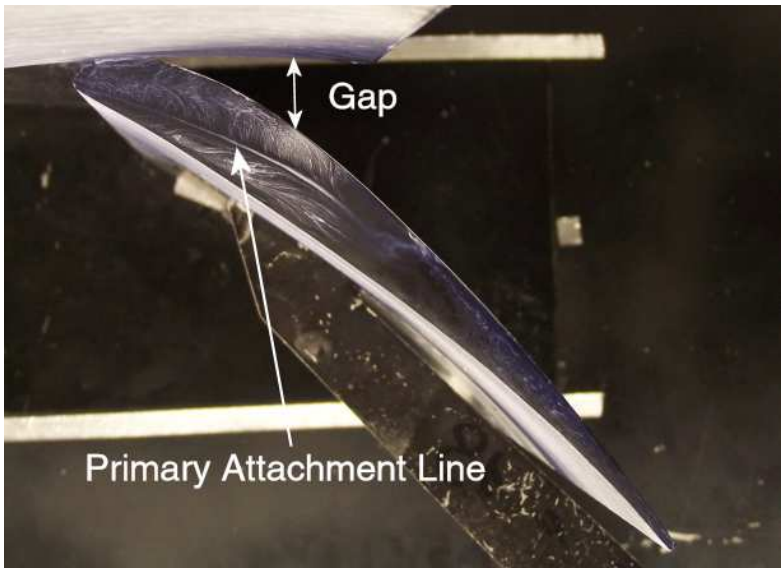

FIGURE 6.5: Oil flow visualisation of flap side-edge. Flow is from left to right.

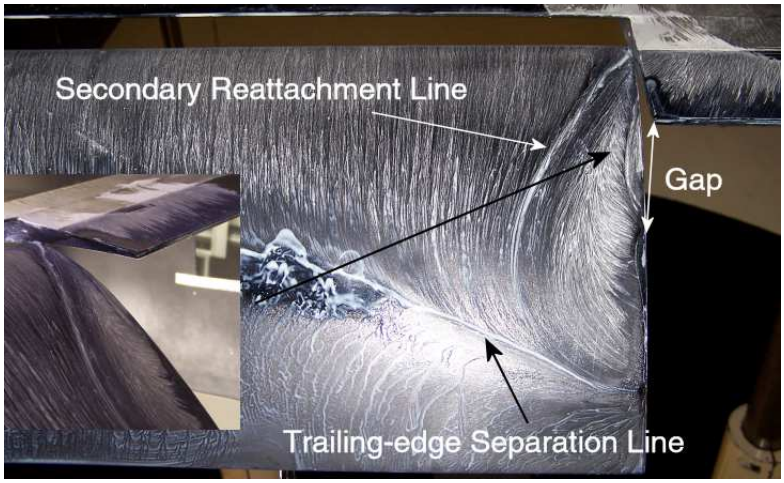

FIGURE 6.6: Oil flow of suction surface of flap. View looking upstream.

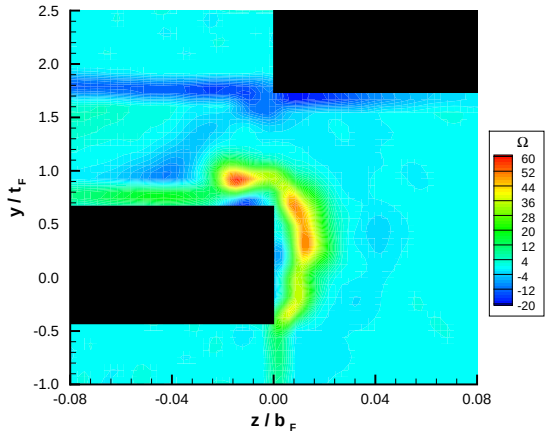

FIGURE 6.7: x vorticity contours at $x_F/c_F = 0.2$. $V_\infty = 20$ m/s, $\alpha = 5$ deg., $\delta_F = 29$ deg.

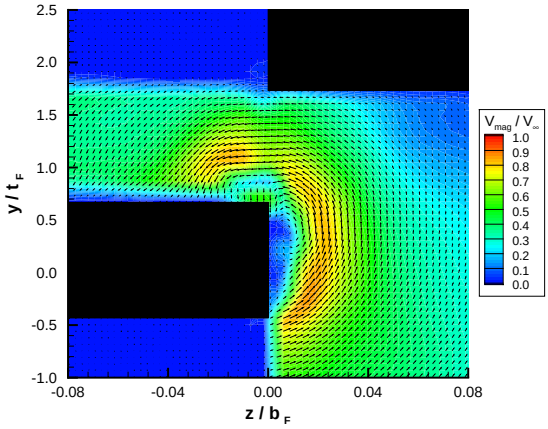

FIGURE 6.8: Velocity magnitude contours at $x_F/c_F = 0.2$. $V_\infty = 20$ m/s, $\alpha = 5$ deg., $\delta_F = 29$ deg.

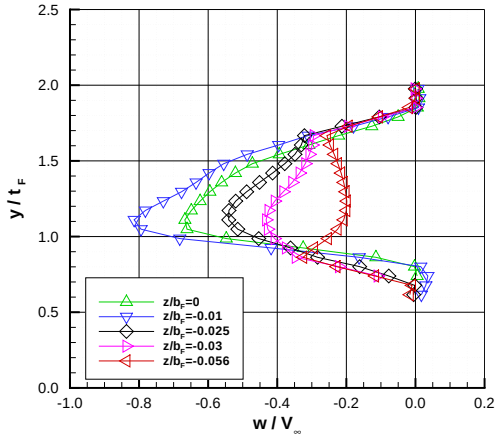

FIGURE 6.9: Velocity distributions through the gap at $x_F/c_F = 0.2$. $V_\infty = 20$ m/s, $\alpha = 5$ deg., $\delta_F = 29$ deg.

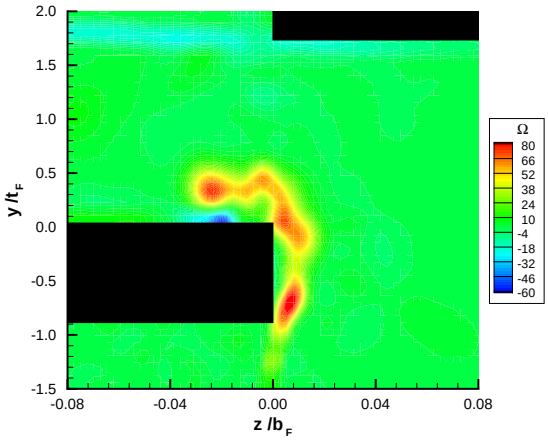

FIGURE 6.10: x vorticity contours at $x_F/c_F = 0.2$. $V_\infty = 20$ m/s, $\alpha = 5$ deg., $\delta_F = 39$ deg.

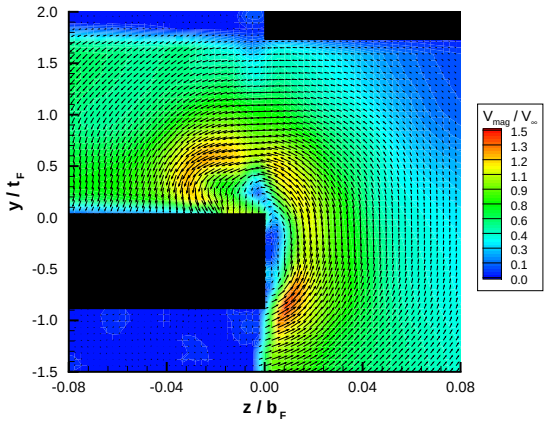

FIGURE 6.11: Velocity magnitude contours at $x_F/c_F = 0.2$. $V_\infty = 20$ m/s, $\alpha = 5$ deg., $\delta_F = 39$ deg.

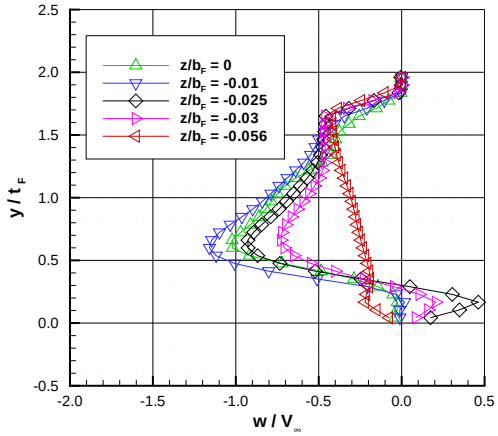

FIGURE 6.12: Velocity distributions through the gap at $x_F/c_F = 0.2$. $V_\infty = 20$ m/s, $\alpha = 5$ deg., $\delta_F = 39$ deg.

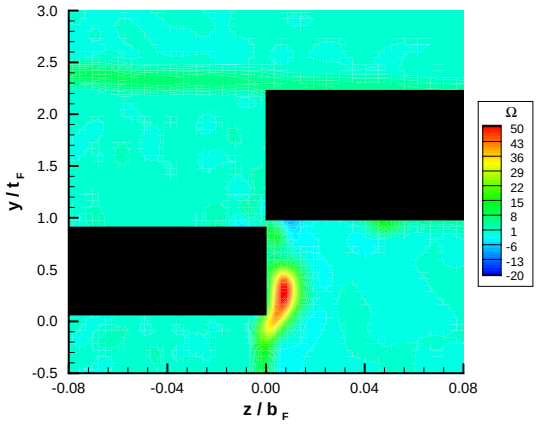

FIGURE 6.13: x vorticity contours at $x_F/c_F = 0.1$. $V_\infty = 20$ m/s, $\alpha = 5$ deg., $\delta_F = 29$ deg.

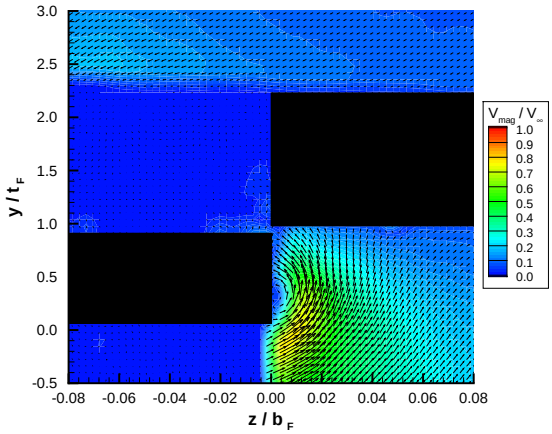

FIGURE 6.14: Velocity magnitude contours at $x_F/c_F = 0.1$. $V_\infty = 20$ m/s, $\alpha = 5$ deg., $\delta_F = 29$ deg.

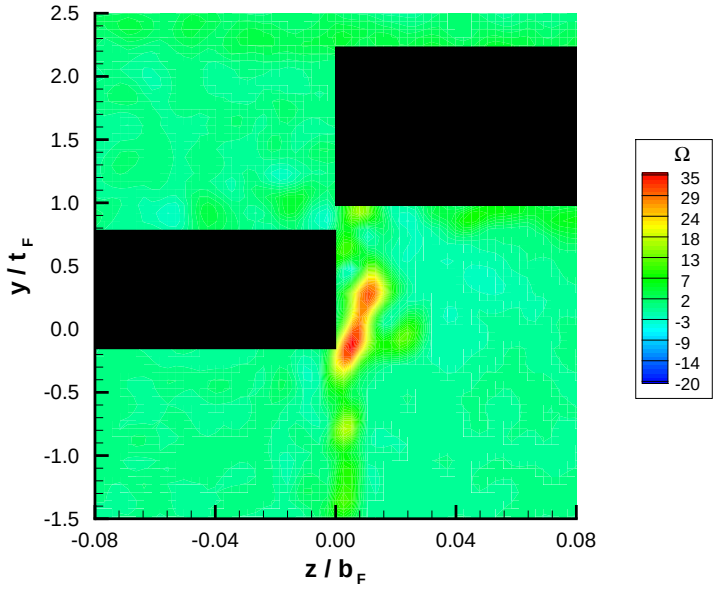

FIGURE 6.15: x vorticity contours at $x_F/c_F = 0.1$. $V_\infty = 20$ m/s, $\alpha = 5$ deg., $\delta_F = 39$ deg.

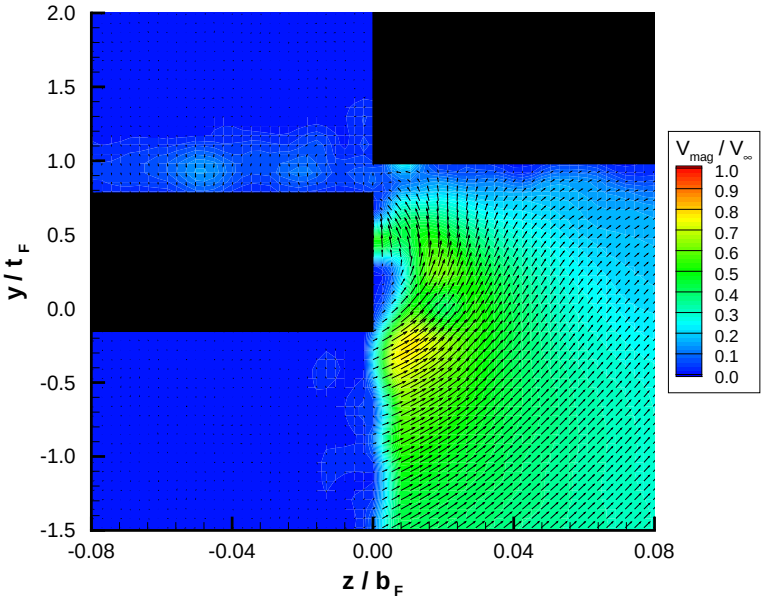

FIGURE 6.16: Velocity magnitude contours at $x_F/c_F = 0.1$. $V_\infty = 20$ m/s, $\alpha = 5$ deg., $\delta_F = 39$ deg.

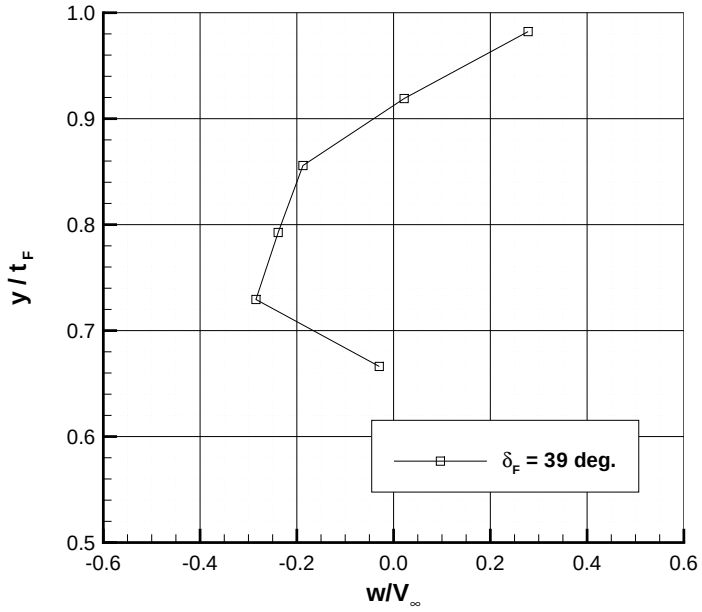

FIGURE 6.17: Velocity distribution at plane 2. z/b_F = -0.01. V_∞ = 20 m/s, α = 5 deg., δ_F = 39 deg.

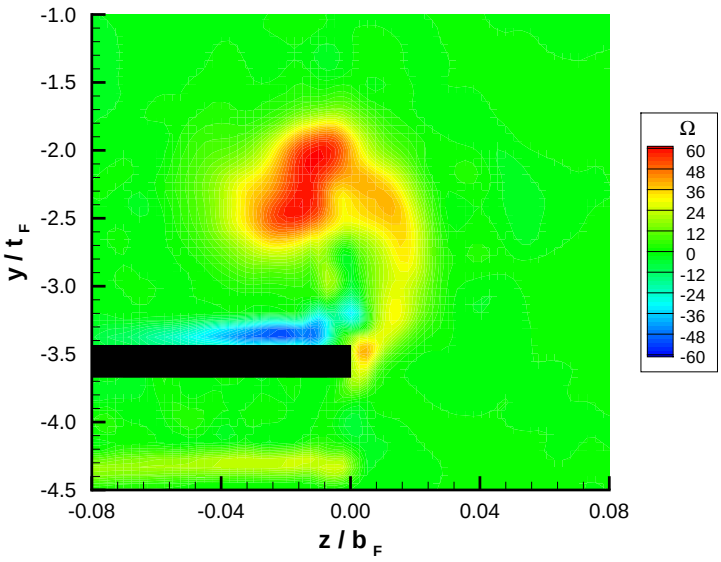

FIGURE 6.18: x vorticity contours at plane 3. V_∞ = 20 m/s, α = 5 deg., δ_F = 29 deg.

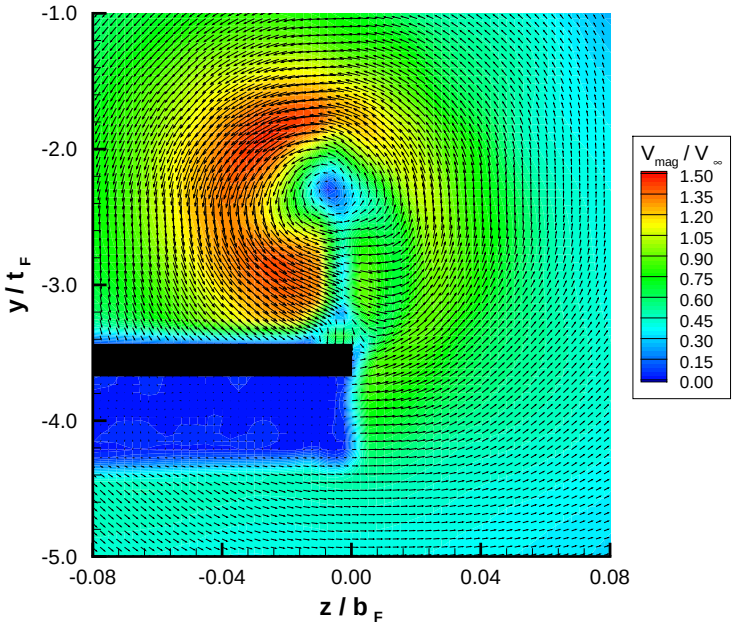

FIGURE 6.19: Velocity magnitude contours at $x_F/c_F = 0.8$. $V_\infty = 20$ m/s, $\alpha = 5$ deg., $\delta_F = 29$ deg.

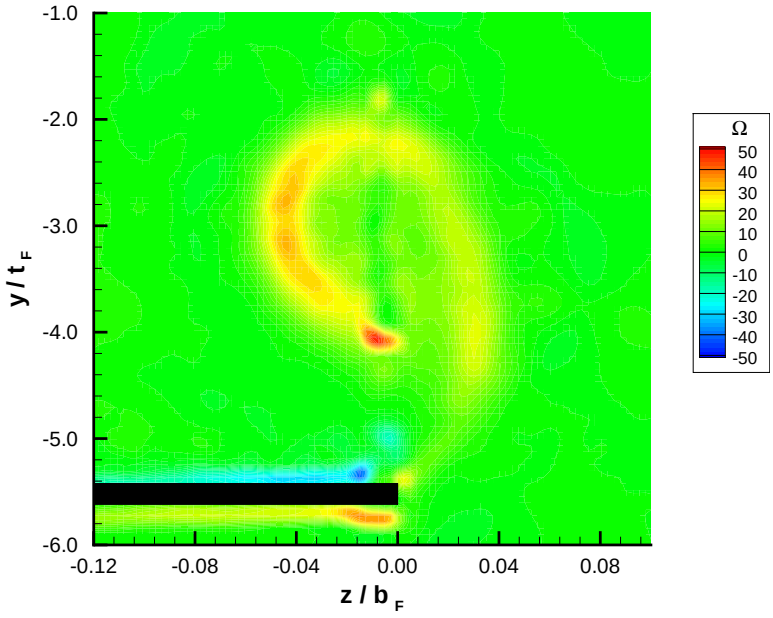

FIGURE 6.20: x vorticity contours at $x_F/c_F = 0.8$. $V_\infty = 20$ m/s, $\alpha = 5$ deg., $\delta_F = 39$ deg.

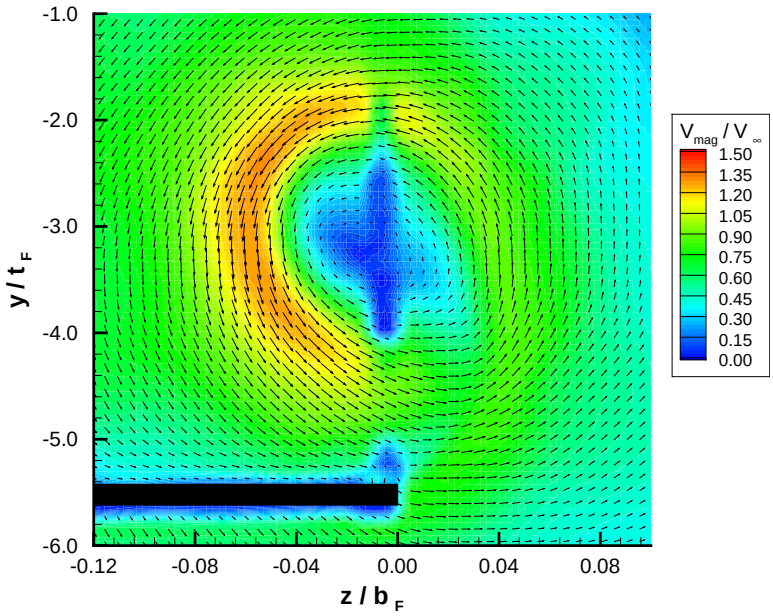

FIGURE 6.21: Velocity magnitude contours at $x_F/c_F = 0.8$. $V_\infty = 20$ m/s, $\alpha = 5$ deg., $\delta_F = 39$ deg.

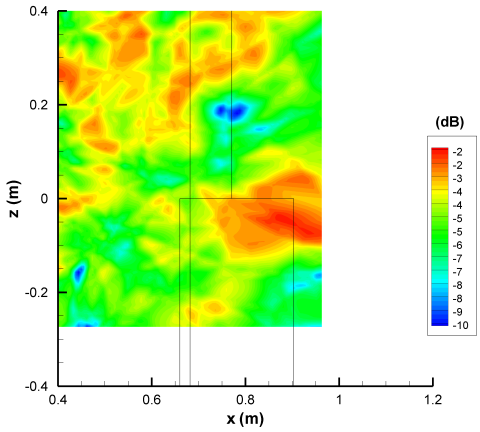

(a) 2 kHz

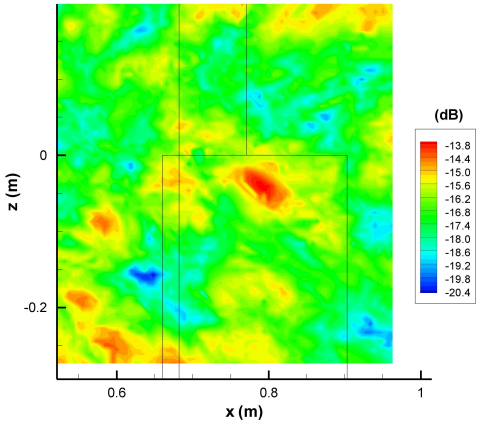

(b) 4 kHz

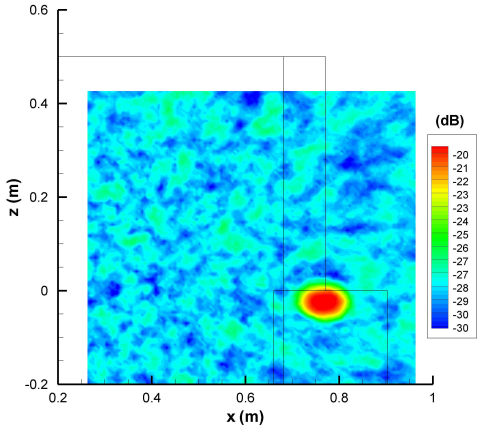

(c) 8 kHz

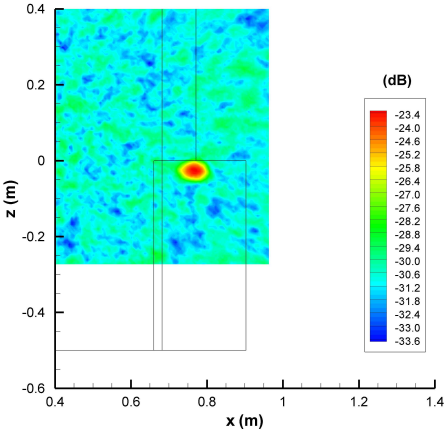

(d) 10 kHz

FIGURE 6.22: Phased microphone array results. $V_\infty = 20$ m/s, $\alpha = 5$ deg., $\delta_F = 29$ deg.

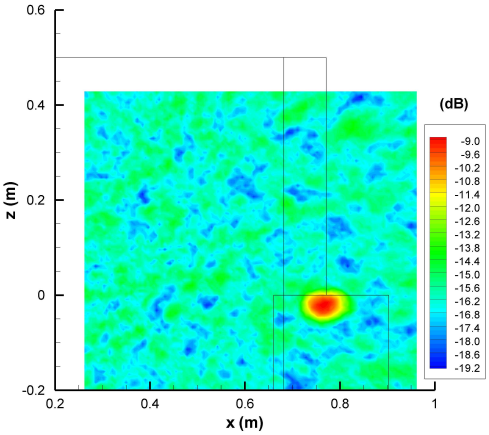

(a) 8 kHz

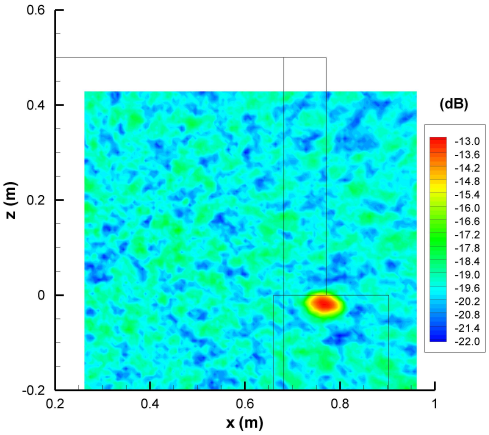

(b) 10 kHz

FIGURE 6.23: Phased microphone array results. $V_\infty = 30$ m/s, $\alpha = 5$ deg., $\delta_F = 29$ deg.

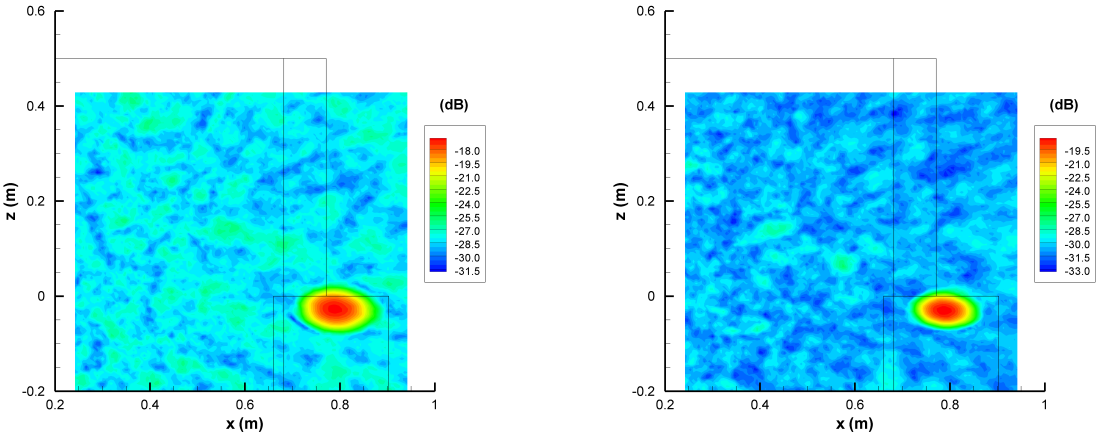

(a) 8 kHz (b) 10 kHz

FIGURE 6.24: Phased microphone array results. $V_\infty = 20$ m/s, $\alpha = 5$ deg., $\delta_F = 39$ deg.

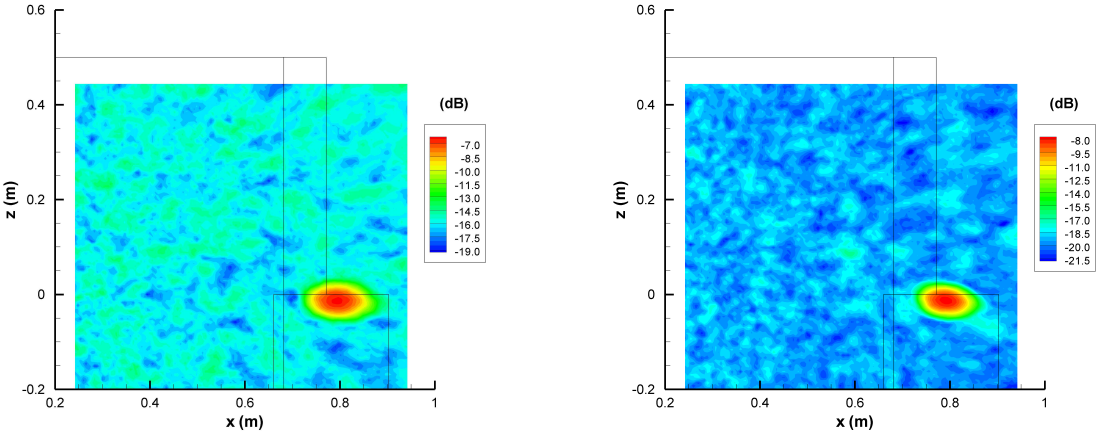

(a) 8 kHz (b) 10 kHz

FIGURE 6.25: Phased microphone array results. $V_\infty = 30$ m/s, $\alpha = 5$ deg., $\delta_F = 39$ deg.

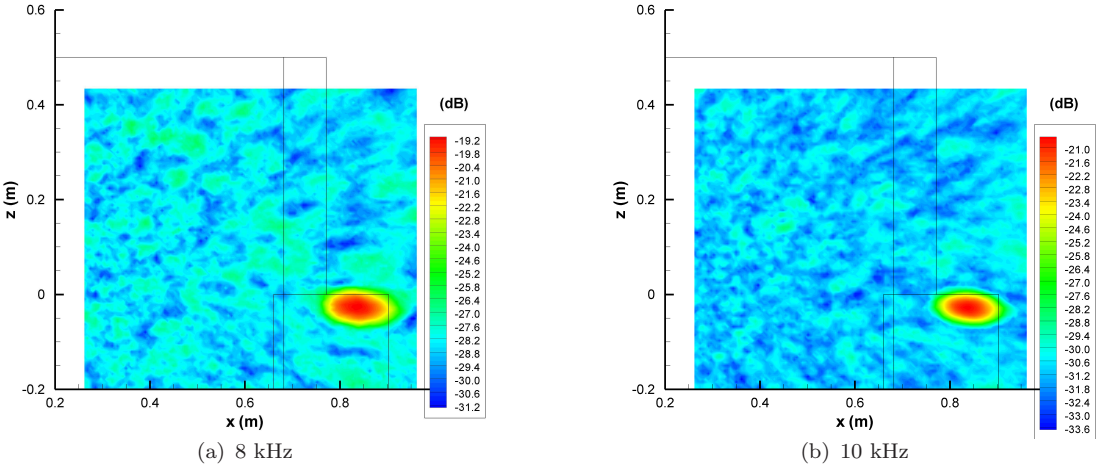

(a) 8 kHz (b) 10 kHz

FIGURE 6.26: Phased microphone array results. $V_\infty = 20$ m/s, $\alpha = 10$ deg., $\delta_F = 39$ deg.

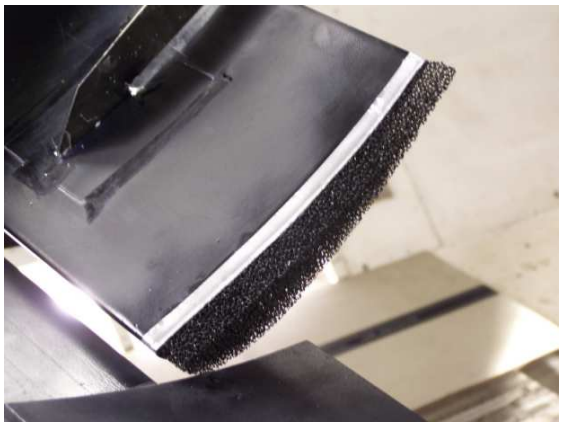

FIGURE 6.27: Porous material applied to the flap side-edge.

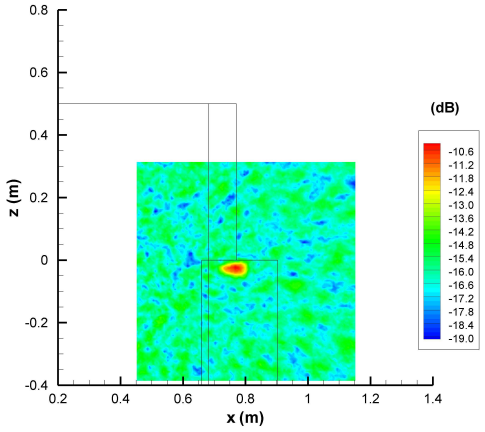

(a) $V_\infty = 30$ m/s, $\alpha = 5$ deg., $\delta_F = 29$ deg. 8 kHz.

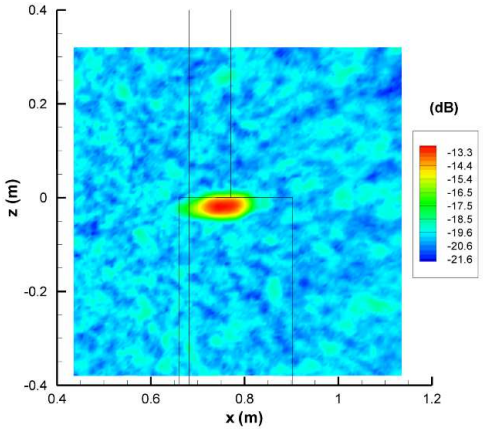

(b) $V_\infty = 30$ m/s, $\alpha = 5$ deg., $\delta_F = 29$ deg. 10 kHz.

FIGURE 6.28: Phased microphone array results with porous flap side-edge.

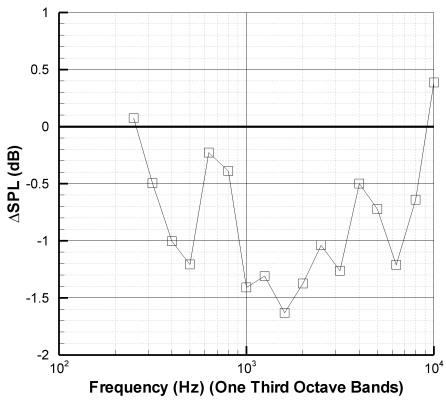

FIGURE 6.29: Change in sound pressure level between hardwall and porous flap side-edges. Averaged over one-third octave bands.

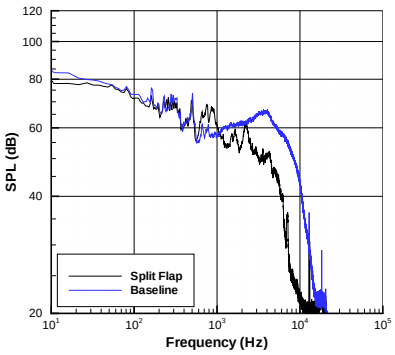

(a) $V_\infty = 10$ m/s, $\alpha = 5$ deg., $\delta_F = 29$ deg.

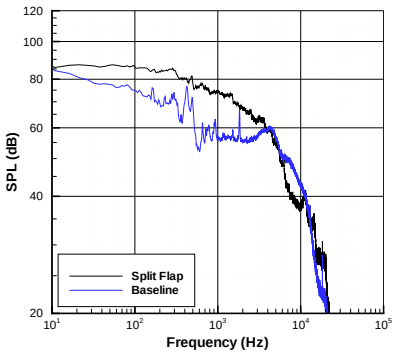

(b) $V_\infty = 10$ m/s, $\alpha = 5$ deg., $\delta_F = 39$ deg.

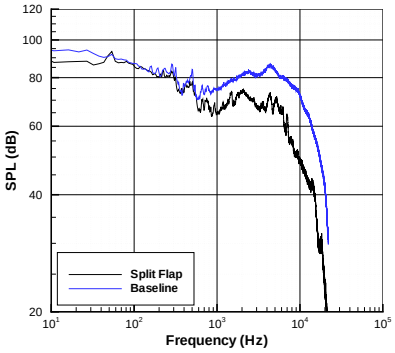

(c) $V_\infty = 20$ m/s, $\alpha = 5$ deg., $\delta_F = 29$ deg.

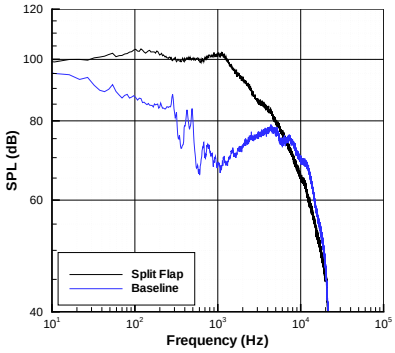

(d) $V_\infty = 20$ m/s, $\alpha = 5$ deg., $\delta_F = 39$ deg.

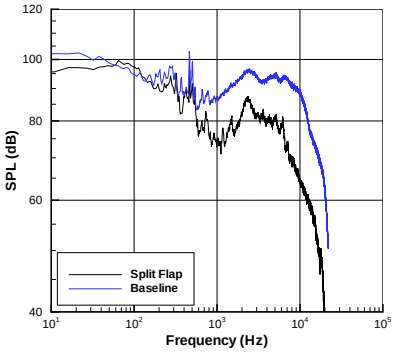

(e) $V_\infty = 30$ m/s, $\alpha = 5$ deg., $\delta_F = 29$ deg.

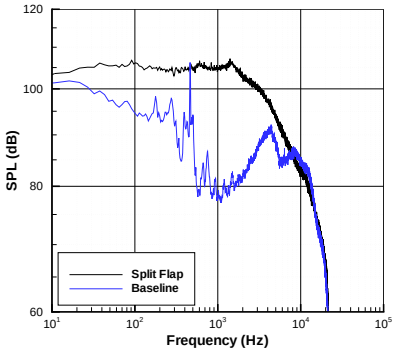

(f) $V_\infty = 30$ m/s, $\alpha = 5$ deg., $\delta_F = 39$ deg.

FIGURE 6.30: Comparison of hardwall microphone measurements on split flap configuration with baseline configuration (Mic 1).

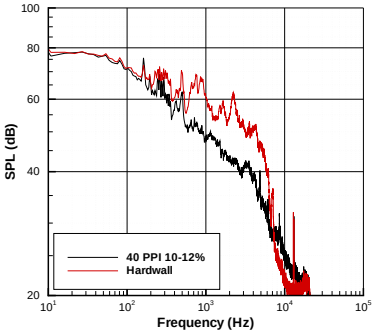

(a) $V_\infty = 10$ m/s, $\alpha = 5$ deg., $\delta_F = 29$ deg.

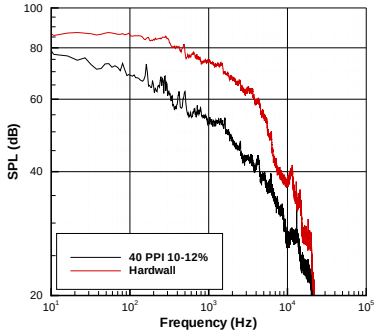

(b) $V_\infty = 10$ m/s, $\alpha = 5$ deg., $\delta_F = 39$ deg.

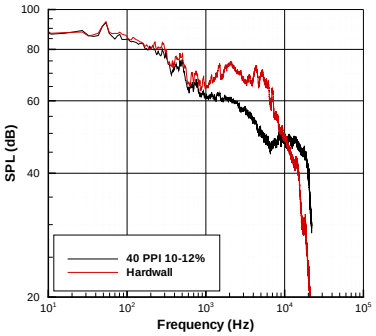

(c) $V_\infty = 20$ m/s, $\alpha = 5$ deg., $\delta_F = 29$ deg.

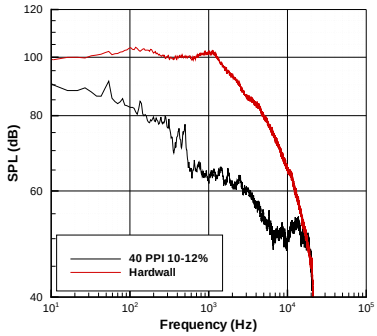

(d) $V_\infty = 20$ m/s, $\alpha = 5$ deg., $\delta_F = 39$ deg.

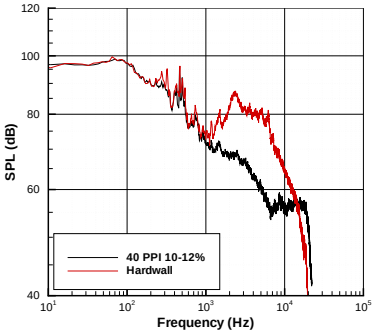

(e) $V_\infty = 30$ m/s, $\alpha = 5$ deg., $\delta_F = 29$ deg.

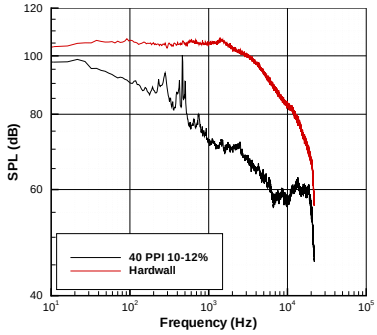

(f) $V_\infty = 30$ m/s, $\alpha = 5$ deg., $\delta_F = 39$ deg.

FIGURE 6.31: Comparison of microphone measurements on split flap configuration with porous treatment with split flap hardwall measurements (Mic 1).

Chapter 7

Numerical Models

This chapter describes the computational methodology, including flow solver and turbulence model used for the detached eddy simulation presented in Chapter 8. Also discussed are the computational grids that were used and the boundary conditions that were applied.

7.1 Governing Equations

The equations solved were the unsteady, compressible Navier-Stokes equations. For a turbulent flow the instantaneous value is equal to the sum of the ensemble-averaged component and the fluctuating component, e.g. $u_i = \bar{u}_i + u'_i$. The Favre-averaged Navier-Stokes equations for variable-density flow are given in Equations 7.1 - 7.3.

$$\frac{\partial \bar{\rho}}{\partial t} + \frac{\partial \bar{\rho}\bar{u}_i}{\partial x_i} = 0 \,. \tag{7.1}$$

$$\frac{\partial \bar{\rho}\bar{u}_i}{\partial t} + \frac{\partial \bar{\rho}\bar{u}_i\bar{u}_j}{\partial x_j} = -\frac{\partial \bar{p}}{\partial x_i} + \frac{\partial}{\partial x_j}\big(-\overline{\rho u'_i u'_j} + \bar{\tau}_{ij}\big) \,. \tag{7.2}$$

$$\begin{aligned}\frac{\partial \bar{\rho}\bar{E}}{\partial t} + \frac{\partial}{\partial x_j}\Big(\Big(\bar{\rho}\bar{E} + \bar{p}\Big)\bar{u}_j\Big) &= -\frac{\partial}{\partial x_j}\Big(\bar{q}_j + \overline{\rho u'_j e'}\Big) \\ &+ \frac{\partial}{\partial x_j}\Big(\bar{u}_i\big(\bar{\tau}_{ij} - \overline{\rho u'_i u'_j}\big)\Big) + \frac{\partial}{\partial x_j}\Big(\overline{\tau_{ij}u'_i} - \frac{1}{2}\overline{\rho u'_j u'_i u'_i}\Big) \,.\end{aligned} \tag{7.3}$$

The terms u'_i and e' are the unresolved turbulent fluctuations in velocity and specific internal energy respectively. The Favre-averaged total energy is given by,

$$\bar{\rho}\bar{E} = \bar{\rho}\big(\bar{e} + \frac{1}{2}\bar{u}_i\bar{u}_i\big) + \frac{1}{2}\overline{\rho u'_i u'_i} \,, \tag{7.4}$$

where $\bar{e}$ is the Favre-averaged specific energy. The two additional terms compared to the instantaneous Navier-Stokes equations are $\overline{\rho u_i' u_j'}$ and $\overline{\rho u_j' e'}$, the Reynolds stress tensor and the turbulent heat flux respectively. The Boussinesq assumption was employed to relate the Reynolds stresses to the mean velocity gradients. This results in the following viscous stress tensor,

$$\bar{\tau}_{ij} = (\mu + \mu_t)\left[\left(\frac{\partial \bar{u}_j}{\partial x_i} + \frac{\partial \bar{u}_i}{\partial x_j}\right) - \frac{2}{3}\frac{\partial \bar{u}_k}{\partial x_k}\delta_{ij}\right], \tag{7.5}$$

where μ_t is the turbulent viscosity. The heat flux vector is given as follows,

$$\bar{q}_j = -\left(\frac{\mu}{Pr} + \frac{\mu_t}{Pr_t}\right)c_p \frac{\partial \bar{T}}{\partial x_j}, \tag{7.6}$$

where Pr_t is the turbulent Prandtl number (the ratio of viscous diffusion to thermal diffusion). The third term on the right hand side of Equation 7.3 represents molecular diffusion and turbulent transport of turbulent kinetic energy. Both these terms were ignored based on order of magnitude arguments [81]. Also viscous terms involving fluctuating quantities in the stress tensor were ignored. The contributions of turbulent fluctuations to the total energy in Equation 7.4 were also ignored.

7.2 Solver

The solver was a cell-centered, finite volume CFD code. A pressure-velocity correction approach was applied to solve the governing equations. The discretisation scheme for pressure was second order. For density and energy the discretisation scheme was second order upwind. For momentum and modified turbulent viscosity (the transport variable in the SA turbulence model) a central differencing scheme was used. The pressure-velocity correction algorithm used was SIMPLE (Semi-Implicit Method for Pressure-Linked Equations), to enforce mass conservation and to obtain the pressure field. The time scheme was an implicit second-order time scheme with dual time stepping.

The computations were performed in parallel on a Linux cluster. The grid was divided into various subdomains or partitions that were then solved simultaneously using multiple computer nodes. The grid partitioning was performed automatically into equal size partitions.

7.3 Turbulence Modelling

A Detached-Eddy Simulation (DES) approach was employed as the turbulence model. The DES approach used was proposed by Shur *et al.* [82]. It is based on a one equation

Spalart-Allmaras (SA) RANS turbulence model with a modified length scale ($\widetilde{d}$). The SA model solves a transport equation for the modified turbulent viscosity ($\widetilde{\nu}$), where d is the distance to the nearest wall. The following equation describes the transport of $\widetilde{\nu}$,

$$\frac{\partial \tilde{\nu}}{\partial t} + \nabla \cdot (\tilde{\nu}\,\mathbf{V}) = c_{b1}[1 - f_{t2}]\tilde{S}\tilde{\nu} + \frac{1}{\sigma}\Big[\nabla \cdot ((\nu + \tilde{\nu})\nabla\tilde{\nu}) + c_{b2}(\nabla\tilde{\nu})^2\Big] - \left[c_{w1}f_w - \frac{c_{b1}}{\kappa^2}f_{t2}\right]\left[\frac{\tilde{\nu}}{d}\right]^2 \tag{7.7}$$

The modified turbulent viscosity ($\tilde{\nu}$) is related to the eddy turbulent viscosity (ν_t) as follows,

$$\nu_t = \tilde{\nu} f_{v1}\ . \tag{7.8}$$

The definition of the various functions and constants in the SA model are described in Appendix C.

A vorticity/strain relationship was used for the production term [83] as opposed to the original production term that was proportional to the magnitude of vorticity. The modified S in the production term is as follows,

$$S = |\Omega_{ij}| + C_{prod}\ \min\left(0, |S_{ij}| - |\Omega_{ij}|\right)\ , \tag{7.9}$$

where $|\Omega_{ij}|$ is the magnitude of vorticity, $C_{prod} = 2.0$ and $|S_{ij}|$ is the magnitude of the strain tensor. The effect of the modified production term, was to reduce the eddy viscosity in regions where the magnitude of vorticity exceeded the strain rate. In flows near vortex cores, the turbulence is known to be suppressed where the flow is subjected to pure rotation [83]. The default production term, based on the magnitude of vorticity over-predicts the eddy viscosity in the vortex core region.

In the SA model the wall destruction term is proportional to $(\widetilde{\nu}/d)^2$. When the destruction term is equal to the production term, the eddy viscosity is proportional to $\hat{S}\,d^2$, where $\hat{S}$ is the local strain rate. In a Large Eddy Simulation (LES), a sub-grid scale model is needed to solve the turbulent stresses that aren't solved directly. In the Smagorinski sub-grid scale model, the eddy viscosity is proportional to $\hat{S}\,\Delta^2$, where $\Delta = \max(\Delta x, \Delta y, \Delta z)$. If the distance to the nearest wall in the SA model (d) is replaced with the maximum cell dimension (Δ), the SA model behaves like a Smagorinski LES model. To exhibit RANS behaviour close to the wall and LES behaviour away from the wall, a modified length scale ($\widetilde{d}$) is defined as follows and replaces the length scale (d) in Equation 7.7,

$$\widetilde{d} = \min(d, C_{DES}\Delta). \tag{7.10}$$

When the distance to the nearest wall is smaller than $C_{DES}\Delta$ the model behaves as a RANS model. When $d > C_{DES}\Delta$ the model behaves in LES mode. The transition between the RANS and LES models can be controlled by modifying the constant C_{DES}

and locally refining the grid.

7.4 Grid Generation

A three-dimensional hybrid grid was created for the second-order CFD solution. The geometry consisted of a main element with a fixed leading-edge and a half-span flap. The span of the computational model was 0.8 m. This differed by 20% from the physical dimensions of the model. The reduction in spanwise length was to improve the quality and number of spanwise cells, which is crucial in providing adequate resolution in a DES computation. The difference of 20% was assumed to be negligible since the experimental oil flow visualisation and spanwise pressure distributions showed a quasi two-dimensional flow over this region. Therefore, this region was away from the influence of the flap side-edge.

The separated flow around the flap side-edge and corresponding vortices were the region of interest, where turbulence and the flowfield needed to be accurately resolved in the DES calculation. In the classic formulation of DES, the length scale is proportional to $\max(\Delta x, \Delta y, \Delta z)$ for the LES region. Therefore, the least expensive way to obtain a required spatial resolution is to have cubic cells [42]. This philosophy was followed in the nearfield flow of the flap side-edge as much as possible, with cells with an aspect ratio of unity in the wake immediately aft of the flap.

The viscous RANS region for the attached boundary layer had a first wall cell spacing of $y^+ = 2$ and a stretching ratio of 1.2. This follows the guidelines suggested by Spalart [42] for the log layer to be accurately resolved with the SA RANS model. There was no limit to the maximum spacing in the direction parallel to the wall (x^+) over the main element and flap. However, near the trailing-edge of each element, the spacing in the wall parallel direction was $x^+ = 4$. The spacing at the edge of the boundary layer needed to be controlled to avoid unresolved gradients in the eddy viscosity. No problems with numerical stability were found in this region.

Outside of the structured blocks that contained all the turbulence and vorticity generated by the solid walls as it convected downstream, an unstructured mesh was used to greatly reduce the total number of gird points that were needed. A fully structured grid from the nearfield out to the farfield leads to an excessive number of cells for a given accuracy in the nearfield. The final grid used for the DES calculation consisted of 4.7×10^6 cells and 72 blocks. Pictures of the computational grid are shown in Figures 7.1 - 7.4.

7.5 Boundary Conditions

The farfield boundary condition was a non-reflecting boundary condition based on Riemann invariants for a one-dimensional flow normal to the boundary. For a subsonic flow, the two Riemann invariants corresponding to an incoming and outgoing wave are,

$$R_\infty = u_{n,\infty} + \frac{2a_\infty}{\gamma - 1} \,, \tag{7.11}$$

and,

$$R_i = u_{n,i} - \frac{2a_i}{\gamma - 1} \,, \tag{7.12}$$

where u_n is the velocity normal to the boundary, a is the local speed of sound. The subscript ∞ refers to flow variables at infinity (the boundary condition), and the subscript i refers to interior flow variables. Adding and subtracting the two invariants in Equations 7.11 and 7.12 gives the following equations,

$$u_n = \frac{1}{2}(R_i + R_\infty) \,, \tag{7.13}$$

$$a = \frac{\gamma - 1}{4}(R_i - R_\infty) \,. \tag{7.14}$$

At the boundary, the values of tangential velocity and entropy are extrapolated from the interior. Using the values for normal velocity and speed of sound applied to the boundary, given in Equations 7.13 and 7.12 respectively, and the extrapolated values of tangential velocity and entropy, the flow variables at the boundary can be calculated.

The freestream boundary conditions are presented in Table 7.1.

Parameter	*Symbol*	*Value*
Freestream Mach Number	M	0.2
Main Element Angle of Attack	α	5 degrees
Flap Deflection Angle	δ_F	29 degrees
Reynolds Number	Re	4.6×10^6

TABLE 7.1: Inlet boundary conditions - detached eddy simulation.

The wall boundary condition was a no-slip boundary condition with the gradient of pressure normal to the wall set to zero. Density was calculated using the ideal gas law. A symmetry boundary condition was applied to the spanwise extents of the computational domain to simulate the presence of the endplates without incurring the cost of having to resolving the boundary layers on the endplates. Physically the flow conditions set at this boundary were no convective flux and no diffusive flux normal to the symmetry plane, i.e. the normal gradients of the flow variables were set to zero. The position of the boundary conditions are sketched in Figure 7.5.

One simulation was performed with a hardwall at the flap side-edge. Another had a porous boundary condition applied to the flap side-edge. The boundary condition used was a source term in the momentum equation to account for the momentum flux through the porous material, assuming a homogeneous material. The momentum source in tensor notation was defined as

$$S_i = -\left(\frac{\mu}{\alpha}v_i + C_2\frac{1}{2}\rho|v|v_i\right), \tag{7.15}$$

where α is the permeability and C_2 is the inertial resistance factor. The first term in Equation 7.15 was Darcy's law and the second term was an inertial loss term. In Darcy's law, the pressure drop across the porous material due to viscous effects is proportional to the velocity through the material and the thickness of the material. When velocities through the porous material are significant the inertial loss term also needs to be included. The pressure drop in this term is proportional to the dynamic head. Turbulence production was suppressed in the porous region.

The constants in Equation 7.15 were determined from the experimental data provided by the manufacturer of the porous material for the pressure drop across the material as a function of velocity. The pressure drop across a porous material was assumed to take the form of a second order polynomial,

$$\Delta p = AV + BV^2, \tag{7.16}$$

where $A = \mu/\alpha$ and $B = \frac{1}{2}\,\rho\, C_2$. The material was assumed to be isotropic so the constants had the same value in each or the three coordinate directions. A least squares fit was used to determine the constants in the polynomial expression to the experimental data, shown in Figure 7.6. The value of A was 118.4 Ns/m and the value of B was 59.2 kg/m^3.

7.6 Convergence Criteria

The physical timestep (Δt) was 5×10^{-5} s. This corresponded to a sampling frequency of 20000 Hz. According to the Niquest criteria this meant that the highest frequency that could be resolved was 10000 Hz. The timestep corresponded to a non-dimensional timestep of 4.25×10^{-3}, which meant 237 timesteps were needed for one convection length. An implicit dual time-stepping method was used with 20 sub-iterations for each timestep to ensure convergence. The solution was run to a non-dimensional time of approximately 80. Convergence was determined by monitoring global values like lift and drag and also pressure monitors around the vortex.

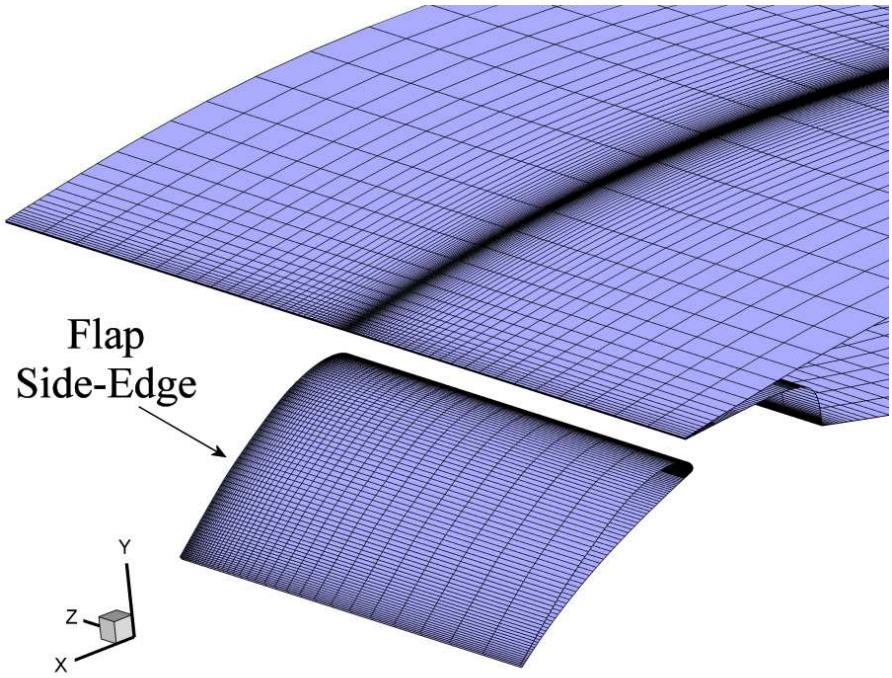

FIGURE 7.1: An overview of the on-surface grid.

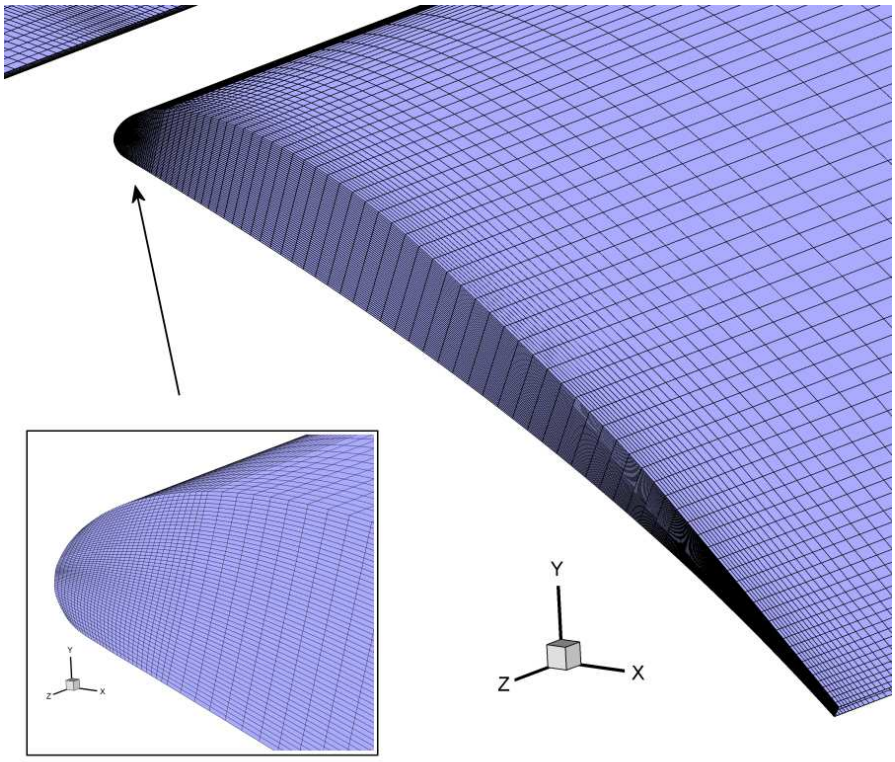

FIGURE 7.2: On-surface grid at flap side-edge.

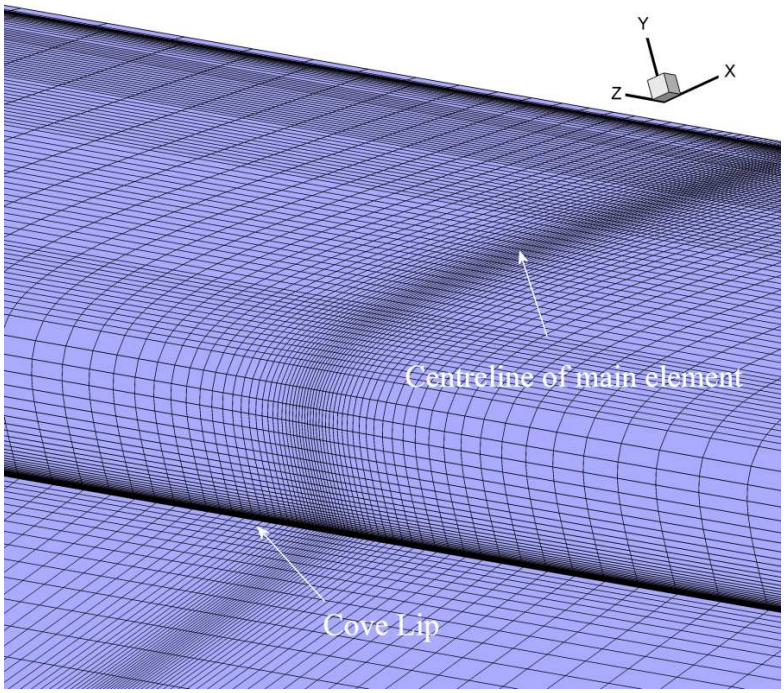

FIGURE 7.3: On-surface grid on main element cove.

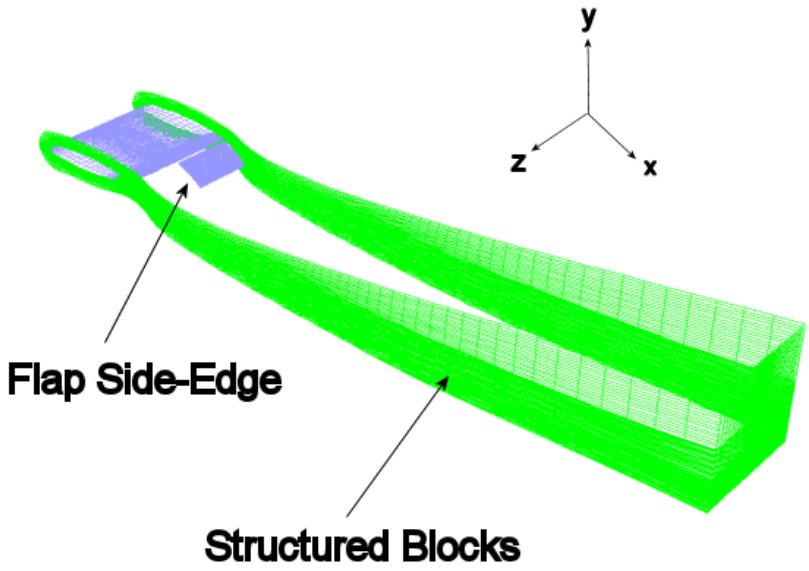

FIGURE 7.4: Illustration of structured blocks, which contain all the vorticity that is generated by the wing and flap as it is convected downstream.

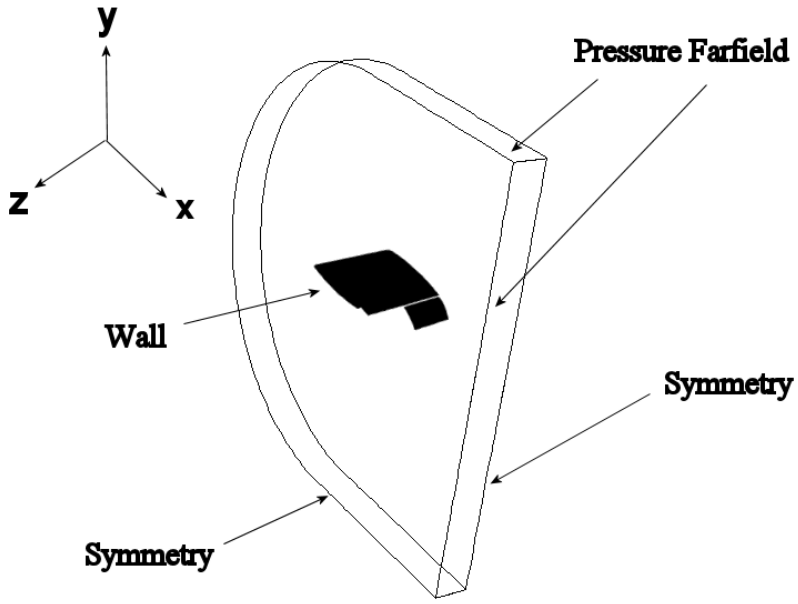

FIGURE 7.5: Sketch of boundary conditions (not to scale).

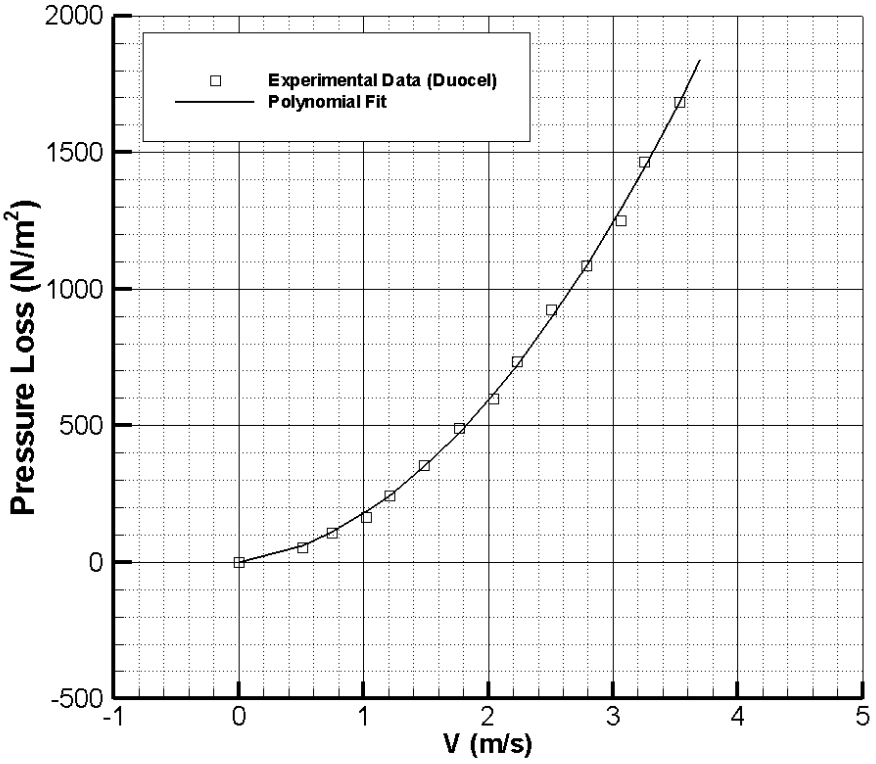

FIGURE 7.6: Experimental data for pressure loss through a porous material (40 PPI, density $10 - 12\%$) supplied by Duocel [79] with a second order polynomial trend line.

Chapter 8

Three-Dimensional Detached-Eddy Simulation

This chapter presents and discusses results of a Detached Eddy Simulation (DES) calculation of a flap side-edge flowfield. The purpose of this computation was to model the nearfield flow and to use the unsteady CFD data as an input to a Ffowcs-Williams Hawkings (FWH) solver to estimate the farfield acoustics. The CFD solver used was a commercial code Fluent and the FWH solver used was an in-house code written by Ashcroft [84] based on Farassat's 1A formulation [85]. A detached-eddy simulation was chosen to try and capture the significant off-surface unsteadiness. One of the limitations of Unsteady Reynolds-Averaged Navier-Stokes (URANS) is that it over-estimates the turbulent viscosity. This leads to excessive diffusion, which damps unsteadiness present in the flow. This is a particular problem in vortical flows where the use of URANS over-predicts turbulent viscosity due to high strain rates in the vortex. The use of DES in this study addressed some of these deficiencies.

8.1 Aerodynamic Flowfield

8.1.1 Symmetry Plane Flowfield

The spanwise extents of the computational domain were symmetry planes. This was to simulated the effect of the endplates. The flow in this plane was two-dimensional, with normal derivatives of flow variables to the plane set to zero. The flowfield at this position was away from influence of the flap side-edge vortex. The prominent flow features in the symmetry plane were a shear layer that detached from the main element cove, shedding from the main element trailing-edge and separation from the flap surface. These are shown in a plot of vorticity magnitude shown in Figure 8.1. The boundary layer on the

pressure surface separated from the main element cove and formed a shear layer of positive z vorticity. This shear layer was unstable and induced an unsteady flow in the flap cove region. The shear layer was then convected through a gap between the main element and the flap, and over the suction surface of the flap. Pressure perturbations from the unsteady flow in the main element cove propagated downwards and through the flap gap.

There was also shedding from the blunt trailing-edge of the main element. Due to a low pressure above the flap suction surface, the vorticity that originated from the blunt main element trailing-edge was deflected towards the flap suction surface. This interacted with the positive vorticity in the shear layer, which originated at the flap cove and was convected through the flap gap. This produced a highly unsteady flow above the flap suction surface. The flow on the flap suction surface separated at approximately $x_F/c_F \approx 0.6$ due to a strong adverse pressure gradient that acted on the flap. The unsteady flow due to the interaction of the trailing-edge shedding and the cove shear layer with the separated flow, caused a roll up of large discrete vortices. These vortices were then convected downstream of the flap as shown in Figure 8.1.

Pressure perturbations from this unsteady wake propagated in all directions as shown in Figure 8.2. This unsteadiness, due to the interaction of three sources of vorticity, was of significant strength. Even away from the flap side-edge, the flow over the two element geometry was significantly unsteady. These pressure perturbations provided large disturbances to amplify any instability mechanisms that were present in the side-edge vortex.

8.1.2 Flap Side-Edge Flowfield

Near the leading-edge of the flap, the flowfield was dominated by the presence of a dual vortex system as shown in Figure 8.3. The primary vortex originated from the pressure surface of the flap and was located on the side-edge. The secondary vortex was located on the suction surface. This vortex was caused by a shear layer that separated from the upper surface of the side-edge. This shear layer reattached on the suction surface of the flap. The primary vortex grew rapidly in the chordwise direction and eventually dominated the entire side-edge. The growth of the secondary vortex was reduced compared to that of the primary vortex. As the shear layer wrapped around the primary vortex impinged close to the suction surface, the secondary vortex was displaced further from the side-edge in the z direction.

Figure 8.4 shows the near-surface streamlines one cell off the surface. The primary attachment line was where the shear layer that detached from the flap suction surface, attached to the side-edge. This formed the extent of the primary vortex on the side-edge. The size of the primary vortex increased in the chordwise direction. Eventually

the primary attachment line moved from the side-edge to the suction surface. The primary and weaker secondary vortices merged to become a single vortex. The evolution of the vortex system in the streamwise direction is shown in Figure 8.5. After the primary and secondary vortices merged, the vortex separated from the flap surface. The vortex continued to be further displaced from the flap surface as it moved downstream. The vortex strength also decreased as the vortex grew in size and was displaced further from the surface.

The nearfield streamlines from the DES calculation were overlaid on the experimental oil flow from Chapter 4. This is shown in Figure 8.6. Although the major features were captured in the computation, there were two significant disparities. The primary attachment line determined by the DES calculation, was located further towards the suction surface than the equivalent feature on the oil flow. This suggested that the size of the primary vortex on the flap side-edge was larger and grew quicker in the DES calculation. There was also a disparity at the point where the shear layer, which was wrapped around the primary vortex, attached on the suction surface. This was the point of vortex merging. In the oil flow, this occurred at $0.41 < x_F/c_F < 0.44$ (the exact location of this point was difficult to determine in the oil flow visualisation since it moved). The point of attachment on the suction surface in the DES calculation was $x_F/c_F = 0.38$. The difference arose from the accelerated growth of the primary vortex on the flap side-edge in the simulation. The point on the flap where the merged vortex system separated from the flap was well predicted by the simulation. The location of this point was at $x_F/c_F = 0.62$ for both the simulation and the experiment.

From the plots of vorticity in the vortex in a series of streamwise planes (Figures 8.7 - 8.11) the strong shear layers, originating at the pressure surface of the side-edge, can be seen wrapped around the vortex. Eventually these broke down to discrete vortices been convected around the stronger main vortex. This interaction produced a significantly unsteady vortex.

Five $y - z$ planes were taken through the flap side-edge. These planes corresponded to the PIV measurement planes. Plane 1 is shown in Figure 8.7. The presence of two vortices can be seen. A strong vortex with negative x vorticity was at the lower edge of the flap side-edge. There was also a region of positive x vorticity attached to the flap side-edge. As shown in Figure 8.4, the flow beneath the primary attachment line flowed towards the pressure surface of the flap. This attached boundary layer on the side-edge was the source of the positive x vorticity. Vorticity due to the main element wake was located above the flap surface.

The vorticity in plane 2 is shown in Figure 8.8. At this plane, the primary vortex dominated almost the entire side-edge region. The secondary vortex also grew in strength.

This plane corresponded to a point prior to vortex merging. Plane 3 shows the merged vortices in Figure 8.9. The vorticity in the wake of the main element was deflected towards the flap surface due to the induced velocity of the vortex above the suction surface. The strongest vorticity was in the shear layer at the lower surface of the side-edge. This constant source of vorticity from the shear layer was fed into the vortex resulting in a strong, unsteady vortex.

Plane 4, shown in Figure 8.10, illustrates the vortex located away from the surface of the flap. The strength of the vortex core was weaker at this plane. There continued to be strong vorticity in the separated shear layer. The fifth and final plane is shown in Figure 8.11. The unsteady shear layer was wrapped around the extremity of the vortex. This interaction of vorticity resulted in a significantly unsteady vortex. At this plane the vortex had moved further away from the surface.

The pressure perturbation is defined for each point in the flowfield as follows ,

$$p' = p - p_{\text{mean}} \, . \tag{8.1}$$

These correspond to hydrodynamic perturbations in the flowfield. The pressure perturbations in the $x-y$ plane at the flap side-edge are shown in Figure 8.12. Three regions of significant unsteadiness were identified.

- Cove region (A): Due to instabilities in the shear layer, there was an unsteady flowfield induced in the main element cove.
- Trailing-edge shedding (B): There was an unsteady shear layer behind the blunt trailing-edge of the main element. This region also had contributions from the perturbations from the main element cove that were convected through the flap gap and past the main element trailing-edge.
- Flap side-edge vortex (C): Pressure perturbations arose from the interaction between the vortex and the unsteady shear layer. These perturbations grew in magnitude as the vortex grew in size as it moved downstream. There were also smaller pressure perturbations above the flap surface due to the weaker secondary vortex. The largest pressure perturbations were caused by the large amplitude displacements of the off-surface vortex aft of the trailing-edge of the flap.

A series of pressure perturbation plots were taken in five $y-z$ planes, which corresponded to the same planes as the above discussion on vorticity. The pressure perturbations in Plane 1 are shown in Figure 8.13. Pressure perturbations were associated with the primary vortex, the secondary vortex and the main element trailing-edge shedding. The pressure perturbations in plane 2 are shown in Figure 8.14. The pressure perturbations present in the main element wake were deflected closer to the flap suction surface. The

pressure perturbations were stronger at the secondary vortex compared to plane 1.

Plane 3 corresponded to a point after the two vortices had merged, shown in Figure 8.15. Here the merged vortex was a significant source of unsteadiness. The vortex interacted with the main element trailing-edge wake. Plane 4, shown in Figure 8.16, illustrates strong pressure perturbations above the flap suction surface. The sources of unsteadiness due to the flow around the flap grew stronger in the streamwise direction along the flap chord. This was caused by the amplitude of vortex displacements increasing in the streamwise direction. Plane 5 is shown in Figure 8.17. The off-surface vortex dominated with large pressure perturbations induced by the unsteadiness inherent in the vortical structure.

Pressure distributions over the main element and flap at five spanwise locations are shown in Figure 8.18. The pressure distribution on the main element was characterised by a mild suction peak at the leading edge. There was also a hump towards the trailing-edge on the pressure surface due to the cove. The pressure distribution over the flap near the side-edge was characterised by two peaks. The first location corresponded to $z/b_F = 0.0075$. The first peak on the flap pressure distribution corresponded to the suction peak of the secondary vortex on the suction surface of the flap. The second, stronger peak corresponded to the large suction caused by the post-merged separated vortex located above the flap surface.

The next spanwise location was $z/b_F = 0.0013$. The secondary vortex peak was stronger at this spanwise location. As mentioned previously, the secondary vortex was displaced inboard as it moved downstream before it merged with the primary vortex. The peak that corresponded to the primary vortex suction peak was weaker. The merged vortex was located above the flap side-edge ($z = 0$). Therefore, the influence of the merged vortex on the on-surface pressure was less as the distance from the side-edge was increased.

The third pressure distribution was at $z/b_F = 0.0275$. The influence of the weak secondary vortex was no longer felt at this spanwise location, which indicated a small diameter of the secondary vortex. The peak that corresponded to the primary vortex was weaker. The fourth location was $z/b_F = 0.0975$. The suction peak at the leading-edge of the flap was visible for the first time at this spanwise location. This indicated that the flow was less influenced by the presence of the side-edge. The peak that corresponded to the suction due to primary separated vortex was weaker than the suction peak at the leading-edge of the flap. The fifth pressure distribution was at the symmetry plane ($z/b_F = 1.0$). Away from the side-edge the influence of the vortex was less. At all the spanwise locations, the flap pressure distributions had little influence over the main element pressure distributions. The only significant difference was in the cove region.

Figure 8.19 shows three pressure distributions on the flap side-edge along three lines in the x direction. The first pressure distribution corresponded to $y/t_{F\max} = 0.12$. The effect of the weak primary vortex near the leading-edge on the flap side-edge resulted in a low pressure peak of $C_p = -4.87$. The effect of the strong vortex, before it separates from the surface, is shown up until $x = 0.94$ m. The second pressure distribution was at $y/t_{F\max} = 0.5$. The peak pressure location had moved significantly aft. The third pressure distribution was at $y/t_{F\max} = 0.82$. As the suction surface of the flap was approached, the pressure peak was stronger ($C_p = -9.02$). Aft of $x = 0.94$ m there was a region of reversed flow.

The spanwise pressure distribution on the flap is shown in Figure 8.20 at two different streamwise stations. The first pressure distribution was near the leading-edge of the flap at $x_F/c_F = 0.09$. This streamwise point was upstream of the point where the vortex impinged on the suction surface. The influence of the secondary vortex in the spanwise direction was not significant since it was so weak. At $x_F/c_F = 0.63$ the influence of the strong vortex on the spanwise pressure distribution can be seen. The peak pressure induced by the vortex dropped away rapidly in the spanwise direction.

A comparison of the experimental pressure distribution on the flap with the DES results is shown in Figure 8.21. The experimental data was taken at an angle of attack of 5 degrees, a flap deflection angle of 29 degrees and a freestream velocity of 30 m/s. The chordwise pressure distribution was taken on the centerline of the flap model at a spanwise coordinate of $z = 0.25$ m. There was good agreement between the two. The suction peak on the flap was predicted well in the simulation. A comparison of the spanwise pressure distributions is shown in Figure 8.22. The spanwise pressure distribution was taken at $x_F/c_F = 0.35$. Again the simulation predicted the pressure distribution adequately. The pressure drop due to the presence of the flap side-edge vortex was not detected in the experimental data since there were no pressure taps close enough to the side-edge. The closest pressure tap to the side-edge was 0.008 m from the edge. There was an aluminium rib at the side-edge, which was part of the construction of the model. This prevented any pressure taps been placed closer to the side-edge.

Figure 8.23 shows a sample boundary layer profile on the suction surface of the main element at $x/c = 0.9$. A comparison was made with the log-law in the overlap region, which showed the boundary layer on the main element was adequately resolved. The log law is as follows,

$$u^+ = \frac{1}{\kappa} \ln y^+ + B \ , \tag{8.2}$$

where $\kappa = 0.41$ and $B = 4.9$.

8.2 Ffowcs-Williams Hawkings Solution

Using the nearfield CFD data, the farfield acoustics were determined using a Ffowcs-Williams Hawkings (FWH) solver. The contributions from the volume integral term were ignored. An on-surface integration surface was used. The magnitude of the dipole term in the FWH equation is proportional to the Root Mean Square (RMS) of the on-surface pressure fluctuations with time,

$$\sqrt{\frac{1}{T_2 - T_1} \int_{T_1}^{T_2} \left[\frac{\partial p'}{\partial t} \right]^2 \mathrm{d}t} \, . \tag{8.3}$$

The magnitude of the on-surface dipole term is shown on the flap side-edge in Figure 8.24 and on the flap suction surface in Figure 8.25. The highest acoustic source on the flap side-edge was where the primary vortex spilled over onto the flap suction surface. There was also another high source near the trailing-edge of the flap, which corresponded to the separated unsteady flow on the side-edge behind the point where the vortex detached from the flap surface. On the suction surface of the flap, the highest acoustic source was where the vortex separated from the flap surface. Above this point a strong unsteady vortex was located close to the surface. The unsteady pressure perturbations from the vortex interacted with the solid flap surface and were radiated as sound. This strong unsteady vortex in the vicinity of the flap side-edge was the strongest acoustic source.

The directivity from the main element and flap in the $x - y$ plane are shown in Figures 8.26 and 8.27 respectively. Since an on-surface impermeable integration surface was used for the FWH solver, the only contributions were from dipole sources. The combined fafield directivity at 100 m from both the flap and the main element is shown in Figure 8.28. Both lobes for the dipole associated with the flap were approximately symmetric. This was not true for the directivity of the main element. This was due to the presence of the cove on the pressure surface of the main element, which altered the directivity of the sound radiated downwards and upstream.

The farfield directivity in the $x - z$ plane is shown in Figure 8.29. This was the contribution from the flap side-edge. The propagation direction in the FWH equation was the normal vector of each of panel on the integration surface. Since the spanwise extents of the main element were symmetry planes, not walls, there was no propagation from the main element in this plane. However, the integration surface at the flap side-edge clearly had normal vectors in the $x-z$ plane and was thus responsible for all the sound radiated in this plane. The directivity showed that slightly downstream there was more sound radiated. This was due to significant regions of flow unsteadiness near the trailing-edge of the flap. The directivity was compared to that of a cardioid directivity pattern, which

is given by,

$$SPL \propto \sin^2(\theta/2) \; . \tag{8.4}$$

This was the directivity of a vortex line around a semi-infinite half plane as derived by Crighton [86]. The directivity of the flap side-edge was approximately that of a cardioid but differed, especially upstream and downstream due to the finite thickness of the flap and the non-uniform loading on the flap.

8.3 Porous Side-Edge Simulation

A computation was carried out with a porous boundary condition at the flap side-edge to determine the nearfield flow changes arising from the transpiration velocity through the porous material. This computation was related to the experimental results with the porous side-edge in Chapter 5. Changes in the nearfield flow could be used to potentially determine the effect of the porous flap side-edge on the acoustic sources. As mentioned in Chapter 7, the porous boundary condition was modelled as a source term in the momentum equation.

The results for the pressure and x vorticity at a plane $x_F/c_F = 0.4$ are shown in Figures 8.30 and 8.31 respectively. The results showed that with the porous side-edge treatment, the vortex was significantly weaker than for the hardwall case. The pressure and x vorticity at $x_F/c_F = 0.9$ are shown in Figures 8.32 and 8.33 respectively. As the trailing-edge was approached, the vortex had moved inboard from the side-edge and also further away from the surface. The point of maximum x vorticity in the vortex core was 0.035 m above the flap surface at $x_F/c_F = 0.9$ for the hardwall case. With the porous side-edge treatment applied this point was 0.06 m above the flap surface. The difference in the vortex location between the hardwall and porous side-edge corresponded to a vertical displacement of approximately $y/t_F = 1.2$. This was due to the momentum flux passing through the porous material. The displacement in the computational solution closely matched the experimental PIV measurements in Chapter 5.

Figure 8.34 shows the non-dimensionalised transpiration velocity through the porous side-edge in the y direction. This corresponded to the vertical velocity, which was responsible for the displacement effect. The largest region of transpiration velocity was from $x_F/c_F = 0.4$ to $x_F/c_F = 0.8$. This region of the porous material had the largest pressure difference across it due to the low pressure vortex core above the suction surface.

Pressure distributions over the chord of the flap with the porous treatment are shown at various spanwise locations in Figure 8.35. The porous side-edge treatment was applied over 4% of the span of the flap. The pressure distribution on the porous material was at $z/b_f = 0.027$. The loading on the porous edge was small due to the leaking of flow from

the pressure surface to the suction surface. The pressure difference supported across the porous side-edge was proportional to the velocity through the material. The peak loading on the porous flap side-edge was at $x_F/c_F = 0.6$. This was caused by the low pressure in the vortex core which induced a greater velocity through the porous side-edge from the pressure surface to the suction surface.

The second pressure distribution was at $z/b_F = 0.078$. The hardwall pressure distribution in Figure 8.18 showed a strong peak in the pressure distribution due to the low pressure in the strong vortex core. The main effect of the porous side-edge was to reduce the vortex core strength. The porous pressure distribution had a much reduced peak and was spread further over the chord of the flap. At $z/b_F = 0.242$, the pressure peak at the leading edge of the flap was apparent. The weak side-edge vortex influenced the pressure distribution near the trailing-edge. Compared to the hardwall case, the pressure peak that corresponded to the side-edge vortex was much reduced.

The spanwise pressure distributions of the flap with a porous side-edge is shown in Figure 8.36. Near the leading-edge, the influence of the side-edge vortex is minimal, similar to the hardwall case. Near the mid-chord, the strongest influence of the side-edge vortex was seen, although it was significantly weaker than the hardwall case.

8.4 Summary

The three-dimensional solution outlined in this chapter captured all of the major physics and flow phenomenon outlined in the literature review and found during the experimental investigation presented in Chapter 4. However, previous computational work had not captured the unsteadiness that was present in the flap side-edge vortex. Sources of unsteadiness have been obtained by examining contours of pressure perturbation, which showed sources of unsteadiness at the main vortex, the shear layer, the cove region and the main element wake. A FWH solver was used to obtain the farfield directivity and to evaluate the strength of on-surface acoustic sources. The effect of the porous flap side-edge was to reduce the magnitude of vorticity in the vortex significantly. It also had the effect of displacing the vortex core further away from the flap surface. There was no evidence of vortex bursting at a flap deflection angle of 29 degrees.

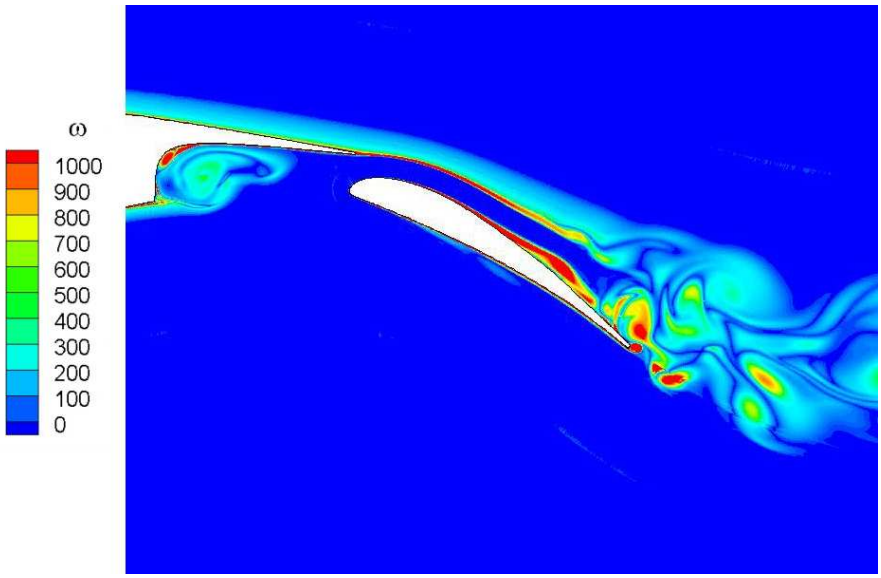

FIGURE 8.1: Vorticity magnitude contours in symmetry plane.

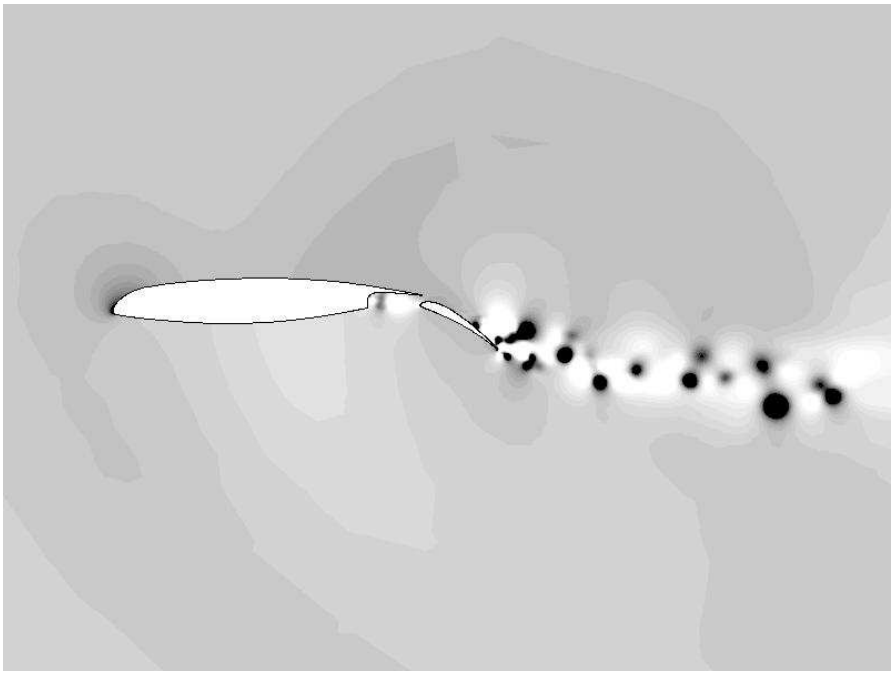

FIGURE 8.2: Pressure perturbations in symmetry plane.

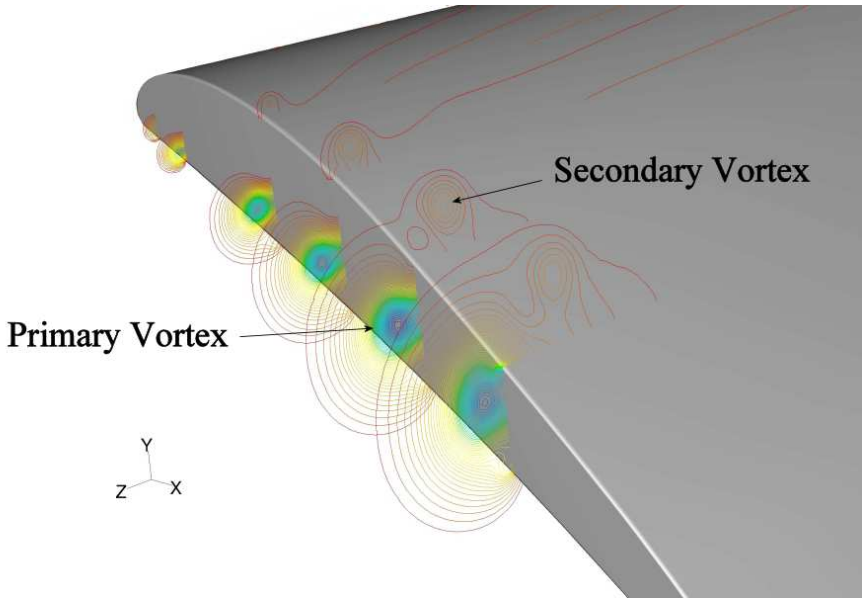

FIGURE 8.3: Coefficient of pressure contours close to flap leading-edge showing presence of dual vortex system.

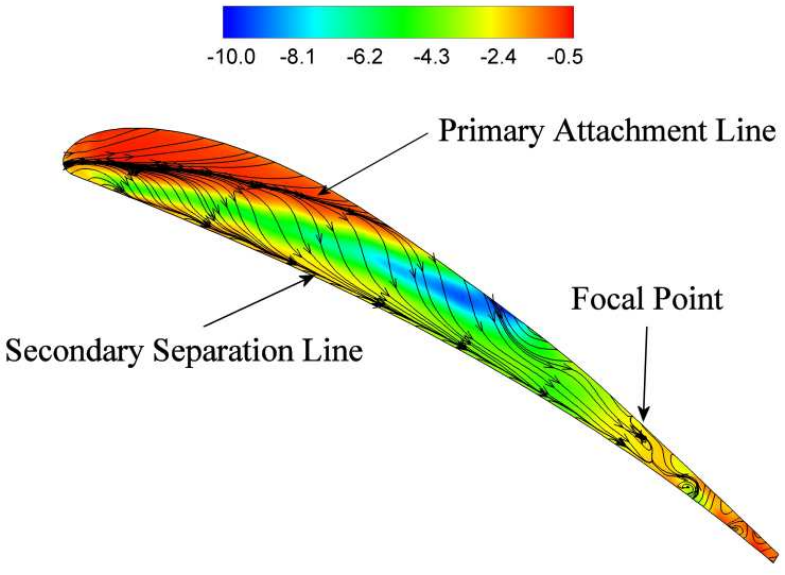

FIGURE 8.4: Near surface streamlines showing major on-surface flow features with contours of pressure coefficient.

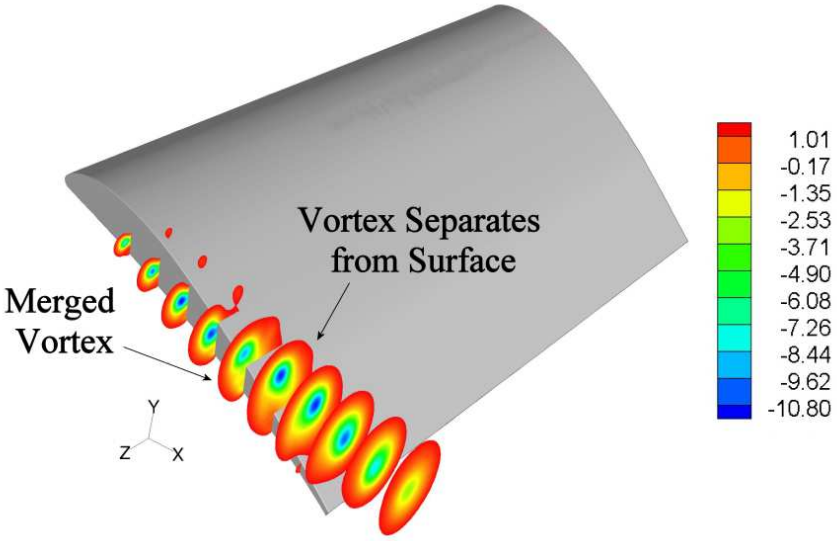

FIGURE 8.5: Coefficient of pressure contours in a series of $y - z$ planes showing vortex merging and separation of vortex from flap.

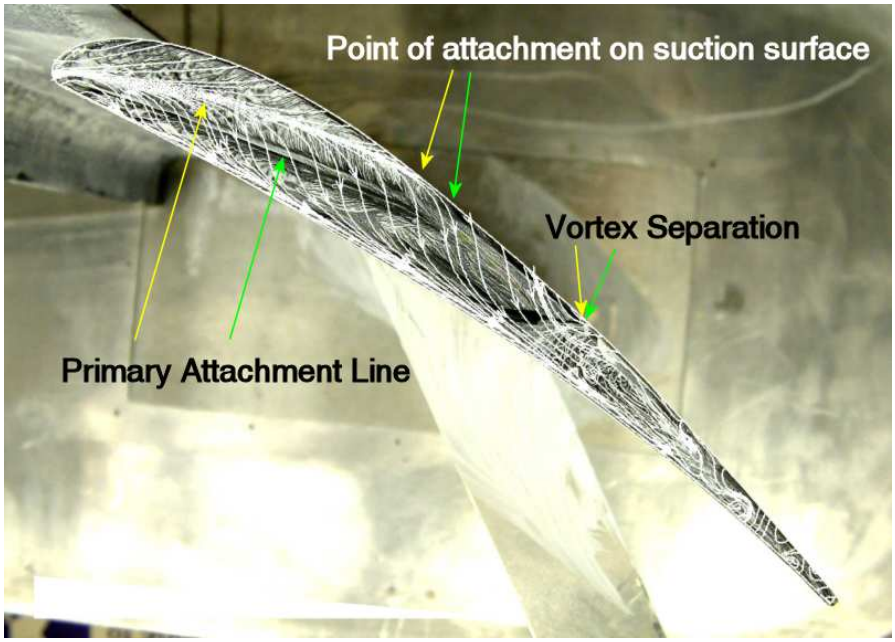

FIGURE 8.6: Overlay of oil flow and detached eddy simulation result showing the flap side-edge flowfield. (Computational features are shown with yellow arrows while experimental features are shown with green arrows.)

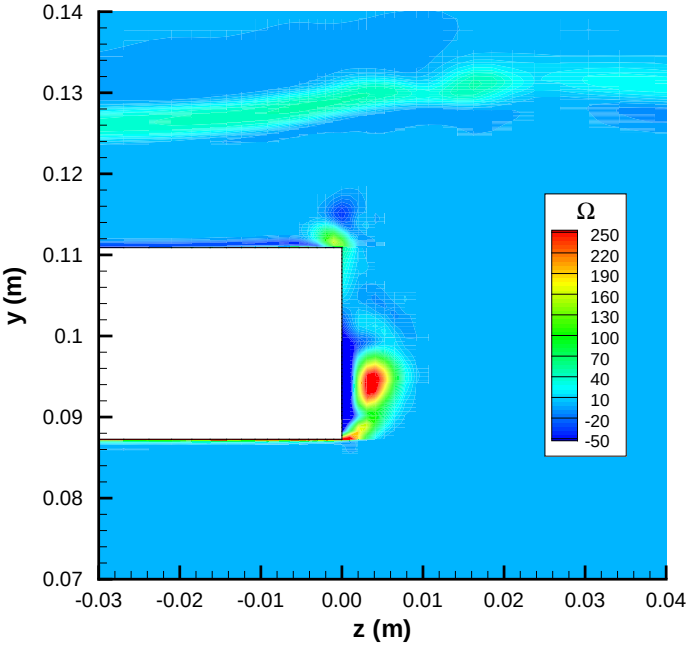

FIGURE 8.7: Contours of x vorticity in $y-z$ plane at $x_F/c_F = 0.2$.

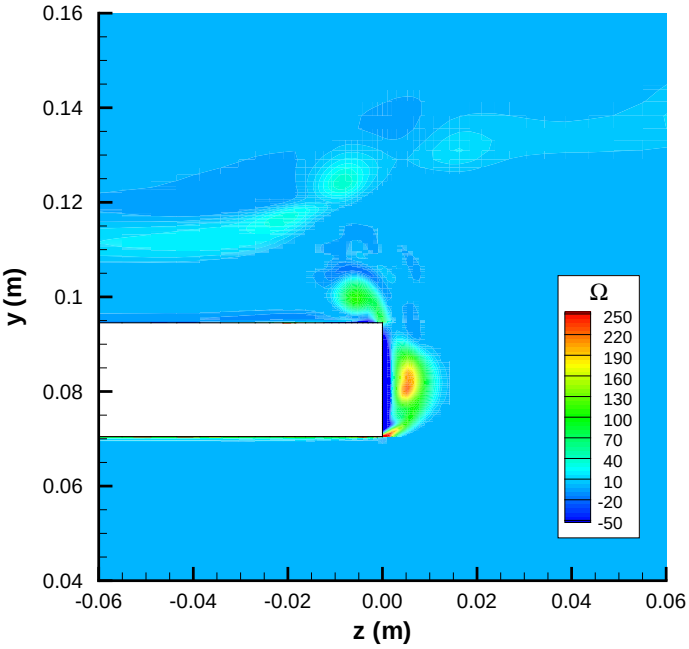

FIGURE 8.8: Contours of x vorticity in $y-z$ plane at $x_F/c_F = 0.4$.

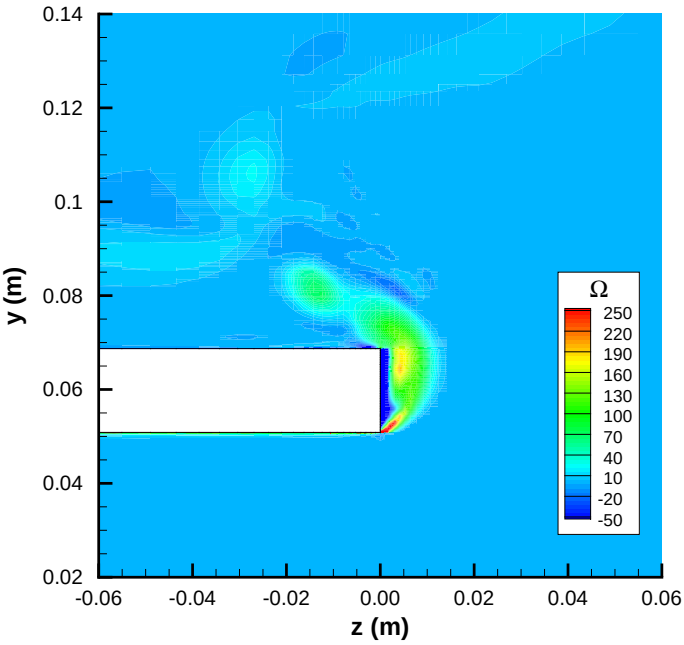

FIGURE 8.9: Contours of x vorticity in $y-z$ plane at $x_F/c_F = 0.6$.

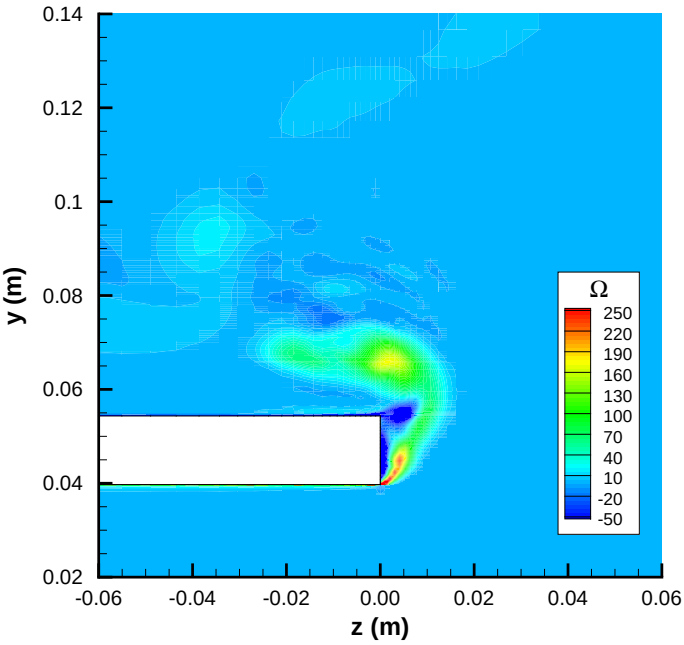

FIGURE 8.10: Contours of x vorticity in $y-z$ plane at $x_F/c_F = 0.7$.

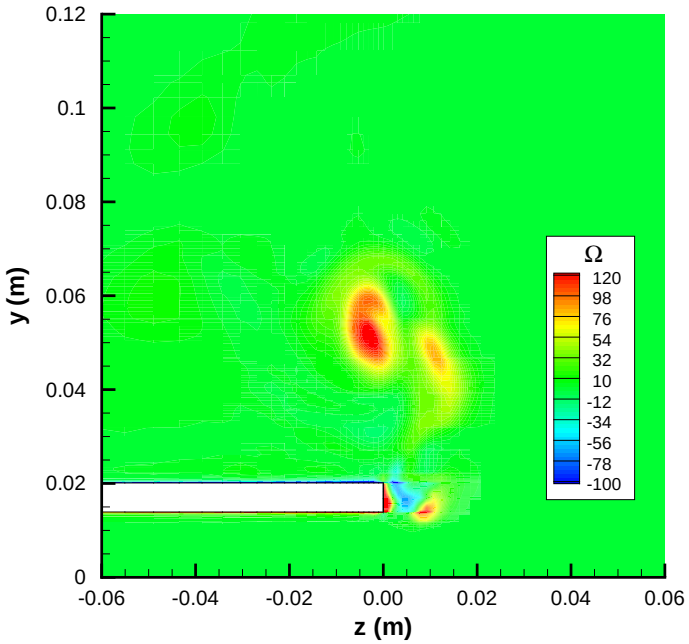

FIGURE 8.11: Contours of x vorticity in $y-z$ plane at $x_F/c_F = 0.9$.

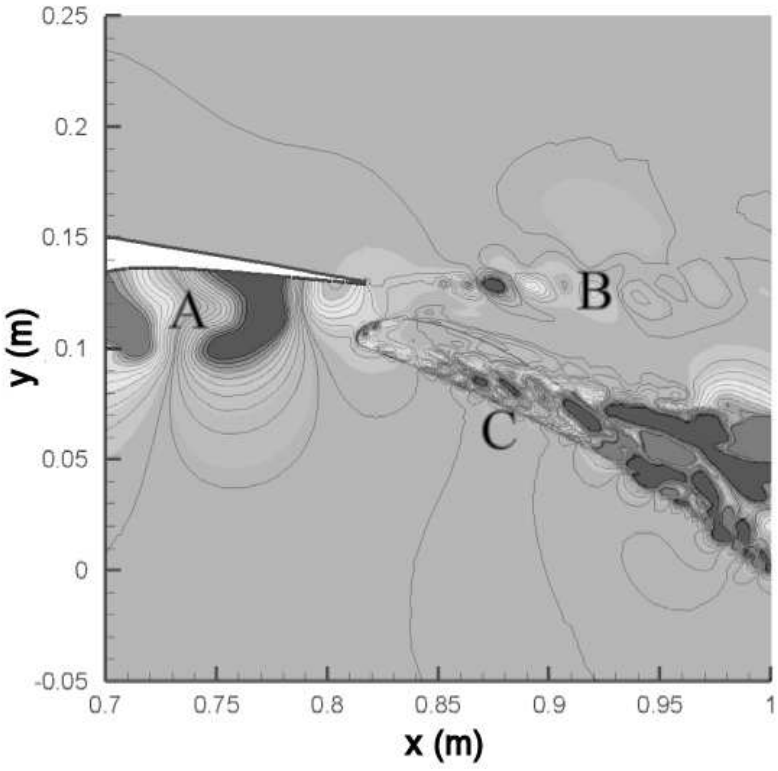

FIGURE 8.12: Pressure perturbations in $x-y$ plane at flap side-edge ($z = 0$).

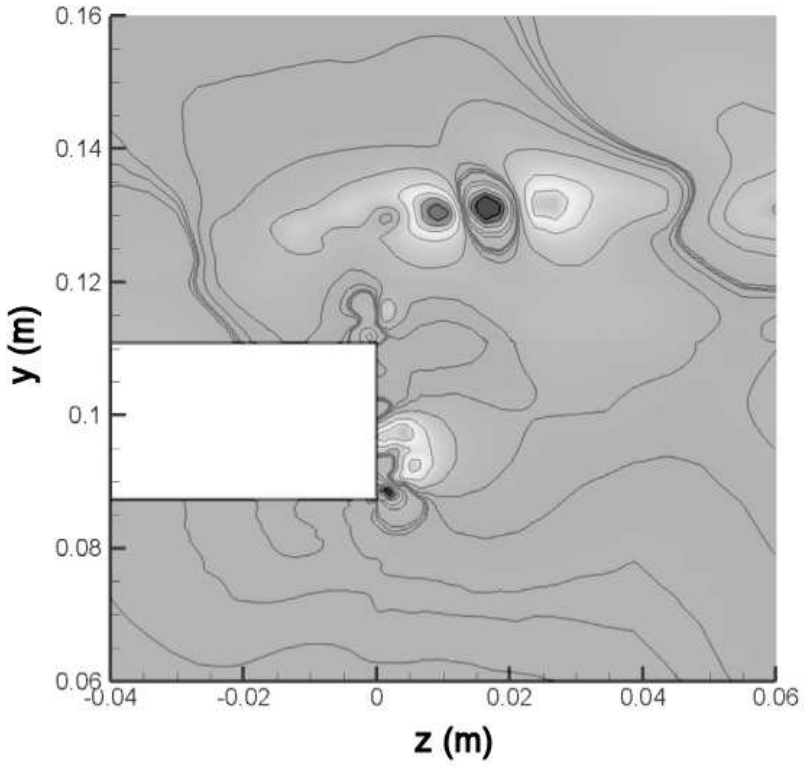

FIGURE 8.13: Pressure perturbations in $y - z$ plane at $x_F/c_F = 0.2$.

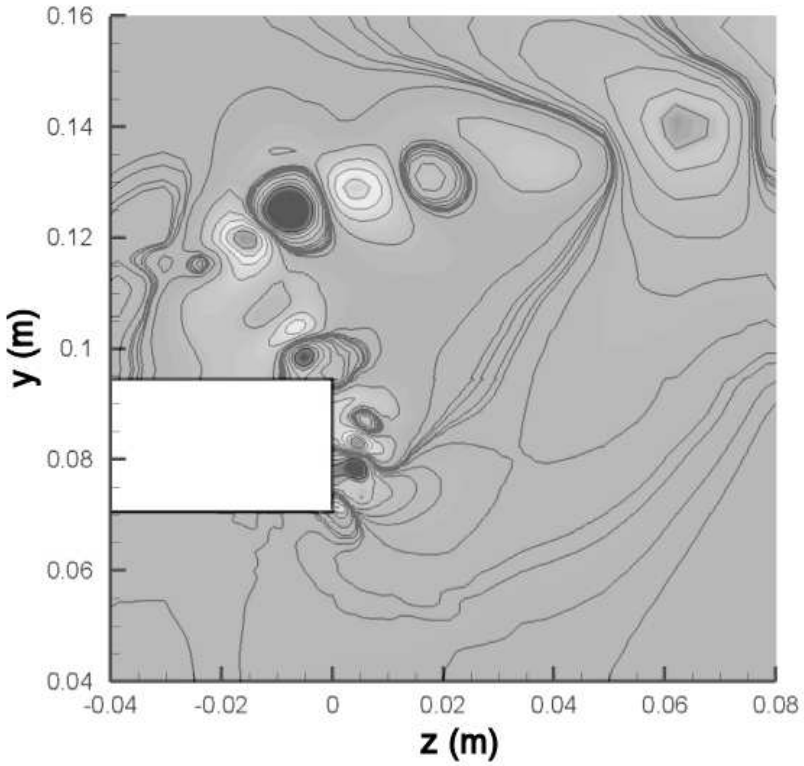

FIGURE 8.14: Pressure perturbations in $y - z$ plane at $x_F/c_F = 0.4$.

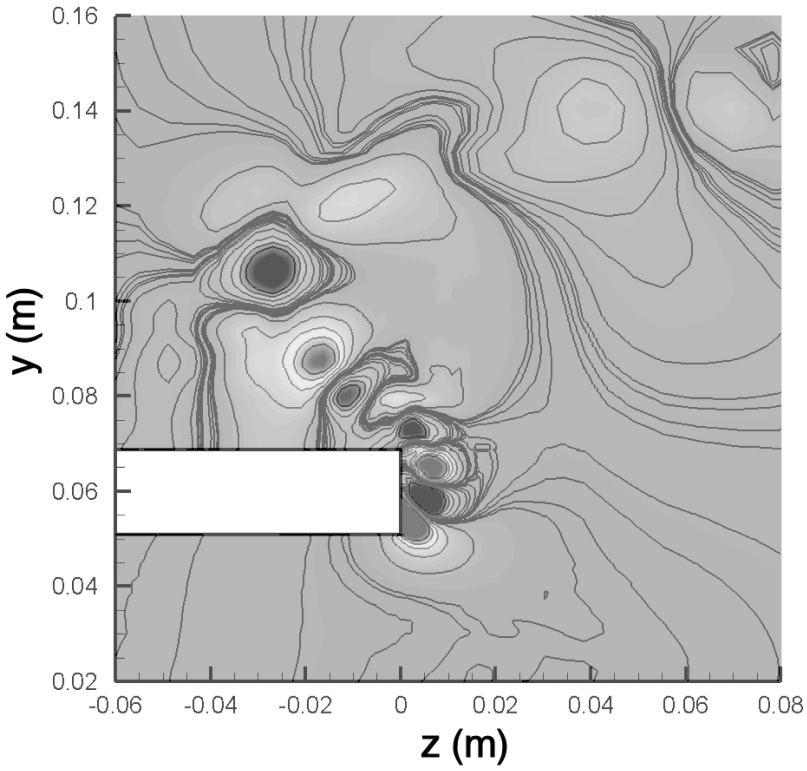

FIGURE 8.15: Pressure perturbations in $y - z$ plane at $x_F/c_F = 0.6$.

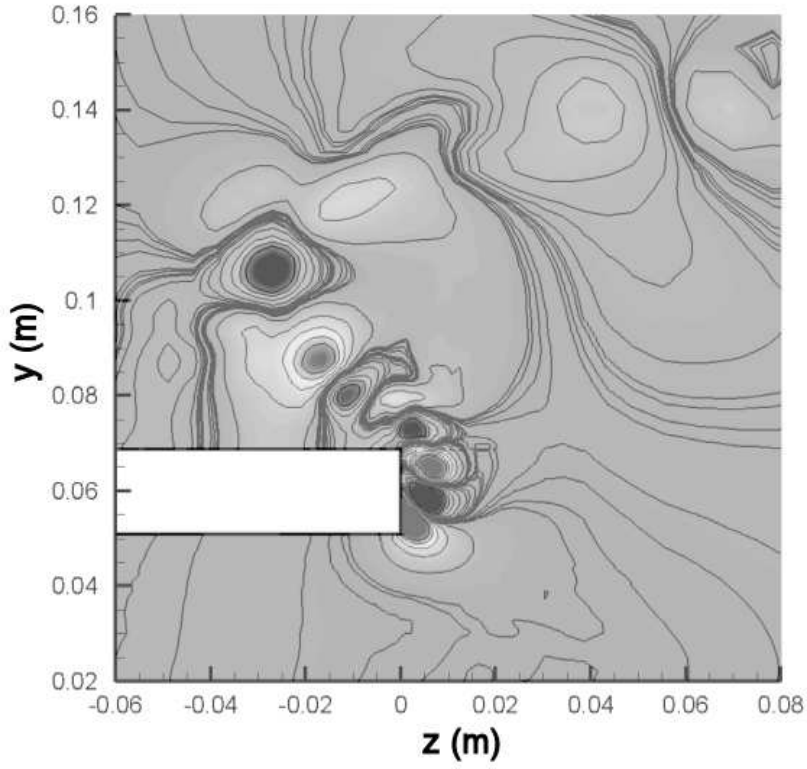

FIGURE 8.16: Pressure perturbations in $y - z$ plane at $x_F/c_F = 0.7$.

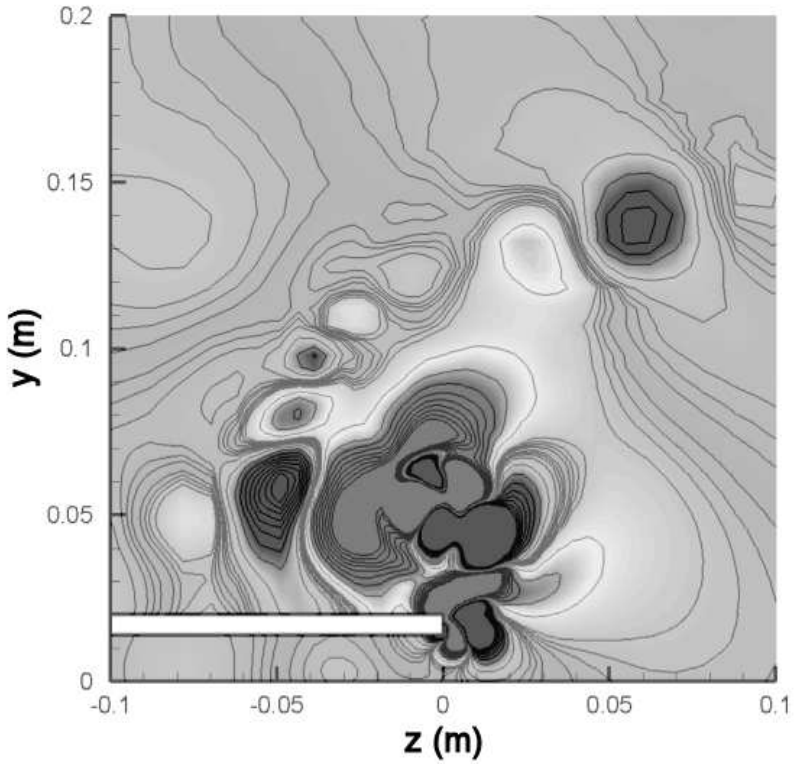

FIGURE 8.17: Pressure perturbations in $y - z$ plane at $x_F/c_F = 0.9$.

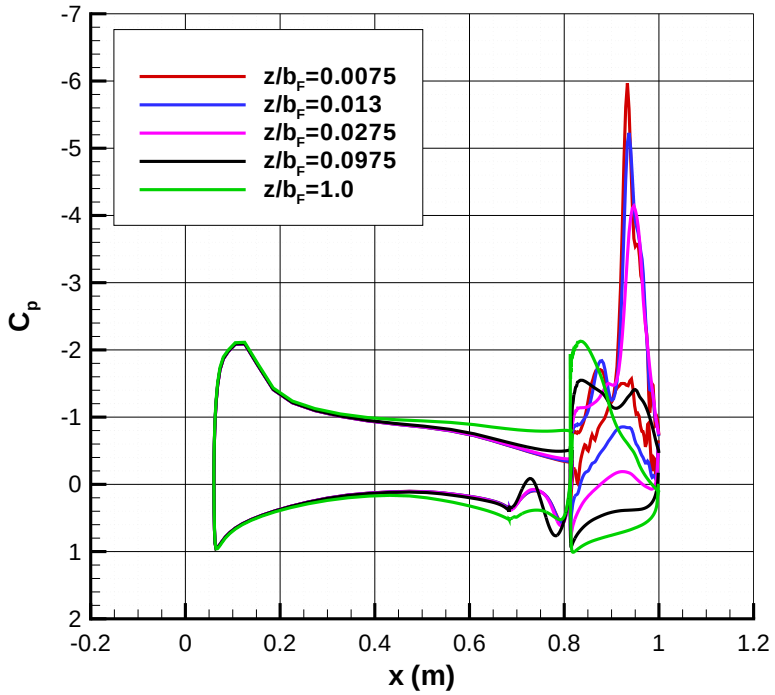

FIGURE 8.18: Pressure distributions on flap at five spanwise locations.

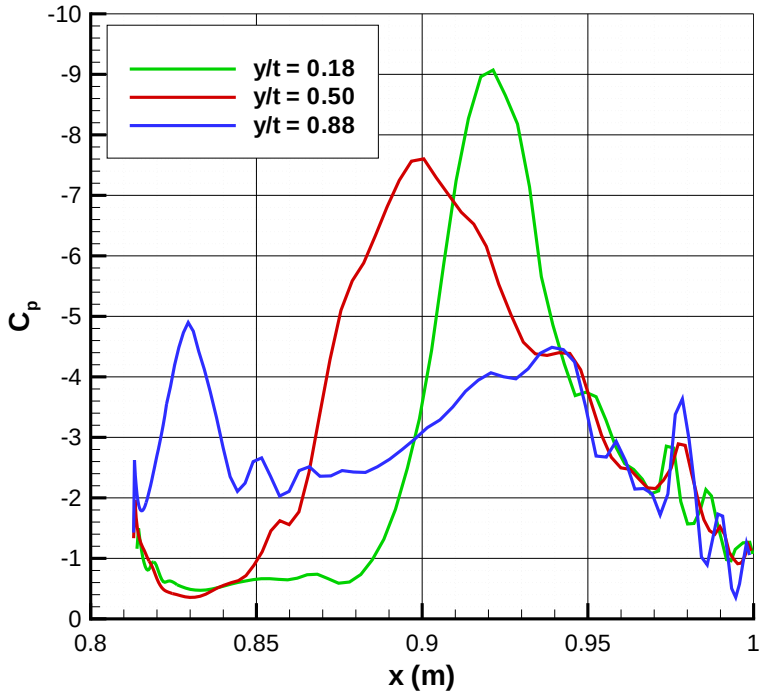

FIGURE 8.19: Three pressure distributions along the flap side-edge.

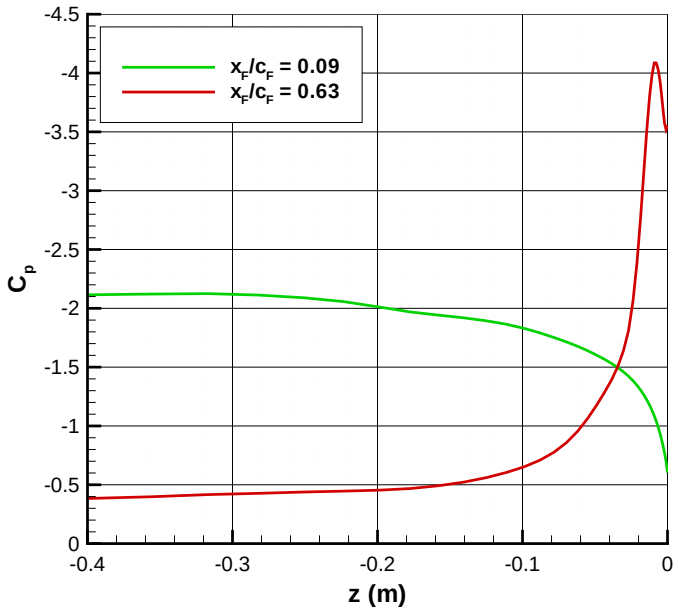

FIGURE 8.20: Spanwise pressure distributions on flap.

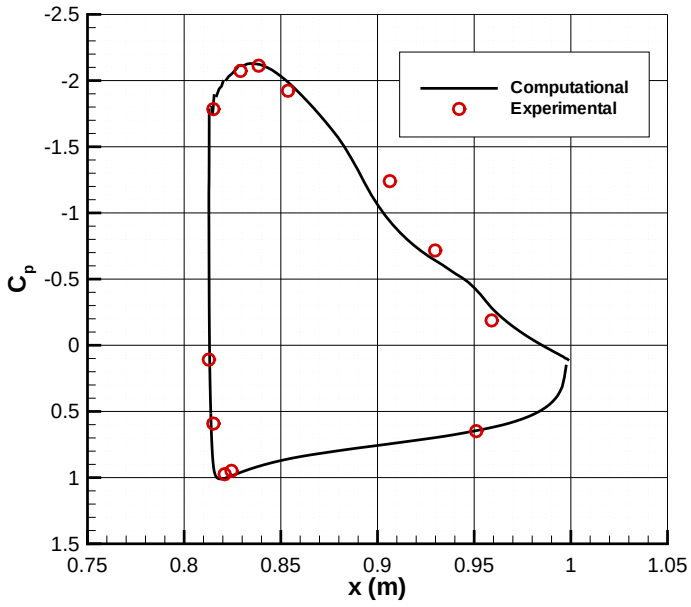

FIGURE 8.21: Comparison of experimental and computational chordwise pressure distributions at $z = 0.25$ m.

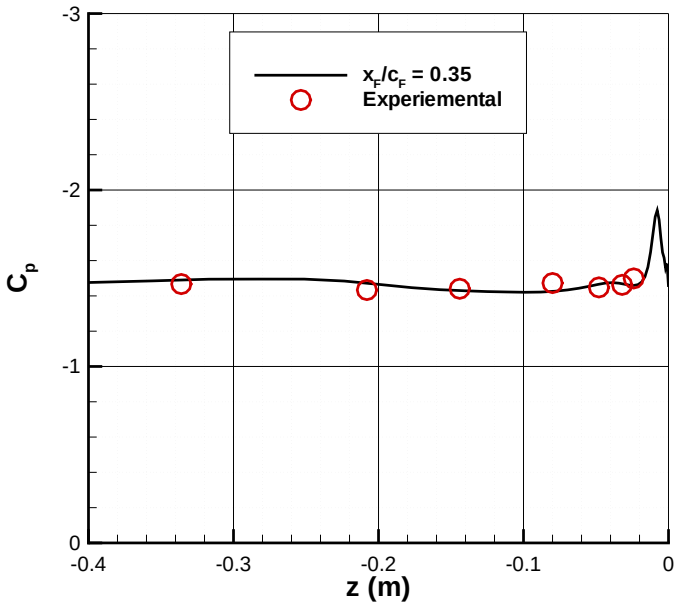

FIGURE 8.22: Comparison of experimental and computational spanwise pressure distributions at $x_F/c_F = 0.35$.

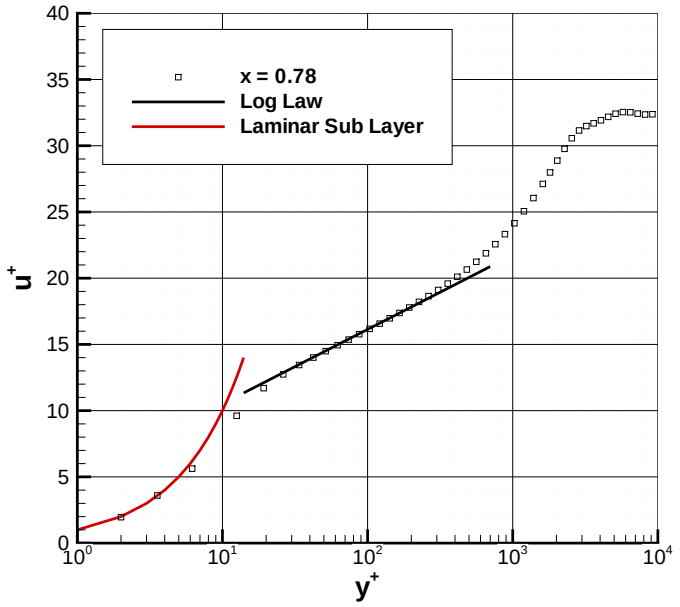

FIGURE 8.23: Comparison of boundary layer profile at $x = 0.78$ with log law.

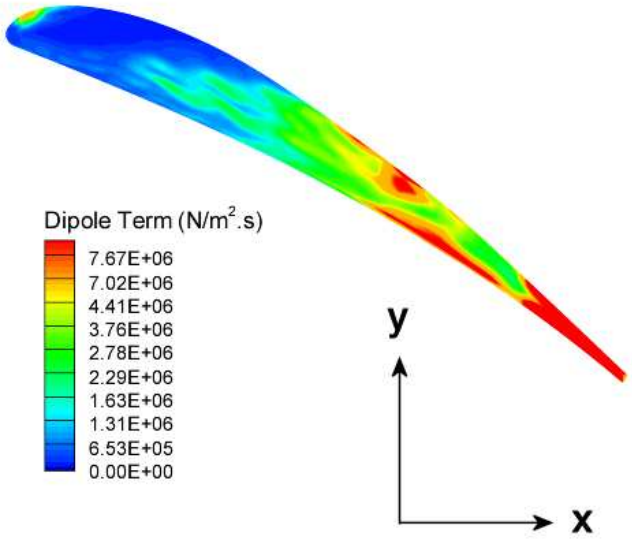

FIGURE 8.24: Magnitude of dipole source term on flap side-edge.

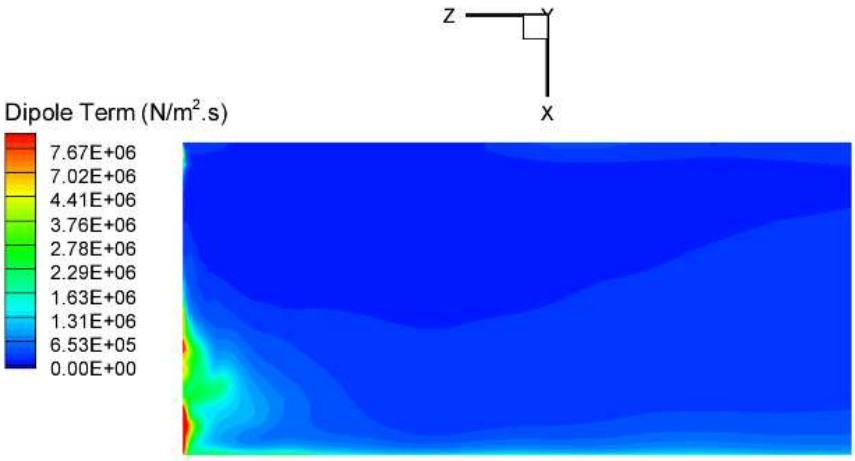

FIGURE 8.25: Magnitude of dipole source term on flap suction surface.

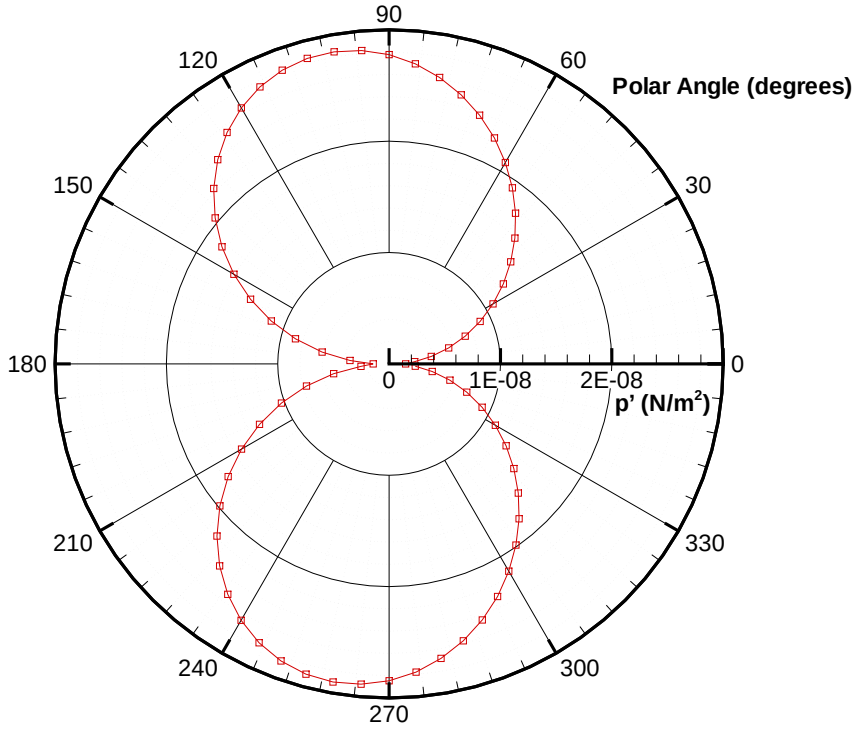

FIGURE 8.26: Farfield directivity at $r = 100$ m in $x - y$ plane from main element.

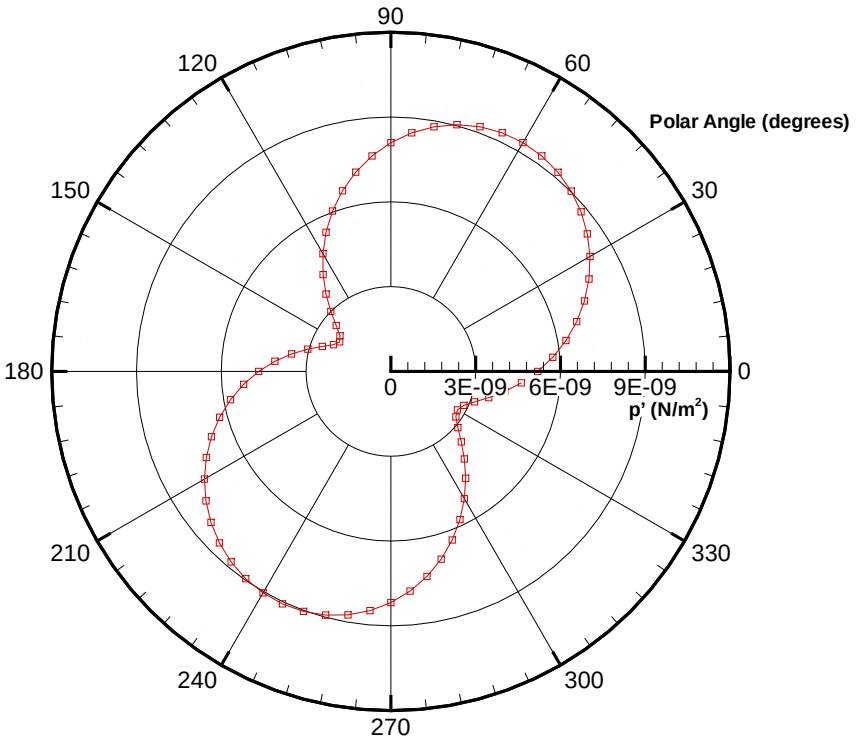

FIGURE 8.27: Farfield directivity at $r = 100$ m in $x - y$ plane from flap.

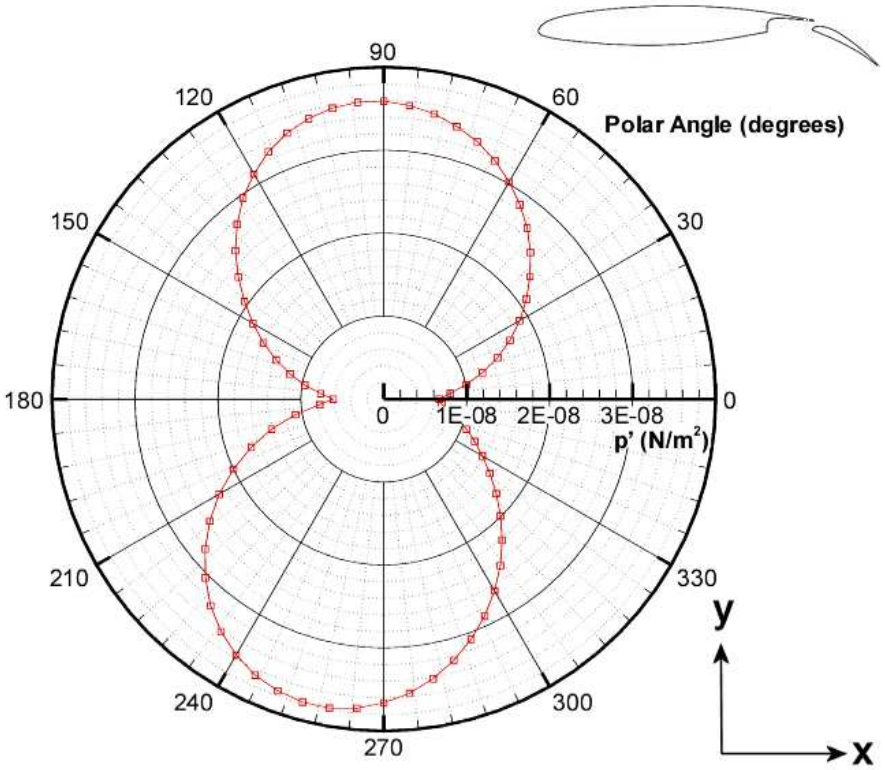

FIGURE 8.28: Combined farfield directivity at $r = 100$ m in $x - y$ plane.

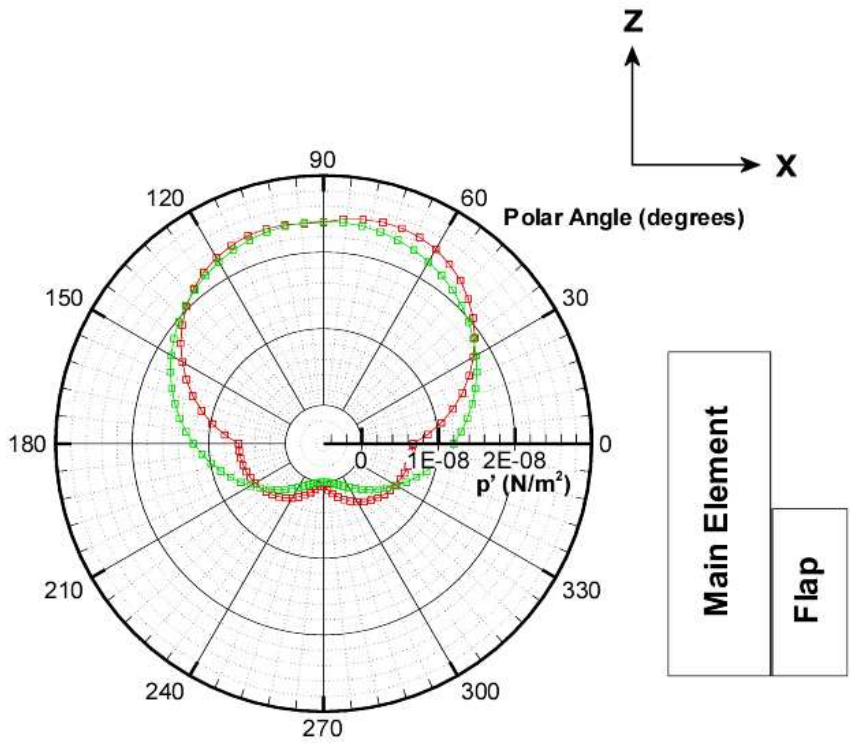

FIGURE 8.29: Farfield directivity at $r = 100$ m in $x - z$ plane.

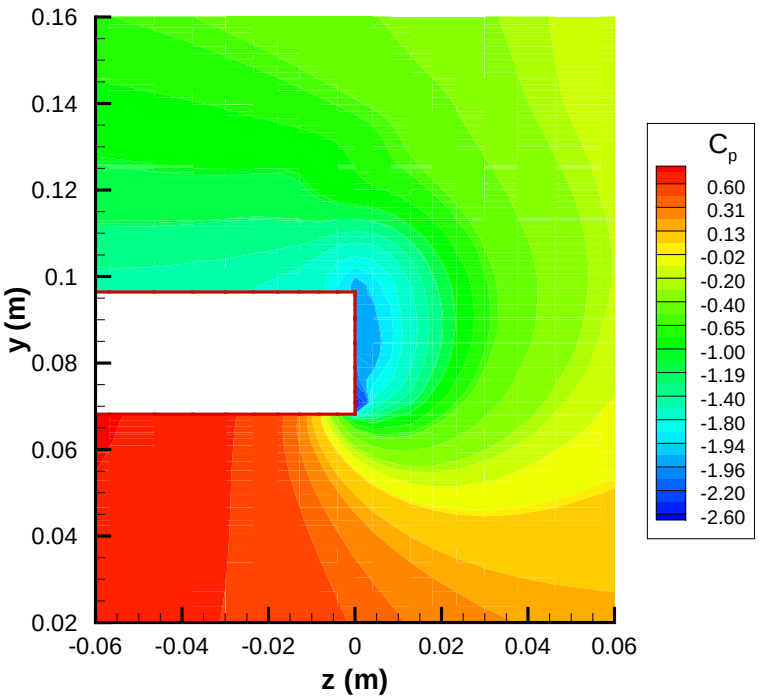

FIGURE 8.30: Pressure contours at $x/c_F = 0.4$ with porous treatment.

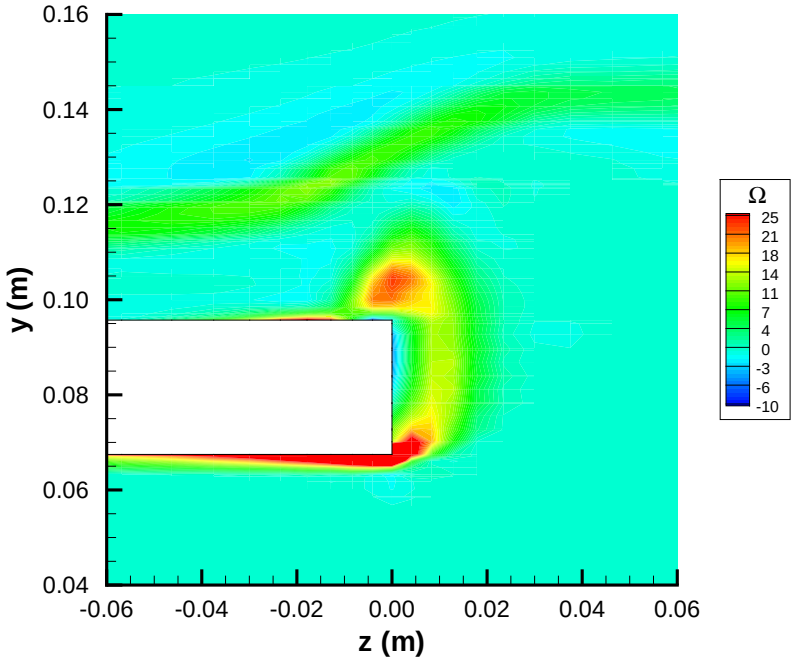

FIGURE 8.31: x vorticity contours at $x/c_F = 0.4$ with porous treatment.

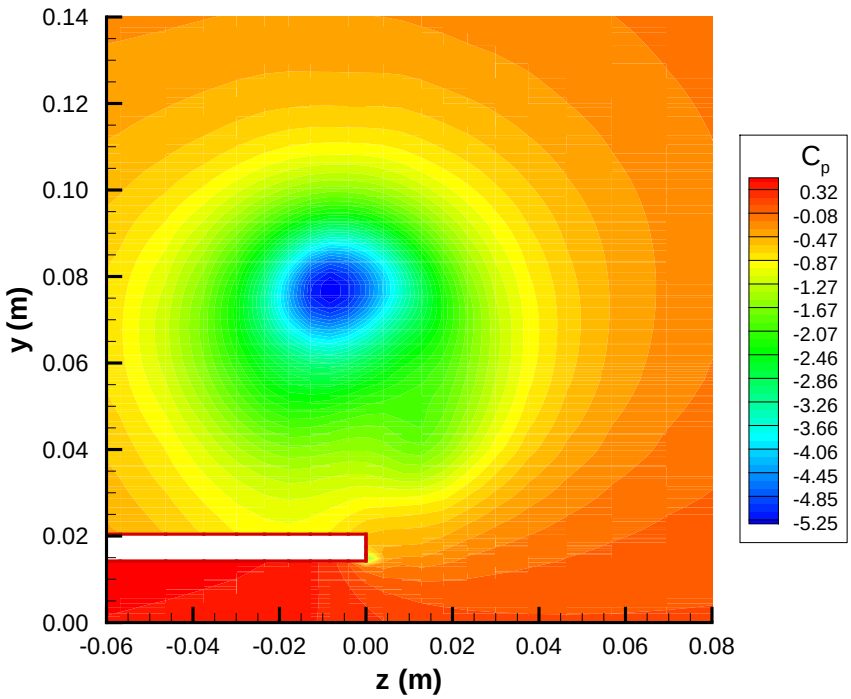

FIGURE 8.32: Pressure contours at $x/c_F = 0.9$ with porous treatment.

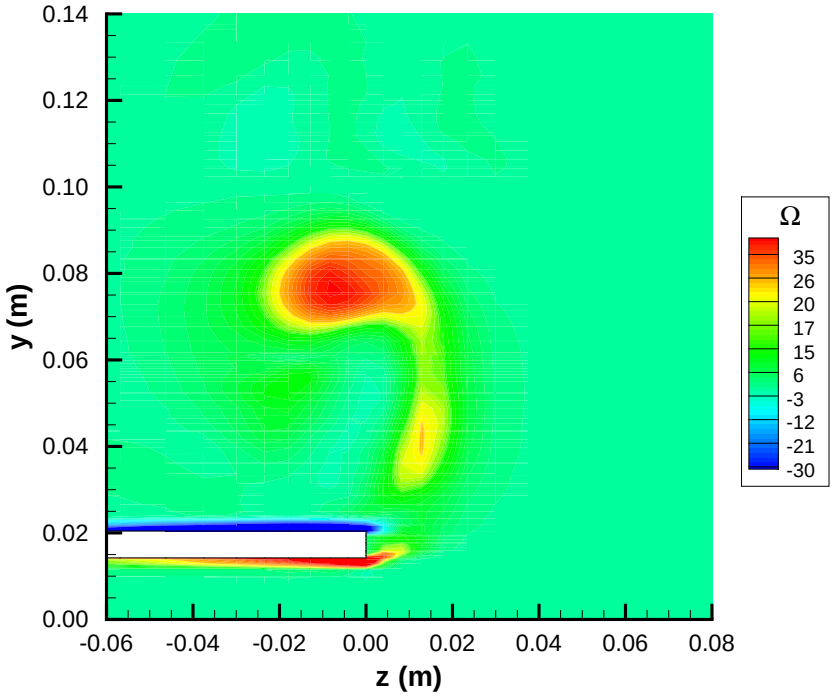

FIGURE 8.33: x vorticity contours at $x/c_F = 0.9$ with porous treatment.

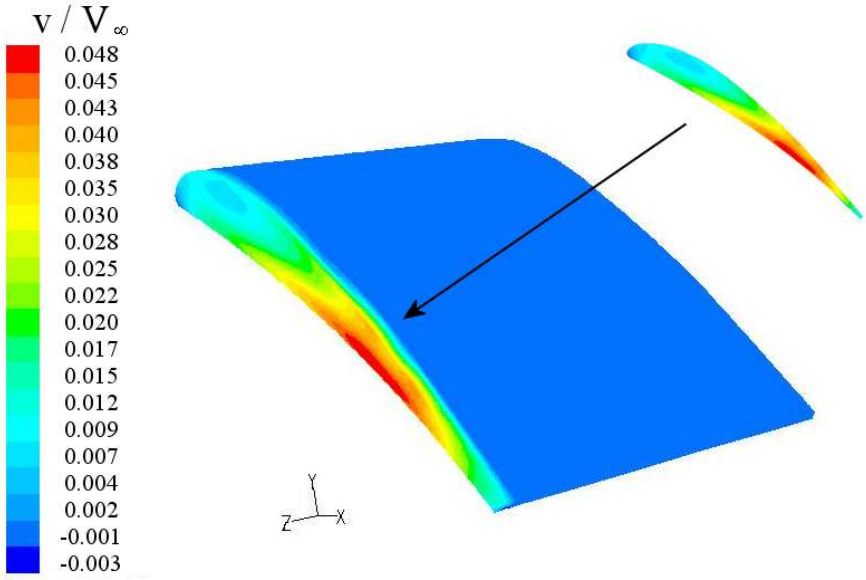

FIGURE 8.34: Non-dimensionalised y transpiration velocity through the porous flap side-edge.

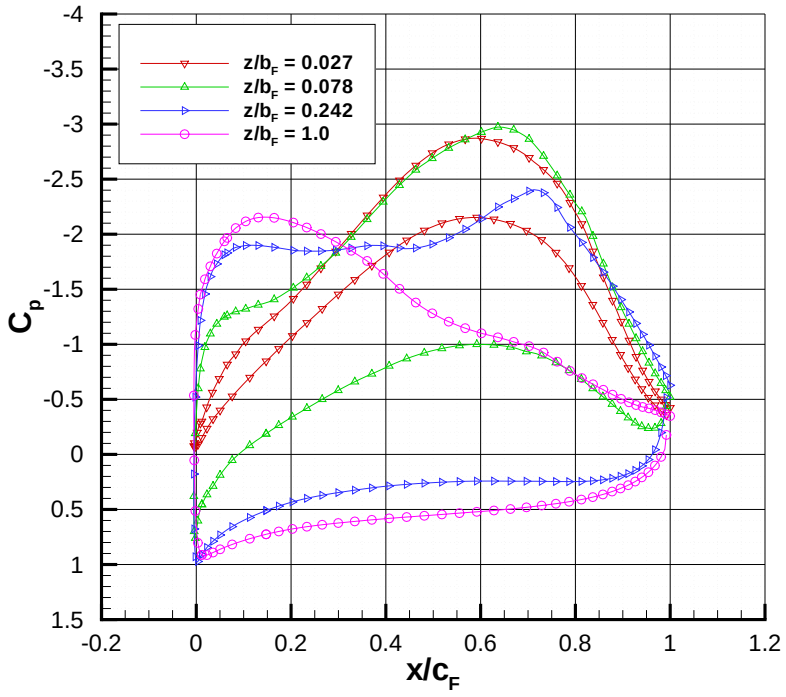

FIGURE 8.35: Pressure distributions on the flap with a porous side-edge.

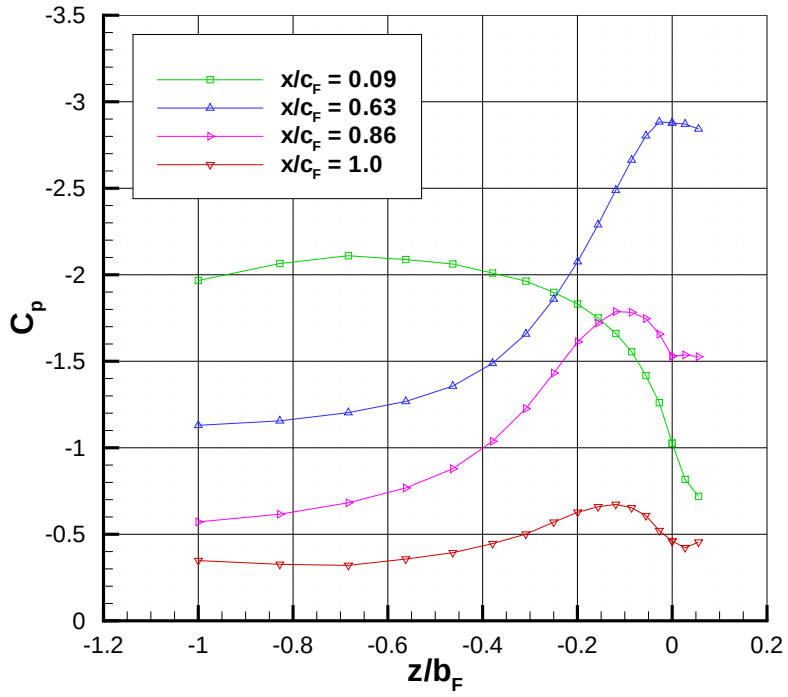

FIGURE 8.36: Spanwise pressure distributions on the flap with a porous side-edge.

Chapter 9

Conclusions and Recommendations

9.1 Summary

An experimental and computational investigation was carried out to determine the aerodynamics and aeroacoustics of the flowfield around a flap side-edge. The aim of the research was to understand the mechanisms responsible for the noise generation at the flap side-edge. A porous material was applied to the flap side-edge in an attempt to reduce the noise generated by the flap. The changes in the flowfield with the application of a porous side-edge were determined by means of various experimental measurements.

9.2 Hardwall

The aerodynamic properties of a high lift wing equipped with a half span flap were determined by means of on-surface pressures and by measuring forces and moments. PIV was used to examine the formation of the flap side-edge vortex with both a solid side-edge and a porous side-edge. Oil flow visualisation was performed in conjunction with the PIV to determine the nearfield flow. From the flow visualisation and PIV measurements three potential noise sources were proposed at the flap side-edge. Firstly, near the leading edge, the turbulent shear layer that separated from the pressure surface of the flap, attached to the side-edge. An on-surface, flush mounted microphone was placed at this attachment point to measure the unsteadiness caused by the impingement of the turbulent shear layer. Secondly, near the mid-chord of the flap, the dual vortex system on the flap side-edge had merged to become a single vortex. The attachment point of the turbulent shear layer now moved onto the suction surface. Thirdly, as the trailing edge was approached, the vortex was located off-surface above the flap side-edge. The

vortex exhibited a low frequency instability due to unsteady flow originating upstream of this point. This caused pressure perturbations from the unsteady vortex to interact with the sharp flap side-edge and trailing edge.

From the hotwire measurements, the vortex downstream of the flap exhibited low frequency instabilities centered around a Strouhal number based on flap chord (St_F) of 9.3. This corresponded to the on-surface microphone measurements in the cove region of the main element where a similar frequency was measured at the same airspeed. This suggested that the low frequency instabilities in the downstream vortex were dominated by unsteadiness originating upstream of the flap. The spectra also demonstrated mid frequency features between 2 kHz ($St_F = 20$) and 5 kHz ($St_F = 50$), which became slightly more prominent as the freestream velocity increased. These frequencies matched those measured by the on-surface microphone at the flap side-edge. The origin of these instabilities was shed turbulence from the flap side-edge.

Although the mid frequency disturbances were small as measured by the hotwire far downstream, they dominated the nearfield. The on-surface microphone, located at the primary vortex attachment line, showed a broadband hump between 2000 Hz and 7000 Hz depending on airspeed and flap deflection angle. The effect of increasing the flap deflection angle was to decrease the magnitude of these disturbances, since the vortex separated from the flap surface further upstream. Therefore, for the 39 degree flap deflection case the vortex was already off-surface and therefore the shed turbulence was moved further away from the on- surface microphone.

A detached eddy simulation was carried out on a flap side-edge to resolve the unsteady flow around this geometry with a grid of 4.7×10^6 nodes. The simulation allowed the identification of sources of unsteadiness in the flow around the flap side-edge. Away from the influence of the flap side-edge vortex, the flowfield showed three sources of vorticity that interacted to form a significant unsteady flow above the flap suction surface. A shear layer separated from the main element flap cove and induced an unsteady flow in the cove. There was vorticity generated in the separated flow region on the flap suction surface. This interacted with the vorticity convected from the trailing-edge of the main element to form a significantly unsteady wake that was convected downstream.

The pressure perturbations in a plane at the flap side-edge, showed an additional source of unsteadiness in the flap side-edge vortex. The primary vortex on the flap side-edge showed significant unsteadiness. The secondary vortex on the flap suction surface, which was weaker, showed less unsteadiness. The amplitude of these disturbances were magnified as the vortex grew in strength and separated from the flap surface. The main element trailing-edge wake was deflected towards the flap suction surface due to the induced flowfield around the flap side-edge vortex. The effect of bringing this unsteadiness

closer to the flap surface had an adverse effect on the aeroacoustic performance of the flap.

The detached eddy simulation captured the major flow features at the flap side-edge found in the experimental study of Chapter 4, i.e. a dual vortex system near the leading-edge, vortex merging and a significantly unsteady off-surface vortex. Compared to the experimental on-surface oil flow visualisation, the detached eddy simulation overestimated the magnitude and growth rate of the primary vortex on the flap side-edge. The point of separation of the vortex from the flap surface was well predicted by the detached eddy simulation. The chordwise and spanwise pressure distribution on the flap were well predicted when compared to the experimental data. The boundary layer profile on the main element was compared to the log law, which showed the boundary layer was adequately resolved in the log law region from $30 < y^+ < 300$.

A Ffowcs-Williams Hawkings solution was performed using the CFD data as an input to obtain the farfield acoustics. The magnitude of the dipole source term was plotted on the flap surface. The major sources were on the flap side-edge on the primary attachment line and beneath the point where the unsteady vortex separated from the surface. There was also a source on the leading edge, which was due to unsteady pressures in the cove that impinged on the flap surface. On the suction surface of the flap, the major source was beneath the separated vortex.

9.3 Porous Side-Edge Effect

Three porous side-edges were applied to the flap with varying degrees of porosity. The experimental force measurements showed a diminutive reduction in lift, i.e. less than 0.5% of C_L at 20 degrees angle of attack. The least permeable of the side-edges (40 PPI 10-12%) had the least reduction in lift. There was a slight increase in the drag associated with the use of a porous side-edge. This was due to the pressure loss of the flow through the porous material that resulted in a net force contributing to drag.

The particle image velocimetry measurements demonstrated the two effects of applying a porous material to the flap side-edge:

1. Reduced strength of vorticity in the flowfield around the flap side-edge.
2. Displacement of the vortex further away from the flap surface.

The most permeable material of 20 PPI 5-7% resulted in the most significant reduction in the strength of the shear layer wrapped around the vortex. The porous treatment at a relative density of 5-7% also resulted in the most displacement of the vortical structure

away from the flap suction surface. The displacement with this porous edge treatment was 50% greater than the hardwall case. The reduction in vorticity was due to relieving some of the pressure differential between the suction and pressure surfaces, which resulted in a weaker vortex. The weaker vortex led to less induced velocities around it. This reduced the strength of vorticity in the shear layer that fed the vortex and which was one of the causes for instabilities in the vortex in the detached eddy simulation.

The hotwire anemometry showed that with the application of a porous side-edge there were increased levels of turbulence in the wake downstream of the model. It was hypothesised that this was due to turbulence generation caused by the flow through the porous material interacting with the structure of the porous material. The hotwire measurements showed that the higher spectra levels in the farfield wake were associated with smaller characteristic pore dimensions. Spectra taken in the vortex core showed a broadband hump centered at a Strouhal number based on flap chord of 70.

The microphone measurements taken on the port endplate also showed this broadband hump at $St_F = 70$ with the porous side-edge treatment applied. The dominant feature for the hardwall case was a broadband hump centered around 4 kHz ($St_F = 40$). This shift in frequency with the application of porous materials was similar to that found by other authors. The major effect of applying the porous side-edge on the acoustic field measured by the microphone on the flap side-edge, was a large reduction in the mid-frequencies. This was caused by reducing the vortex strength and the strength of the shear layer wrapped around it. This lessened the interaction between the two and the magnitude of the hydrodynamic instabilities. Also by displacing these disturbances further from the surface, further reductions in the noise generated by the flap side-edge were achieved.

9.4 Split Flap

The flow with a split flap configuration was characterised by a high speed flow through the gap between the trailing-edge of the main element and the deflected portion of the flap. This caused a strong shear layer, of opposite sign vorticity to that of the side-edge vortex, to separate from the main element trailing-edge. The secondary vortex on the top surface was flattened due to the jet like flow through the gap. The spectra levels at a flap deflection angle of 29 degrees were lower than the baseline hardwall configuration. This was due to a constrained gap between the main element and the flap, which restricted the flow around the flap side-edge as shown in Figure 6.4. As the flap deflection angle was increased to 39 degrees this gap increased and allowed a high speed flow through the gap and the vortex to form. This resulted in higher sound pressure levels compared to the baseline hardwall results.

The effect of applying a porous side-edge to the split flap configuration resulted in lower sound pressure levels measured at the flap side-edge. It was hypothesised that this was caused by impeding the air as it passed through the gap due to the nature of the porous material. This impedance reduced the jet effect through the gap and also resulted in the formation of a weaker vortex on the suction surface.

9.5 Recommendations

This section discusses briefly some other potential noise reducing technologies that could be applied to the flap side-edge region. One of the ways the porous material reduced the strength of the acoustic source at the flap side-edge was by displacing the unsteady vortical structure away from the surface. Another way to achieve the same effect is to use blowing at the flap side-edge to displace the vortex. Mid frequency noise was produced by the impingement of the turbulent shear layer on the side-edge and suction surface of the flap. This noise was scattered by the sharp edges present in the vicinity of the flap. The use of fences at the flap side-edge could be used to delay the point of vortex merging and to displace the turbulent shear layers away from the flap surface. The presence of sharp edges at the flap side-edge should be avoided. Serrated or rounded flap side-edges edges could be used to reduce this edge scattering phenomenon.

At a flap deflection angle of 29 degrees, the split flap produced less noise than the baseline configuration tested in Chapter 4. This was caused by the constriction between the deflected flap and retracted trailing-edge of the main element. This prevented the formation of a strong vortex near the leading-edge of the deflected flap. As the flap deflection angle increased to 39 degrees, a gap existed between the main element trailing-edge and the deflected flap. This increased the noise due to a high speed flow through the gap. By constricting the gap between the main element and the deflected flap, the formation of the side-edge vortex can be delayed resulting in a weaker vortex. The use of Continuous Moldline Technology (CMT) has been applied to this area. A similar effect could be achieved by applying brushes or a deformable porous material to constrict this gap between the deflected flap and the retracted trailing-edge of the main element.

As well as displacing the vortex, the application of a porous side-edge resulted in the formation of a weaker vortex and shear layer. One way to reduce the strength of the flap side-edge vortex is to control the spanwise distribution of circulation. Ideally this would require less loading on the flaps to produce a more idealised distribution across the wing. Abrupt changes in the spanwise derivative of circulation ($\partial\Gamma/\partial z$) should be avoided. The use of active flow control and circulation control could be used to minimise

the loading on the flaps, thereby reducing the strength of the side-edge vortex.

The advantage of a porous side-edge is that it is a passive means of flow control and doesn't require any energy from the aircraft systems. Also its impact on aerodynamic performance is minimal. The porous material eliminates the sharp edges at the flap side-edge, thereby reducing the edge scattering effect. Further work could be done on investigating the effect of varying the width of the porous material along its chord. The potential advantages of using a tapered porous side-edge was discussed in Section 5.3. The porous side-edge could the tapered so that its width increased towards the trailing edge. For a tapered porous side-edge, the spanwise extent of the treatment is small near the leading-edge. This reduces the loss in aerodynamic loading. As shown in the detached eddy simulation in Chapter 8, the amplitude of the unsteady fluctuations increased as the vortex grew in size. To displace the post merged, off-surface vortex further away from the surface, a wider porous side-edge is needed. This is to ensure a sufficient mass flux through the material to displace the large, unsteady vortical structure away from the surface.

9.6 Dissemination

This work has been presented twice at the AIAA Aerospace Sciences Meeting and Exhibits in 2006 [87] and 2007 [88]. A journal paper is currently under review.

Bibliography

[1] Dobrzynski, W.M., "Trailing-Edge Airframe Noise Source Studies on Aircraft Wings," *Journal of Aircraft*, Vol. 18, No. 5, 1981, pp. 397–402.

[2] Crighton, D.G., "Airframe Noise," Aeroacoustic of Flight Vehicles: Theory and Practice, edited by H.H. Hubbard, Vol. 1 NASA RP 1258, 1991.

[3] Chow, L.C., Mau, K. and Remy, H., "Landing Gear and High Lift Devices Airframes Noise Research," AIAA Paper 2002-2408, 2002.

[4] Fink, M.R., Schlinker, M.H., "Airframe Noise Component Interaction Studies," *Journal of Aircraft*, Vol. 17, No. 2, 1980, pp. 99–105.

[5] Ahyte, W.F., Miller, W.R. and Meecham, W.C., "Wing and Flap Noise Measured by Near- and Far-Field Cross-Correlation Techniques," AIAA Paper 79-0667, 1979.

[6] Kendall, J.M. and Ahyte, W.F., "Noise Generation by a Lifting Wing/Flap Combination at Reynolds Numbers to 2.8×10^6," AIAA Paper 80-0035, 1980.

[7] "New Perspectives in Aeronautics: CARINA (Computational Aeroacoustics Research Initiative on Airframe Noise)," Tech. rep.

[8] Molin, N., Roger, M. and Barre, S., "Prediction of Aircraft High-Lift Device Noise Using Dedicated Analytical Models," AIAA Paper 2003-3223, 2003.

[9] Smith, M.G. and Chow, L.C., "Aerodynamic Noise Sources on High Lift Slats and Flaps," AIAA Paper 2003-3226, 2003.

[10] Fink, M.R., "Noise Component Method for Airframe Noise," *AIAA Journal*, Vol. 16, No. 10, 1979, pp. 659–665.

[11] Fethney, P., "An Experimental Study of Airframe Self-Noise," *Progress in Astronautics and Aeronautics: Aeroacoustics: STOL Noise; Airframe and Airfoil Noise, AIAA*, Vol. 45, pp. 379–404.

[12] Davy, R. and Moens, F., "Aeroacoustic Behaviour of a 1/11 Scale Airbus Model in the Open Anechoic Wind Tunnel CEPRA 19," AIAA Paper 2002-2412, 2002.

[13] Tam, C.K.W., "Computational Aeroacoustics: Issues and Methods," *AIAA Journal*, Vol. 33, No. 10, 1995, pp. 1788–1796.

[14] Roe, P.L., "Technical Prospects for Computational Aeroacoustics," AIAA Paper 92-02-032, 1992.

[15] Morfey, C.L., "Fundamental Problems in Aeroacoustics," *Seventh International Congress on Sound and Vibration, Germany*, 2000.

[16] Lighthill, M.J., "On Sound Generated Aerodynamically; I. General Theory," *Proceedings of the Royal Society of London, Series A*, Vol. 211, pp. 54–587.

[17] Howe, M.S., *Theory of Vortex Sound*, Cambridge University Press, 1st ed., 2002.

[18] Curle, N., "The Influence of Solid Boundaries Upon Aerodynamic Sound," *Proceedings of the Royal Society, Series A*, Vol. 231, 1955, pp. 505.

[19] Ffowcs-Williams, J.E. and Hall, L.H., "Aerodynamic Sound Generation by Turbulent Flow in the Vicinity of a Scatting Half-Plane," *Journal of Fluid Mechanics*, Vol. 40, 1970, pp. 657–670.

[20] Ffowcs-Williams, J.E. and Hawkins, D.L., "Sound Generation by Turbulence and Surfaces in Arbitrary Motion," *Philosophical Transactions of the Royal Society of London A*, Vol. 342, 1969, pp. 264–321.

[21] Lockard, D.P., "A Comparison of Ffowcs Williams-Hawkings Solvers for Airframe Noise Applications," AIAA Paper 2002-2580, 2002.

[22] Farassat, F. and Brentner, K.S., "The Prediction of Helicopter Rotor Discrete Frequency Noise," *Vertica*, Vol. 7, No. 4, 1983, pp. 309–320.

[23] Spaid, F.W. and Lynch, F.T., "High Reynolds Number, Multi-Element Airfoil Flowfield Measurements," AIAA Paper 96-0682, 1996.

[24] Valarezo, W.O., Dominik, C.J., McGhee, R.J., Goodman, W.L. and Paschal, K.B., "Multielement Airfoil Optimization for Maximum Lift at High Reynolds Number," AIAA Paper 91-13332, September 1991.

[25] Lynch, F.T., "Experimental Necessities for Subsonic Transport Configuration Development," AIAA Paper 92-0158, January 1992.

[26] Gursul, I., "Review of Unsteady Vortex Flows over Delta Wings," AIAA Paper 2003-3942, 2003.

[27] Baker, G.R., Barker, S.J., Bofah, K.K. and Saffman, P.G., "Laser Anemometer Measurements of Trailing Vortices in Water," *Journal of Fluid Mechanics*, Vol. 65, No. 2, 1974, pp. 325–336.

[28] Menke, M. and Gursul, I., "Unsteady Nature of Leading Edge Vortices," *Physics of Fluids*, Vol. 9, No. 10, 1997, pp. 1–7.

[29] Gursul, I. and Wensheng, X., "Origin of Vortex Wandering over Delta Wings," *Journal of Aircraft*, Vol. 37, No. 2, 2000, pp. 348–350.

[30] Meredith, P.T., "Viscous Phenomena Affecting High-Lift Systems and Suggestions for Future CFD Development," High Lift System Aerodynamics AGARD-CP-15, Paper 19, 1993.

[31] Lynch, F.T., Potter, R.C. and Spaid, F.W., "Requirements for Effective High-Lift CFD," International Council of the Aeronautical Sciences Proceedings, 20th Congress, AIAA Vol. 2, September 1996.

[32] Khorrami, M.R., Singer, B.A. and Radeztsky Jr., R.H., "Reynolds-Averaged Navier-Stokes Computations of a Flap-Side-Edge Flowfield," *AIAA Journal*, Vol. 37, No. 1, 1999, pp. 14–22.

[33] Spalart, P.R. and Allmaras, S.R., "A One-Equation Turbulence Model for Aerodynamic Flows," AIAA Paper 92-0439, 1992.

[34] Khorrami, M.R., Berkman, M.E., Li, F. and Singer, B.A., "Computational Simulations of a Three-Dimensional High-Lift Wing," AIAA Paper 2002-2804, 2002.

[35] Streett, C.L., "Numerical Simulation of a Flap-Edge Flowfield," AIAA Paper 98-2226, 1998.

[36] Cummings, R.M., Morton, S.A. and Forsythe, J.R., "Detached-Eddy Simulation of Slat and Flap Aerodynamics for a High-Lift Wing," AIAA Paper 2004-1233, 2004.

[37] Moitra, A., "Automated CFD Analysis of Two-Dimensional High-Lift Flows," *AIAA Journal*, Vol. 39, No. 4, 2002, pp. 662–667.

[38] Moitra, A., "Unstructured Grid Issues in 2-D High-Lift Computations," *Proceedings of the 7th International Conference on Grid Generation in Computational Field Simulations. International Society of Grid Generation*, September 2000, pp. 263–274.

[39] Fluent Inc., *FLUENT 6.0 User's Guide*, 2001.

[40] Spalart, P.R., "Trends in Turbulence Treatments," AIAA Paper 2000-2306.

[41] Walsh, P.C. and Zingg, D.W., "Solution Adaptation of Unstructured Grids for Two-Dimensional Aerodynamic Computations," *AIAA Journal*, Vol. 39, No. 5, 2001, pp. 831–837.

[42] Spalart, P.R., "Young-Person's Guide to Detached-Eddy Simulation Grids," NASA CR-2001-211032, 2001.

[43] Godin, P. and Zingg, D.W., "High-Lift Aerodynamic Computations with One- and Two-Equation Turbulence Models," AIAA Paper 96-0562, 1996.

[44] Mentor, F.R., "Improved Two-Equation $k-\omega$ Models for Aerodynamic Flows," NASA TM 103975, October 1992.

[45] Mentor, F.R., "Zonal Two-Equation $k-\omega$ Models for Aerodynamic Flows," AIAA Paper 93-2906, July 1993.

[46] Mentor, F.R., "Two-Equation Eddy-Viscosity Turbulence Models for Engineering Applications," *AIAA Journal*, Vol. 32, No. 8, 1994, pp. 1598–1605.

[47] Macaraeg, M.G., "Fundamental Investigations of Airframe Noise," AIAA Paper 98-2224, 1998.

[48] Brooks, T.F. and Humphreys Jr., W.M., "Flap-edge Aeroacoustic Measurements and Predictions," *Journal of Sound and Vibration*, Vol. 261, No. 1, 2003, pp. 31–74.

[49] Brooks, T.F. and Hodgson, T.H., "Trailing-edge Noise Prediction from Measured Surface Pressures," *Journal of Sound and Vibration*, Vol. 78, No. 1, 1981, pp. 69–117.

[50] Meadows, K.R., Brooks, T.F., Humphreys, W.M., Hunter, W.W. and Gerhold, C.H., "Aeroacoustic Measurements of a Wing-Flap Configuration," AIAA Paper 97-1595, 1997.

[51] Choudhari, M., Lockard, D.P., Macaraeg, M.G., Singer, B.A., Streett, C.L., Neubert, G.R., Stoker, R.W., Underbrink, J.R., Berkman, M.E., Khorrami, M.R., Sadowski, S.S., "Aeroacoustic Experiments in the Langley Low-Turbulence Pressure Tunnel," NASA TM-2002-211432, 2002.

[52] Smith, S.T., "Flap Side-Edge Vortex Bursting and Airframe Noise," AIAA Paper 2000-1999, 2002.

[53] Benjamin, T.B., "Theory of the Vortex Breakdown Phenomenon," *Journal of Fluid Mechanics*, Vol. 14, No. 4, 1963, pp. 593–629.

[54] Harvey, J.K., "Some Observation of the Vortex Breakdown Phenomenon," *Journal of Fluid Mechanics*, Vol. 14, No. 4, 1963, pp. 585–592.

[55] Bossel, H.H., "Vortex Breakdown Flowfield," *Physics of Fluids*, Vol. 12, No. 3, 1969, pp. 498–508.

[56] Grabowski, W.J. and Berger, S.A., "Solutions of the Navier-Stokes Equations for Vortex Breakdown," *Journal of Fluid Mechanics*, Vol. 75, No. 3, 1976, pp. 525–544.

[57] Salas, M.D. and Kuruvila, G., "Vortex Breakdown Simulation: A Circumspect Study of the Steady Laminar Axisymmetric Model," *Computers and Fluids*, Vol. 17, No. 1, 1989, pp. 247–262.

[58] Gursul, I., "Review of Unsteady Vortex Flows Over Delta Wings," AIAA Paper 2003-3942, 2003.

[59] Choudhari, M. and Khorrami, M.R., "Computational Study of Porous Treatment for Altering Flap Side-Edge Flow Field," AIAA Paper 2003-3113, 2003.

[60] Lilley, G.M., "A Study of the Flight of the Owl," AIAA Paper 98-2340, 1998.

[61] Hardin, J.C., "Noise Radiation from the Side-Edge of Flaps," *AIAA Journal*, Vol. 18, No. 5, 1980, pp. 549–552.

[62] Sen, R., "Vortex-Oscillation Model of Airfoil Side-Edge Noise," *AIAA Journal*, Vol. 35, No. 3, 1997, pp. 441–449.

[63] Khorrami, M.R. and Singer, B.A., "Stability Analysis for Noise-Source Modeling of a Part-Span Flap," *AIAA Journal*, Vol. 37, No. 10, 1999, pp. 1206–1212.

[64] Howe, M.S., "On the Generation of Side Edge Flap Noise," *Journal of Sound and Vibration*, Vol. 80, No. 4, 1982, pp. 555–573.

[65] Storms, B.L., Hayes, J.A., Jaeger, S.M. and Soderman, P., "Aeroacoustic Study of Flap-Tip Noise Reduction Using Continuous Moldline Technology," AIAA Paper 2000-1976, 2000.

[66] Koop, L., Ehrenfried, K., Dillmann, A. and Michel, U., "Reduction of Flap Side Edge Noise by Active Flow Control," AIAA Paper 2002-2469, 2002.

[67] Horne, C.F., Hayes, J. and Ross, J.C., "Measurements of Unsteady Pressure Fluctuations on the Surface of an Unswept Multi-Element Airfoil," AIAA Paper 97-1645, 1997.

[68] Blackner, A.M. and Davis, C.M., "Airframe Noise Source Identification using Elliptical Mirror Measurement Techniques," Tech. rep.

[69] Storms, B.L., Takahashi, T.T., Horne, W.C., Ross, J.C., Dougherty, R.P. and Underbrink, J.R., "Flap Tip Treatments for the Reduction of Lift-Generated Noise," NASA CDTM- 21006, March 1996.

[70] Ross, J.C., Storms, B.L. and Kumagai, H., "Aircraft Flyover Noise Reduction Using Lower Surface Flap-Tip Fences," NASA CDTM- 21004, September 1995.

[71] Guo, Y.P. and Joshi, M.C., "Noise Characteristics of Aircraft High Lift Systems," *AIAA Journal*, Vol. 41, No. 7, 2003, pp. 1247–1256.

[72] Miller, W.R., *Flap Noise Characteristics Measured by Pressure Cross-Correlation Techniques*, Ph.D. thesis, University of California, 1980.

[73] Baldwin, G., "11 × 8 wind tunnel boundary layer test results 14th March 1999," *Internal Report, Southampton University Wind Tunnels*.

[74] King, L., "On the convection of heat from small cylinders in a stream of fluid: determination of the convection constants of small platinum wires with applications to hot-wire anemometry," *Philosophical Transactions of the Royal Society of London, Series A*, Vol. 214, 1914, pp. 373–432.

[75] Dantec Dynamics, *Probes for hot-wire anemometry*, 2005.

[76] Freymuth, P., "Frequency response and electronic testing for constant-temperature hot-wire anemometers," *J. Phys. E: Sci. Instrum*, Vol. 10, 1977, pp. 705–710.

[77] Bruun, H., *Hot-wire anemometry*, Oxford University Press, 1st ed., 1995.

[78] ESDU 80024, *Blockage Corrections for bluff bodies in confined flows*, 1998.

[79] ERG Materials and Aerospace Corp., *Duocel Aluminum Foam*, 2006.

[80] Khorrami, M.R. and Choudhari, M., "Application of Passive Porous Treatment to Slat Trailing Edge Noise," NASA TM-2003-212416, 2003.

[81] Wilcox, D.C., *Turbulence Modeling for CFD*, Griffin Printing, CA., 1st ed., 1994.

[82] Shur, M., Spalart, P.R., Strelets, M. and Travin, A., "Detached-Eddy Simulation of an Airfoil at High Angle of Attack," 4th Int. Symposium on Eng. Turb. Modeling and Experiments, Corsica, France, 1999.

[83] Dacles-Mariani, J., Zilliac, G.G., Chow, J.S., and Bradshaw, P., "Numerical/Experimental Study of a Wingtip Vortex in the Near Field," *AIAA Journal*, Vol. 33, No. 9, 1995, pp. 1561–1568.

[84] Ashcroft, G.B., *A Computational and Experimental Investigation into the Aeroacoustics of Low Speed Flows*, Ph.D. thesis, University of Southampton, 2004.

[85] Farassat, F., "Derivation of Formulations 1 and 1A of Farassat," NASA TM-2007-214853, 2007.

[86] Crighton, D.G., "Radiation from vortex filament motion near a half-plane," *Journal of Fluid Mechanics*, Vol. 51, 1972, pp. 357–362.

[87] Angland, D., Zhang, X., Chow, L.C. and Molin, N., "Measurements of Flow around a Flap Side-Edge with Porous Edge Treatment," AIAA Paper 2006-0213, 2006.

[88] Angland, D., Zhang, X., Molin, N. and Chow, L.C., "Measurements of Flow around a Split Flap Configuration," AIAA Paper 2007-0225, 2007.

Appendix A

Pressure Tap Locations

A.1 Main Element

No.	x (m)	Δx (mm)
1	0	-
2	4	4
3	8	4
4	12	4
5	16	4
6	20	4
7	28	8
8	36	8
9	44	8
10	52	8
11	60	8
12	68	8
13	76	8
14	92	16
15	132	40
16	172	40
17	222	50
18	332	110
19	412	80
20	492	80
21	556	64
22	596	40
23	661	65

TABLE A.1: Location of pressure taps on suction surface of main element.

No.	x (m)	Δx (mm)
24	4	-
25	8	4
26	12	4
27	16	4
28	20	4
29	28	8
30	36	8
31	44	8
32	60	16
33	120	60
34	200	80
35	310	110
36	360	50
37	440	80
38	520	80
39	575	55
40	578	3
41	593	15
42	613	20
43	633	20
44	653	20
45	671	18

TABLE A.2: Location of pressure taps on pressure surface of main element.

Mic No.	x (m)	y (m)
1	0.002	0.008
2	0.010	0.020
3	0.586	0.038
4	0.622	0.042
5	0.024	0.033

TABLE A.3: Location of on-surface microphones on pressure surface of main element.

A.2 Flap

No.	x (m)	Δx (mm)
1	0	-
2	0.002	2
3	0.005	3
4	0.008	3
5	0.014	6
6	0.022	8
7	0.035	13
8	0.06	25
9	0.08	20
10	0.09	10
11	0.1	10
12	0.125	25
13	0.16	35

TABLE A.4: Location of chordwise pressure taps on suction surface of half-span flap.

No.	x (m)	Δx (mm)
14	0.002	-
15	0.0035	1.5
16	0.005	1.5
17	0.01	5
18	0.075	65
19	0.125	50
20	0.16	35

TABLE A.5: Location of chordwise pressure taps on pressure surface of half-span flap.

No.	z (m)	Δz (mm)
1	0	-
2	0.04	40
3	0.08	40
4	0.16	80
5	0.24	80
6	0.28	40
7	0.32	40
8	0.36	40
9	0.4	40
10	0.44	40
11	0.45	10
12	0.46	10
13	0.47	10
14	0.48	10
15	0.49	10
16	0.495	5

TABLE A.6: Location of spanwise pressure taps on half-span flap.

Appendix B

Error, Uncertainty, Repeatability and Blockage Corrections

B.1 Force Measurements

Tare corrections were taken. They had three different sources: the endplates, the tailbar and the struts. By measuring the forces of all three together and removing one component at a time it was possible to calculate the contribution of each component to the tare correction. This ignores all interference effects between each component to the other components and also to the model which is not correct. It is however sufficient for the current analysis. The tare values are tabulated in the following Tables for C_L, C_D and C_M. The tailbar and strut are angle of attack are independent while the endplate tare values are dependent on angle of attack. The tare values are presented for three airspeeds and four different angles of attack in Tables B.1 - B.3. The values presented are the sum of the contributions from the tailbar, endplates and struts presented in coefficient form.

Angle of Attack	C_L	C_D	C_M
0 degrees	0.007	0.253	0.159
5 degrees	0.007	0.249	0.090
10 degrees	0.005	0.247	0.005
15 degrees	0.006	0.246	0.050

TABLE B.1: Tare correction $V_\infty = 10$ m/s.

The wind tunnel correction was performed using the method of [78]. The forces were non-dimensionalised as follows using the incompressible three-dimensional definitions for the aerodynamic coefficients.

$$C_L = \frac{L}{\frac{1}{2}\rho_\infty V_\infty^2 S} \tag{B.1}$$

Angle of Attack	C_L	C_D	C_M
0 degrees	0.030	0.245	0.168
5 degrees	0.051	0.241	0.163
10 degrees	0.019	0.240	0.106
15 degrees	0.018	0.238	0.080

TABLE B.2: Tare correction $V_\infty = 20$ m/s.

Angle of Attack	C_L	C_D	C_M
0 degrees	0.041	0.237	0.171
5 degrees	0.042	0.228	0.162
10 degrees	0.012	0.226	0.137
15 degrees	0.013	0.223	0.126

TABLE B.3: Tare correction $V_\infty = 30$ m/s.

$$C_D = \frac{D}{\frac{1}{2}\rho_\infty V_\infty^2 S} \tag{B.2}$$

$$C_M = \frac{M}{\frac{1}{2}\rho_\infty V_\infty^2 S\, c} \tag{B.3}$$

The lift, drag and pitching moment result are shown in Figures 4.1 - 4.3 adjusted for wind tunnel blockage correction factors. The forces were measured at airspeeds varying from 10 to 30 m/s. The angle of attack was varied from -5 degrees to 22.5 degrees. This data was averaged over three runs. The angle of attack of the main element was set to ± 0.05 degrees. The freestream values of temperature, static pressure and velocity were averaged from the values at the beginning and the end of each run. The average variations between the start and the end of the run were ±0.5 °C for temperature, ±0.1 mmH_2O for pressure and ±0.01 m/s for velocity. The short term repeatability for C_L and C_D was within 1.6% and for C_M the repeatability was within 2.1%.

The presence of the wind tunnel walls, which are impermeable, constrain the flow around the model. This leads to a difference between the measured values in the wind tunnel and the free-air values. Therefore corrections need to be made to the measured force data to obtain the free-air values. The correction comprises of two parts. The first is a blockage effect which results in increased velocities in the flow around the body and the wake. The second is the lift interference correction. For three-dimensional bodies the induced drag needs to be deducted from the measured drag since it does contribute to the blockage effect. The method used for the blockage correction factors was the quasi-streamline method [78]. This is applicable where the separation occurs behind the maximum cross-sectional area of the body. For three-dimensional flow the correction is

as follows.

$$\frac{C_{Ff}}{C_F} = 1 - \lambda_1\lambda_3\left(1 + \frac{1}{\lambda_2}\frac{b}{c}\right)\frac{cS}{A^{1.5}} - 0.5(C_D - C_{Di})\frac{S}{A} \tag{B.4}$$

λ_1 is a factor including allowance for wind-tunnel shape. For a rectangular cross section wind tunnel with fillets the value is given below. λ_2 is a two-dimensional body shape factor. and λ_3 is a two-dimensional body shape factor. They are defined as follows.

$$\lambda_1 = 0.72\left[\frac{b_d}{H_d} + \frac{H_d}{b_d}\right] \tag{B.5}$$

$$\lambda_2 = \left(\frac{4}{\pi}\right)\left(\frac{\text{Maximum body cross sectional area}}{bc}\right) \tag{B.6}$$

$$\lambda_3 = \left(\frac{\text{Body Volume}}{cS}\right) \tag{B.7}$$

The above equations are applicable for a body mounted in the tunnel centre. For the worse case scenario the wing was at 22.5 degrees angle of attack. This corresponded to a blockage area ratio of 0.044. Calculating these corresponding for C_{Ff}/C_F gives a blockage correction factor of 3.14%. The blockage corrections are tabulated in Table B.4.

Angle of Attack	C_{Ff}/C_F
-5	-0.32 %
-2.5	-0.53 %
0	-0.76 %
2.5	-1.00 %
5	-1.26 %
7.5	-1.52 %
10	-1.79 %
12.5	-2.05 %
15	-2.33 %
17.5	-2.60 %
20	-2.88 %
22.5	-3.14 %

TABLE B.4: Wind tunnel blockage corrections.

B.2 Pressure Measurements

Pressure taps were located on the chord on the main element, the chord of the half-span flap and also along the span of the suction surface of the half-span flap. The time averaged pressure at each port was averaged over 30 seconds. The short term repeatability of the on-surface pressures was within 1 %. The pressures needed to be corrected for blockage effect as well. Using the principal of invariance under constraint

the variation with blockage of the pressure difference between any two points is a function of the blockage ratio only and is independent of the location of the points [78]. The following relationship is used where C_{Ff}/C_F are given in Table B.4.

$$\frac{1 - C_{pf}}{1 - C_p} = C_{Ff}/C_F \tag{B.8}$$

B.3 Perspective Error in Particle Image Velocimetry Measurements

The instantaneous velocity vector is comprised of three components. Two components, v and w, are measured in PIV. The laser sheet is of a finite thickness and therefore the third component, u, is out-of-plane and introduces errors due to the motion of particles through the laser sheet. This error can be significant when the velocity component out-of-plane is large.

The perspective error (γ), which is defined as the difference between the true and measured in-plane displacement is given in Equation B.9.

$$\gamma = (\gamma_y, \gamma_z) = \left(\frac{\Delta x}{\Delta y} \tan \xi_y \, , \, \frac{\Delta x}{\Delta z} \tan \xi_z \right) , \tag{B.9}$$

where Δx is the thickness of the laser sheet and Δy and Δz are the measured particle displacements in the y and z directions respectively. At 30 m/s, the largest perspective error was less than 5 %.

Appendix C

Constants in S-A Model

This appendix contains the functions and constants in the Spalart-Allmaras (SA) RANS turbulence model that was discussed in Chapter 7.

The following functions are used to relate the modified turbulent viscosity ($\widetilde{\nu}$) to the eddy viscosity (ν_t), where ν is the kinematic molecular viscosity.

$$f_{v1} = \frac{\chi^3}{\chi^3 + c_{v1}^3}, \qquad \chi \equiv \frac{\tilde{\nu}}{\nu} \, . \tag{C.1}$$

The original production term [33] is defined as follows, where S is the magnitude of the vorticity.

$$\tilde{S} \equiv f_{v3} S + \frac{\tilde{\nu}}{\kappa^2 d^2} f_{v2}, \qquad f_{v2} = \left(1 + \frac{\chi}{c_{v2}}\right)^{-3}, \qquad f_{v3} = \frac{(1 + \chi f_{v1})(1 - f_{v2})}{\chi} \, , \tag{C.2}$$

where,

$$S \equiv \sqrt{2\Omega_{ij}\Omega_{ij}}, \qquad \Omega_{ij} = \frac{1}{2}\left(\frac{\partial u_i}{\partial x_j} - \frac{\partial u_j}{\partial x_i}\right) . \tag{C.3}$$

The definition of S was modified as discussed in Section 7.3 to the value given in Equation 7.9. This was to reduce the eddy viscosity in the laminar-like vortex core.

The wall destruction function f_w is defined as follows.

$$f_w = g\left[\frac{1 + c_{w3}^6}{g^6 + c_{w3}^6}\right]^{\frac{1}{6}}, \qquad g = r + c_{w2}(r^6 - r), \qquad r \equiv \frac{\tilde{\nu}}{\tilde{S}\kappa^2 d^2} \, . \tag{C.4}$$

The function f_{t2} is defined as follows. The trip function f_{t1} was not used in this study.

$$f_{t2} = c_{t3} \exp(-c_{t4}\chi^2) \, . \tag{C.5}$$

The constants are shown in Table C.1.

$c_{b1} = 0.1355$	$c_{b2} = 0.622$	$c_{v1} = 7.1$
$\kappa = 0.41$	$c_{v2} = 5$	$\sigma = 2/3$
$c_{w1} = c_{b1}/\kappa^2 + (1 + c_{b2})/\sigma$	$c_{w2} = 0.3$	$c_{w3} = 2$
$c_{t1} = 1$	$c_{t2} = 2$	$c_{t3} = 1.2$
$c_{t4} = 0.5$		

TABLE C.1: Spalart-Allmaras model coefficients.